

DEVELOPMENT OF HIGH PERFORMANCE GRINDING PROCESS
USING HYBRID REDUNDANT MANIPULATOR

A THESIS SUBMITTED TO
THE GRADUATE SCHOOL OF NATURAL AND APPLIED SCIENCES
OF
MIDDLE EAST TECHNICAL UNIVERSITY

BY

MASOUD LATIFI NAVID

IN PARTIAL FULFILLMENT OF THE REQUIREMENTS
FOR
THE DEGREE OF DOCTOR OF PHILOSOPHY
IN
MECHANICAL ENGINEERING

DECEMBER 2017

Approval of the thesis:

**DEVELOPMENT OF HIGH PERFORMANCE GRINDING
PROCESS USING HYBRID REDUNDANT MANIPULATOR**

submitted by **MASOUD LATIFI NAVID** in partial fulfillment of the requirements for the degree of **Doctor of Philosophy in Mechanical Engineering Department, Middle East Technical University** by,

Prof. Dr. Gülbin Dural Ünver
Dean, Graduate School of **Natural and Applied Sciences**

Prof. Dr. M. A. Sahir Arıkan
Head of Department, **Mechanical Engineering**

Assoc. Prof. Dr. Erhan İlhan Konukseven
Supervisor, **Mechanical Engineering Dept., METU**

Examining Committee Members:

Prof. Dr. Raif Tuna Balkan
Mechanical Engineering Dept., METU

Assoc. Prof. Dr. Erhan İlhan Konukseven
Mechanical Engineering Dept., METU

Assoc. Prof. Dr. Mustafa Doğan
Control and Automation Engineering Dept.,
Istanbul Technical University

Assoc. Prof. Dr. Murat Demiral
Mechanical Engineering Dept., Çankaya University

Assist. Prof. Dr. Orkun Özşahin
Mechanical Engineering Dept., METU

Date: 2017/12/28

I hereby declare that all information in this document has been obtained and presented in accordance with academic rules and ethical conduct. I also declare that, as required by these rules and conduct, I have fully cited and referenced all material and results that are not original to this work.

Name, Last Name: MASOUD LATIFI NAVID

Signature :

ABSTRACT

DEVELOPMENT OF HIGH PERFORMANCE GRINDING PROCESS USING HYBRID REDUNDANT MANIPULATOR

LATIFI NAVID, MASOUD

Ph.D., Department of Mechanical Engineering

Supervisor : Assoc. Prof. Dr. Erhan İlhan Konukseven

December 2017, 141 pages

Automatic grinding using robot manipulators, requires simultaneous control of the robot endpoint and force interaction between the robot and the constraint surface. In robotic grinding, surface quality can be increased by accurate estimation of grinding forces where significant tool and workpiece deflection occurs. Tool deflection during robotic grinding operation causes geometrical errors in the workpiece cross-section. Also, it makes controlling the grinding cutting depth difficult. Moreover small diameter of the tool in robotic grinding causes different behavior in the grinding process in comparison with the tools that are used by universal grinding machines. In this study, a robotic surface grinding force model is developed in order to predict the normal and tangential grinding forces. A physical model is used based on chip formation energy and sliding energy. To improve the model for robotic grinding operations, a refining term is added. In order to include the stiffness of the tool and setup in the force model,

penetration tests are implemented and their results are used in refining term of the force model. The model coefficients are estimated using a linear regression technique. The proposed model is validated by comparing model outputs with experimentally obtained data. Evaluation of the test results demonstrates the effectiveness of the proposed model in predicting surface grinding forces. In this thesis, a method is proposed for calculation of the tool deflection in normal and tangential directions based on grinding force feedback in these directions. Based on calculated values, a real-time tool deflection compensation algorithm is developed and implemented. Implementing surface grinding with constant normal force is a well-known approach for improving surface quality. Tool deflection in the robotic grinding causes orientation between the force sensor reference frame and tool reference frame. This means that the measured normal and tangential forces by the sensor are not actual normal and tangential interaction forces between the tool and workpiece. In order to eliminate this problem, a resultant grinding force control strategy is designed and implemented for a parallel hexapod-robotic light abrasive surface grinding operation. Due to the nonlinear nature of the grinding operation, a supervised fuzzy controller is designed where the reference input is identified by the proposed grinding force model. Evaluation of the experimental results demonstrates significant improvement in grinding operation accuracy using the proposed resultant force control strategy in parallel with a real-time tool deflection compensation algorithm. The final aim of this thesis is to develop a posture optimization strategy for robotic grinding operation using 12 DOF hybrid redundant manipulator. The 12 DOF redundant hybrid manipulator of present study is composed of a 6 DOF serial ABB IRB2000 robot and a 6 DOF PI H-824 hexapod where the parallel hexapod is connected to the end of the serial ABB manipulator. Here the fifth joint (wrist) of the ABB serial manipulator is the weakest joint in the robot, so the computed torque of this joint is selected as the cost function. The aim is to minimize this factor by finding the best configuration of the hybrid manipulator using genetic algorithm approach. For such a purpose, a complete kinematic and dynamic model of the 12 DOF manipulator is developed where the output of the

grinding force model is fed into the dynamic model as external reaction forces. The computed torque of the wrist joint is given to the optimization module and new configuration is generated by the module and is given to the dynamic model. This process continues until converge to the minimum computed torque value. Then the optimal configuration is chosen for the grinding operation. The evaluation of this posture optimization approach shows its great ability to decrease the necessary actuating torques of the redundant manipulator joints.

Keywords: Robotic Grinding, Grinding Force model, Hybrid Redundant Manipulator, Tool Deflection Compensation, Posture Optimization

ÖZ

HİBRİT ARTIK ROBOT KOLU KULLANARAK YÜKSEK PERFORMANSLI TAŞLAMA İŞLEMİ GELİŞTİRMESİ

LATIFI NAVID, MASOUD

Doktora, Makina Mühendisliği Bölümü

Tez Yöneticisi : Doç. Dr. Erhan İlhan Konukseven

Aralık 2017, 141 sayfa

Robot manipülatörler kullanılarak yapılan otomatik taşlama işlemi, robot uç noktasının ve robot ile yüzey arasında oluşan kuvvetin kontrolünü gerektirir. Robotik taşlama işleminde takım ve iş parçası eğilmeleri önemli ölçüde olduğundan, oluşan kuvvetlerin doğru tahmin edilmesi, ortaya çıkan yüzey kalitesini artırmakta önem taşımaktadır. Robotik taşlama işleminde takımda oluşan sapmalar iş parçasının kesitinde geometrik hatalara neden olmaktadır. Ayrıca bu durum taşlama derinliğinin kontrolünü de zorlaştırmaktadır. Ek olarak, robotik taşlama işleminde kullanılan küçük boyutlu takımlar üniversal taşlama makinelerinde kullanılan takımlara kıyasla taşlama işlemin süresince farklı davranışlara sebebiyet verir. Bu çalışmada; robotik yüzey taşlama kuvvet modeli, teğet ve dik yöndeki kuvvetlerin tahmin edilebilmesi için geliştirilmiştir. Talaş oluşturma ve kayma enerjisine dayanan fiziksel bir model kullanılmıştır. Bu modeli robotik taşlama işleminde kullanabilmek için modele iyileştirici bir terim eklenmiştir.

İyileştirici terimin bulunmasında penetrasyon test sonuçları kullanılarak, takımın ve deney düzeneğinin rijitliği modele dâhil edilmiştir. Modelin katsayıları doğrusal regresyon metodu ile bulunmuştur. Sunulan modelin çıktıları ile deneysel olarak elde edilen sonuçlar karşılaştırılarak doğruluğu gösterilmiştir. Test sonuçlarının karşılaştırılması sunulan modelin yüzey taşlama işlemi kuvvetlerinin tahminindeki başarımını göstermektedir. Bu tezde, dik ve teğet yönde takımın oluşan sapmaların hesaplanması için bir model öne sürülmüştür. Bu model aynı yönlerdeki taşlama işlemi kuvvetleri geri bildirimini temel almaktadır. Hesaplanan değerlere göre gerçek zamanlı takım esneme telafisi algoritması oluşturulmuş ve uygulanmıştır. Yüzey kalitesinin artırmak için dik yönde sabit kuvvet kontrollü yüzey taşlama işlemi uygulaması bilinen bir yöntemdir. Robotik taşlama işleminde oluşan takım sapması, kuvvet sensörü referans sistemi ile takım referans sistemi arasında bir oryantasyon farkı oluşturur. Bu fark, sensörden okunan takım ile iş parçası arasındaki dik ve teğet yöndeki kuvvet değerlerinin, gerçekte oluşan kuvvetler değerlerine eşit olmadığını ifade eder. Bu problemi ortadan kaldırmak için, bileşke kuvvet modeli kontrol metodu yüzey taşlama işlemi için tasarlanıp uygulanmıştır. Taşlama işleminin doğrusal olmayan yapısından dolayı, referans girdisi taşlama kuvvet modelinden tanımlanan bir denetimli bulanık kontrolcü tasarlanmıştır. Sunulan bileşke kuvveti kontrolü metodu ve gerçek zamanlı takım sapması telafisi algoritması kullanılarak yapılan deney sonuçları taşlama işleminin doğruluğunun önemli ölçüde iyileştirildiği görülmektedir. Bu tezin son amacı, 12 serbestlik dereceli hibrit manipülatör kullanılarak robotik taşlama işlemi için bir duruş eniyilemesi stratejisi geliştirmektir. Sunulan çalışmada kullanılan, 12 serbestlik dereceli manipülatör 6 serbestlik dereceli seri ABB IRB2000 robotun ucuna yine 6 serbestlik dereceli paralel PI H-824 heksapod robotun takılmasıyla oluşturulmuştur. ABB seri manipülatörün beşinci eklemi (bilek eklemi) en zayıf eklem olduğundan, eklem üzerine etkiyen tork değeri maliyet fonksiyonu olarak seçilmiştir. Buradaki hedef, genetik algoritma kullanılarak hibrit manipülatörün en iyi konfigürasyonunu bularak maliyet fonksiyonunu en küçüklemedir. Bu amaç için 12 serbestlik dereceli manipülatörün tüm kinematik ve dinamik modelleri oluşturulmuştur. Oluşturulan taşlama kuvvet

modelinin çıktısı dinamik modele harici reaksiyon kuvveti olarak beslenmiştir. Bilek eklemi üzerine etkiyen tork eniyileme modeline beslenip, manipülatörün yeni konfigürasyonu elde edilmiş ve dinamik modele verilmiştir. Bu sürece, en küçük tork değeri elde edilene kadar devam ediliyor. Daha sonra taşlama işlemi için hesaplanan optimum konfigürasyon kullanılıyor. Bu duruş eniyilemesi yaklaşımı, fazlalık manipülatör eklemlerine etkiyen gerekli torqların azaltılmasında etkisini göstermiştir.

Anahtar Kelimeler: Robotik Taşlama, Taşlama Kuvvet Modeli, Hibrit Artık Robot Kolu, Takım Eğim Kompanzasyonu, Duruş Optimizasyonu

To Prof. Dr. Cavad Heyat

ACKNOWLEDGMENTS

First of all, I am deeply grateful to my supervisor Assoc. Prof. Dr. Erhan İlhan Konukseven for his invaluable supervision, guidance and criticism and especially his extreme support not only during this study but also in whole period of my graduate study. I also thank examining committee members, Prof. Dr. Tuna Balkan , Assoc. Prof. Dr. Mustafa Doğan for their valuable comments and contributions.

I would like to express my thanks to my dear friends Payam Parvizi, Abdulhamit Dönder, Ömer Okumuş, Uğur Mengilli, Kemal Açıkgöz, Musab Çağrı Uğurlu, Matin Ghaziani and Hamed Tanabi for their friendship and technical support throughout the thesis period and for all the good times we have spent.

I would like to to thank the scientific and technological research council of Turkey (TÜBİTAK) for supporting this thesis under grant number 114E274 and BİDEB-2215 fellowship.

I would like to thank my lovely family for their support, love and encouragement through all my life.

Finally, I am deeply grateful to my dear family, especially my father Moharram Latifi Navid and my wife Nejla Allahyari, for supporting me and for showing me their love throughout my PhD education.

TABLE OF CONTENTS

ABSTRACT	v
ÖZ	viii
ACKNOWLEDGMENTS	xii
TABLE OF CONTENTS	xiii
LIST OF TABLES	xvii
LIST OF FIGURES	xviii
LIST OF ABBREVIATIONS	xxiii
CHAPTERS	
1 INTRODUCTION	1
1.1 Motivation and Objectives of the Thesis	1
1.2 Contributions of the Thesis	3
1.3 Outlines of the Thesis	5

2	HYBRID MODEL BASED ON ENERGY AND EXPERIMENTAL METHODS FOR PARALLEL HEXAPOD-ROBOTIC LIGHT ABRASIVE GRINDING OPERATIONS	9
2.1	Introduction	9
2.2	Literature Survey	10
2.2.1	Grinding force models	10
2.2.1.1	Physical grinding force models	10
2.2.1.2	Empirical grinding force models	12
2.2.2	Robotic grinding	13
2.3	Development of Robotic Surface Grinding Model	15
2.3.1	Energy-based model of surface grinding forces	18
2.3.2	Penetration tests	23
2.3.3	Feature selection	28
2.3.4	Grinding force model improvement with a refining term	30
2.4	Results and discussion	33
3	HIGH PERFORMANCE PARALLEL HEXAPOD-ROBOTIC LIGHT ABRASIVE GRINDING USING REAL-TIME TOOL DEFLECTION COMPENSATION AND CONSTANT RESULTANT FORCE CONTROL	41

3.1	Introduction	41
3.2	Literature Survey	43
3.2.1	Constant Force Control	44
3.2.2	Control approaches	46
3.3	Effect of tool deflection on robotic surface grinding forces	47
3.4	Experimental setup	48
3.5	Modeling tool deflection	49
3.6	Kinematic solution for tool deflection compensation (TDC)	51
3.7	Constant resultant force control using model supervised fuzzy controller	57
3.7.1	Grinding force model	58
3.7.2	Fuzzy controller design	59
3.8	Results and discussion	61
4	KINEMATIC/DYNAMIC ANALYSIS AND POSTURE OPTI- MIZATION OF A 12 DOF HYBRID REDUNDANT MANIPU- LATOR	69
4.1	Introduction	69
4.2	Literature survey	70
4.3	Kinematic and dynamic analysis and simulation of ABB IRB2000 manipulator	72

4.3.1	Forward kinematics of the ABB IRB2000 manipulator	72
4.3.2	Inverse kinematics of the ABB IRB2000 manipulator	75
4.3.3	Jacobian calculation of ABB IRB2000 manipulator	81
4.3.4	Dynamic analysis of ABB IRB2000 manipulator	85
4.4	Kinematics and dynamic analysis of the parallel hexapod	93
4.4.1	Dynamic analysis of a 6 DOF parallel hexapod	100
4.4.1.1	Dynamic equations for upper platform (body 1)	100
4.4.1.2	Dynamic equations for motors 1-6 (bodies 2-7)	103
4.4.1.3	Dynamic equations for shafts 1-6 (bodies 8-13)	104
4.4.2	Connecting serial and parallel manipulators . .	107
4.5	Posture optimization of 12 DOF hybrid redundant manipulator	109
4.5.1	Posture optimization along the grinding path .	113
5	CONCLUSION	121
	REFERENCES	127
	CURRICULUM VITAE.	139

LIST OF TABLES

TABLES

Table 2.1	Design of experiment Taguchi method	25
Table 2.2	Descriptions of the extracted features	27
Table 2.3	Selected subset with respect to the grinding forces using CFS	29
Table 2.4	Units of parameters	34
Table 2.5	RMSE of tangential and normal forces prediction over the total dataset using proposed model and energy-based model	36
Table 3.1	Rule bases of the fuzzy controller	61
Table 4.1	Denavit-Hartenberg parameters of ABB IRB 2000 manipulator	73
Table 4.2	Number of unknowns in direct dynamic of ABB IRB2000 ma- nipulator	89
Table 4.3	Number of unknowns in direct dynamic of hexapod	101
Table 4.4	Number of unknowns in direct dynamic of hexapod	102
Table 4.5	Motion range of the PI H-824 Hexapod	114

LIST OF FIGURES

FIGURES

Figure 1.1	Steps of posture optimization process	3
Figure 2.1	Experiment setup	16
Figure 2.2	Robotic grinding with constant SDOC and spindle speed. A: Ground surface with constant feed rate where tool deflection happens, B: Ground point where hexapod is stopped (zero feed rate) without tool deflection, C: Unmachined surface	18
Figure 2.3	Grinding model generation steps	19
Figure 2.4	Penetration tests example	24
Figure 2.5	Tangential force profile of a penetration test in the time domain	26
Figure 2.6	Spindle percent load in time domain during penetration test	31
Figure 2.7	Example of the first regime robotic grinding	34
Figure 2.8	Example of the second regime robotic grinding	36
Figure 2.9	Example of the third regime robotic grinding	37
Figure 2.10	Regime 1 example. Tangential grinding force of experimental data (blue graph), proposed model outputs (red graph) and energy- based model outputs (green graph)	37

Figure 2.11 Regime 1 example. Normal grinding force of experimental data (blue graph), proposed model outputs (red graph) and energy-based model outputs (green graph)	38
Figure 2.12 Regime 2 example. Tangential grinding force of experimental data (blue graph), proposed model outputs (red graph) and energy-based model outputs (green graph)	38
Figure 2.13 Regime 2 example. Normal grinding force of experimental data (blue graph), proposed model outputs (red graph) and energy-based model outputs (green graph)	39
Figure 2.14 Regime 3 example. Tangential grinding force of experimental data (blue graph), proposed model outputs (red graph) and energy-based model outputs (green graph)	39
Figure 2.15 Regime 3 example. Normal grinding force of experimental data (blue graph), proposed model outputs (red graph) and energy-based model outputs (green graph)	40
Figure 3.1 Orientations between the tool tip reference frame and force sensor reference frame	49
Figure 3.2 Tool modeled as a cantilever rod (left). Internal moment at x distance from the tool holder is shown (right)	50
Figure 3.3 Illustration of the setup and assigned reference frames	52
Figure 3.4 Architecture of the proposed model supervised fuzzy admittance controller	59
Figure 3.5 Membership functions of Error	60
Figure 3.6 Membership functions of (Δa_p)	60
Figure 3.7 Membership functions of $(\Delta \dot{a}_p)$	60

Figure 3.8 Grinding resultant force profile without using a force controller	62
Figure 3.9 Measurement setup	62
Figure 3.10 Surface profile of the workpiece before grinding and after grinding operation without any force control	63
Figure 3.11 Inclined cross-section because of tool deflection	64
Figure 3.12 Grinding resultant force profile using the proposed force control approach	64
Figure 3.13 Surface profile of the workpiece before and after grinding operation using the proposed force control approach	66
Figure 3.14 Effect of the TDC algorithm on the workpiece cross-section .	67
Figure 3.15 Hexapod motion in the X, Y and Z directions during the robotic grinding experiment	67
Figure 3.16 Hexapod rotation around the X,Y and Z axes during the robotic grinding experiment	68
Figure 4.1 12 DOF redundant hybrid manipulator	70
Figure 4.2 Reference frames of ABB IRB2000 Manipulator	73
Figure 4.3 Forward and inverse kinematics blocks of the ABB manipulator	79
Figure 4.4 Simulation of ABB manipulator using VRML toolbox	80
Figure 4.5 Simulation of ABB manipulator	80
Figure 4.6 Trajectory, angular velocity and angular acceleration profiles of joints 1, 2 and 3. The blue graphs are related to the θ_1 , θ_2 and θ_3 . The red graphs are related to the $\dot{\theta}_1$, $\dot{\theta}_2$ and $\dot{\theta}_3$. The green graphs are related to the $\ddot{\theta}_1$, $\ddot{\theta}_2$ and $\ddot{\theta}_3$	84

Figure 4.7 Trajectory, angular velocity and angular acceleration profiles of joints 4, 5 and 6. The blue graphs are related to the θ_4 , θ_5 and θ_6 . The red graphs are related to the $\dot{\theta}_4$, $\dot{\theta}_5$ and $\dot{\theta}_6$. The green graphs are related to the $\ddot{\theta}_4$, $\ddot{\theta}_5$ and $\ddot{\theta}_6$	84
Figure 4.8 X and v_x profiles of the tip point using Jacobian matrix and numerical differentiation	85
Figure 4.9 Y and v_y profiles of the tip point using Jacobian matrix and numerical differentiation	86
Figure 4.10 Z and v_z profiles of the tip point using Jacobian matrix and numerical differentiation	86
Figure 4.11 Schematic configuration of connections and center of gravity vectors of a body	91
Figure 4.12 MATLAB [®] Simscape model of ABB IRB2000 manipulator	94
Figure 4.13 Hexapod views and assigned reference frames	95
Figure 4.14 MATLAB [®] Simscape model of parallel hexapod robot . . .	107
Figure 4.15 Posture optimization process	109
Figure 4.16 SIMULINK model of the posture optimization process	116
Figure 4.17 Posture optimization of 12 DOF hybrid redundant manipulator with first method	117
Figure 4.18 Wrist joint computed torque minimization using first optimization approach	117
Figure 4.19 Posture optimization of 12 DOF hybrid redundant manipulator with second method	118
Figure 4.20 Wrist joint computed torque minimization using second optimization approach	118

Figure 4.21 Grinding path and calculated normal and tangential grinding forces along path	119
Figure 4.22 Flowchart of the posture optimization algorithm	119
Figure 4.23 Example of posture optimization along a path	120
Figure 4.24 Simulation of posture optimization during grinding operation on a manifold	120

LIST OF ABBREVIATIONS

TDL	Tool deflection compensation
ADOC	Actual depth of cut
SDOC	Set depth of cut
DOE	Design of experiment
CFS	Correlation based feature selection
RMSE	Root mean square error
MRR	Material removal rate
ANN	Artificial neural network
GA	Genetic algorithm
CMM	Coordinate measurement machine
CNC	Computer numerical control
Rev. joint	Revolute joint
Univ. joint	Universal joint
Cylin. joint	Cylindrical joint

CHAPTER 1

INTRODUCTION

1.1 Motivation and Objectives of the Thesis

Automatic grinding systems have been investigated for years to mimic adaptive nature of human intelligence in order to replace manual grinding, which is labor intensive and not productive. However, anthropomorphous robots are the best state of the art compromise between performance and flexibility for automated grinding tasks. They provide larger work volumes, safety and efficiency at a lower cost than computer controlled (CNC) grinding machines. Also they provide a greater reachability and working capabilities on the complex paths of the deburring tasks. Therefore, anthropomorphic robots are suitable for grinding processes.

Automatic grinding using robot manipulators requires simultaneous control of the robot endpoint and force interaction between the robot and the constraint surface. In robotic grinding, surface quality can be increased by accurate estimation of grinding forces. Also in robotic grinding operation a significant tool deflection occurs due to the lower stiffness of the manipulator and tool, compared with operation by universal grinding machines. Tool deflection during robotic grinding operation causes geometrical errors in the workpiece cross-section. Also, it makes difficult to control the grinding cutting depth. The small diameter of the tool causes different behavior in the grinding process in comparison with the tools that are used by universal grinding machines.

Serial and parallel manipulators have their own advantages and disadvantages. The large workspace and flexibility of serial manipulators are very useful but extended structures of them have a tendency to vibrate working at high speeds and to deflect dealing with high loads. Also because of the serial configuration, errors of each link are added up and the overall error reflects to the end effector. Hybrid manipulators are known by combination of the serial and parallel manipulators or combination of two serial manipulators such that moving platform of the ones is fixed base of the others like a parallel manipulator chain.

The aim of this thesis is to develop a high performance grinding process using hybrid redundant manipulator. In this process a novel optimized strategy is used for posture optimization and path generation of the redundant hybrid manipulator based on computed torques minimization of a critical joint while grinding operation. For calculating the joint torque, the dynamic model of the hybrid manipulator should be developed. That's why in this thesis a complete kinematic and dynamic analysis of the hybrid manipulator is done. The interaction force between tool and workpiece should be given as input to the dynamic model in order to find the reaction forces/torques on bodies. So it is necessary to predict the normal and tangential grinding forces using a grinding force model. Due to lower stiffness of robotic grinding and tool deflection effect, an optimized force model is needed for this purpose. One of the main goals of this thesis is to develop a new force model that is optimized for robotic grinding operation considering setup stiffness. The steps of posture optimization process and the interaction between grinding model and the dynamic model are shown in Figure 1.1. Force interaction between the tool and workpiece is significant for grinding operation. Implementing grinding with constant normal force is a well-known approach for improving surface quality. Tool deflection in the robotic grinding causes orientation between the force sensor reference frame and tool reference frame. This means that the measured normal and tangential forces by the sensor are not actual normal and tangential interaction forces between the tool and workpiece. Consequently force-position control approach does not work properly. Furthermore, geometrical errors occurs in cross-section of the

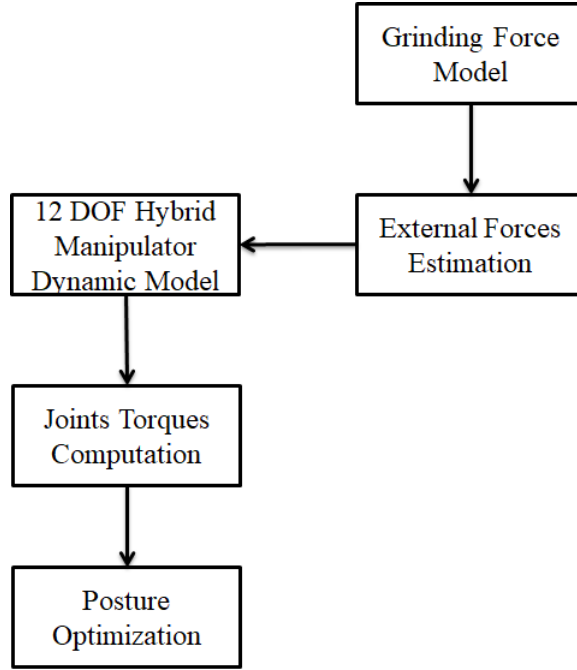


Figure 1.1: Steps of posture optimization process

workpiece because of tool deflection effect during surface grinding operations. In this thesis, one of the objectives is to compensate the tool deflection effect and prevent geometrical errors on cross-section of the workpiece by a kinematic solution.

1.2 Contributions of the Thesis

This thesis is composed of three main parts. In the first part, a novel hybrid grinding force model based on energy and experimental methods is developed. The developed model is optimized for robotic grinding operation considering the setup stiffness and mechanical properties of the setup and workpiece. A physical model is used based on chip formation energy and sliding energy. To improve the model for robotic grinding operations, a refining term is added. The stiffness of the tool and setup is inherently included using penetration test results and estimating the refining term of the model. The model coefficients are cal-

culated using a linear regression technique. The proposed model is validated by comparing model outputs with experimentally obtained data. Evaluation of the test results demonstrates the effectiveness of the proposed model in predicting surface grinding forces.

In the second part of this thesis a method is utilized for calculation of the tool deflection in normal and tangential directions based on grinding force feedback in these directions. Based on calculated values, a novel real-time tool deflection compensation (TDC) algorithm is developed and implemented for robotic grinding using a parallel hexapod. Another contribution of this part is design and implementation of a supervised resultant grinding force fuzzy controller for a parallel hexapod-robotic light abrasive surface grinding operation. Such a controller eliminates the orientation problem between sensor reference frame and tool reference frame which is a result of tool deflection phenomena in robotic grinding. Due to the nonlinear nature of the grinding operation, a supervised fuzzy controller is designed where the reference input is identified by the force model that is developed in this thesis. Evaluation of the experimental results demonstrates significant improvement in grinding operation accuracy using the proposed resultant force control strategy in parallel with a real-time TDC algorithm.

In the third part of this thesis a novel strategy for posture optimization of the 12 DOF redundant hybrid manipulator is proposed. This method is based on minimization of the computed torque of wrist joint of serial part of the hybrid manipulator. The kinematic and dynamic analysis of the hybrid manipulator is done in this part. The force calculated by the developed grinding force model is given to the dynamic model of the hybrid redundant manipulator and the torque in the critical joint is calculated by the dynamic model. In redundant manipulators, there are infinite inverse kinematics solutions. In this thesis a configuration generation approach for 12 DOF hybrid redundant manipulator is proposed. Based on the workpiece geometry and desired grinding geometry, the tip point location and orientation in the robot workspace are obtained. For

the obtained location and orientation and for a given grinding force by the force model, the configuration generation algorithm is implemented and generates various configurations for redundant manipulator. A search algorithm is used in order to find the optimum posture that leads minimum torque in the critical joint of the hybrid manipulator. Also in this part a method is proposed in order to find optimum orientation for surface grinding in the work space. In this method, instead of giving tip orientation to the optimization algorithm, the search approach finds the optimum tip orientation in parallel with optimum posture of the manipulator. The simulation results showed that it is possible to minimize the computed torque of a desired joint in redundant manipulators using true posture of the robot. Based on the proposed posture optimization method and based on proposed grinding force model, it is possible to generate an optimum path for the robot during grinding operation.

1.3 Outlines of the Thesis

A brief information related to the motivation, objectives, contributions and outline of this thesis are given in the first chapter. The detailed presentation of each part of the thesis are explained in the following chapters. There are five chapters in this thesis.

In the second chapter contains detailed steps of developing a hybrid model based on energy and experimental methods for parallel hexapod-robotic light abrasive grinding operations. In this chapter the detailed introduction and literature survey about physical and empirical grinding force models and robotic grinding operations are presented. The steps of robotic surface grinding model development are also explained. The detailed explanation of an energy-based model of surface grinding forces is presented followed by the procedure of penetration tests and feature selection algorithm. The penetration tests are used for extracting new features related to the mechanical properties of the grinding setup and workpiece. Afterwards, grinding force model improvement with a refining term is explained. The refining term optimizes the energy-based model for robotic

grinding operations. The experiments results and a discussion about them are also given in second chapter. In the second and third chapters, the just parallel hexapod is considered as grinding robot and serial manipulator is assumed as a locked rigid body.

The third chapter is related to development of a high performance parallel hexapod-robotic light abrasive grinding using real-time tool deflection compensation and constant resultant force control. In this chapter the detailed introduction and literature survey about constant force control and different control methods in robotic grinding are presented. Afterwards the effects of tool deflection on robotic surface grinding forces are investigated. The experimental setup and technical details of tool deflection modeling are also given in this chapter. Based on such a model for tool deflection a kinematic solution for tool deflection compensation is presented. Then a constant resultant force control approach using model supervised fuzzy controller is presented. In this supervised control approach, the developed force model in Chapter 2 is used for reference input generation that is given to a fuzzy controller in order to keep the resultant grinding force constant during the operation. The results of implementing the tool deflection compensation and resultant force control in parallel are given in this chapter. The results show the effectiveness of this methods in increasing the accuracy of the operation and preventing the geometrical errors on workpiece cross-section.

The fourth chapter is related to the kinematic/dynamic analysis and posture optimization of a 12 DOF hybrid redundant manipulator. In this chapter an introduction and literature survey about applications of the hybrid manipulators in machining operations are presented. Then the kinematic/dynamic analysis and simulation of the ABB IRB2000 manipulator are explained. Afterwards the kinematics and dynamic analysis of the parallel hexapod are given. Finally a novel method for posture optimization and path generation of 12 DOF hybrid redundant manipulator based on computed torque minimization of wrist joint is presented. In this part the simulation results of such an optimization show the capability of proposed method in minimization of wrist torque.

In the fifth chapter a general conclusion of this thesis, and possible future works on upcoming tasks are presented. References are also provided in the Reference section.

CHAPTER 2

HYBRID MODEL BASED ON ENERGY AND EXPERIMENTAL METHODS FOR PARALLEL HEXAPOD-ROBOTIC LIGHT ABRASIVE GRINDING OPERATIONS

Automatic grinding using robot manipulators requires simultaneous control of the robot endpoint and force interaction between the robot and the constraint surface. In robotic grinding, surface quality can be increased by accurate estimation of grinding forces where significant tool and workpiece deflection occurs. In this chapter a novel grinding force model is proposed that is optimized for the robotic grinding operation. The model considers setup and workpiece mechanical properties using several features that are extracted from penetration tests. Also the percent load of the spindle which is a function of spindle current is used in the proposed model.

2.1 Introduction

Grinding is a finishing operation that is used for obtaining high surface quality and high accuracy of dimension. The exerted force is an important factor that greatly affects the grinding operation and resulting surface quality. Constant force control in the normal direction is a potent way to obtain small and uniform chips, leading to improvements in surface quality in machining operations. Without a force sensor, grinding force estimation is an important means of controlling the process. An accurate force estimation model provides assistance in robotic precision grinding operations.

Grinding operation is a complex process and susceptible to workpiece shape and material as well as robot type and configuration. Large number of characteristic quantities have influence upon grinding normal and tangential forces. In addition to the tool and workpiece types and materials, the depth of cut, spindle speed, and feed-rate are well-known grinding parameters that affect force. Considerable researches in development of grinding force models were made by researchers. The main aim of these researches is to predict the grinding normal and tangential forces as a function of grinding parameters.

2.2 Literature Survey

2.2.1 Grinding force models

Grinding models can be classified into two main branches: physical and empirical models [94]. Empirical models are based on experimental results. The physical models are based on physical laws and mathematical relationships between input and output parameters. Physical models are more general, but empirical models are more accurate in certain experiment conditions [11].

2.2.1.1 Physical grinding force models

Physical grinding models are derived from operation attributes, process variables, physical laws and physical assumptions. These types of models can be derived from analytical or numerical approaches. The material removing process in grinding can be considered to be an interaction between many small abrasive edge elements and the workpiece. An analytical force model considering single edge grit individually and extending the results for all active abrasive grits was proposed by Azizi et al. [6]. The effect of kinematic parameters and grinding surface characteristics like number of active grits and their sharpness were included. However, elastic deformation of the tool, workpiece and setup were not considered. Aslan et al. [5] proposed a semi-analytical grinding force

model using micro milling analogy and modeling geometrical characteristics of the individual grits. The grit distribution on the wheel and the interaction with the workpiece was investigated. Also the important parameters like shear stress and friction coefficient between the workpiece and grits were included in the model. Temperature measurement were done during experiments in order to obtain shear stress using Johnson-Cook formula. The setup and grinding wheel assumed stiff enough in this research. Based on a single grain force model, a new grinding model was generated by Wang et al. [95]. These researchers analyzed grain trajectory and interaction between grain and the workpiece in order to find critical grain penetration depths that cause sliding, cutting and plowing behaviors. The used setup was composed of a CNC machine and an alumina wheel with 15.24 *cm* diameter. Due to such a stiff setup, the effect of the tool deflection was not mentioned in this research. The maximum error between experimental and predicted normal/tangential grinding forces were 9.1% and 10% respectively. Hecker et al. [38] proposed a method for prediction of grinding power and force based on the probabilistic distribution of unreformed chip thickness. These researchers used kinematic and dynamic analysis of the process and incorporated the material properties and wheel micro structure in their model. They also considered elastic deformation of the tool and workpiece on the contact length. A model based on static and dynamic chip formation energy was proposed by Tang et al. [91], and formulas for chip formation forces and sliding forces during the grinding operation were calculated without considering tool deflection and stiffness effects. This model is investigated in Chapter 2.3.1 in detail. Dynamic grinding models were proposed as a function of material removal rate (MRR) in [48]. A 25% relative error on the mean forces values were observed comparing the model outputs and experimental data. In this model the contact stiffness between the wheel and workpiece is modeled as a single spring. However, the stiffness of the setup elements are not considered. Cohesive zone based finite-element method was used by Feng et al. [28] for modeling the grinding of ceramic materials. The results of normal forces prediction were more accurate in comparison with the tangential forces prediction.

They investigated the effect of tool deflection especially on tangential grinding forces. The tool deflection effect on tangential forces was modeled as a function of stiffness and friction coefficients and difference between SDOC and ADOC. The new function improved the model performance in prediction of tangential forces but they did not consider the tool deflection effect in normal direction.

2.2.1.2 Empirical grinding force models

The empirical force models are based on collecting data from experiments and finding relationships and patterns between inputs and reaction forces. The relationships and patterns are not necessarily mechanistically relevant. Artificial neural networks (ANN) and regression techniques are common methods for making an empirical model. An empirical force model was generated by Guo et al. [32] using a CNC machine and parameters like feed rate, wheel speed and dynamic depth of cut. The model describes amplitude and frequency properties of the grinding force. They used linear regression approach in their study for making the model from experimental data. The mechanical properties of the material and setup such as their deflection and elastic deformation were not considered. The comparison between developed force model and experimental data showed that the error deviations were within acceptable range. Amamou et al. [3] proposed an ANN model in order to predict the specific tangential and normal grinding forces by determination of an optimal ANN input set. The average percentage of the deviation from the validation experiments was equal to 7.84% using the developed ANN model. A hybrid model based on genetic algorithm (GA) and artificial neural networks was generated for optimization of process parameters in NC camshaft grinding [22]. The absolute maximum error was less than 17.44%. The evaluation of the result showed that absolute maximum error was less than 17.44%. Also the 85.42% of the predicted values had error ranging between $\pm 10\%$.

2.2.2 Robotic grinding

Automatic grinding systems have been investigated for years to mimic the adaptive nature of human intelligence in order to replace manual grinding, which is labor-intensive and not productive. Force-position control is a common technique when grinding with robots, where the end point of the manipulator must be controlled together with force interaction between the manipulator and workpiece. Robotic disc-grinding operations were investigated by Dai et al. [21], and a linear autoregressive moving average with exogenous variable model of the fourth order (ARMAX) was generated. This model was used to develop an adaptive pole placement controller in order to regulate the normal grinding force. The average measured forces during their experiments were not constant. These researchers estimated that changing the grinding force is due to the setup error, robot error or stiffness change in different configurations of the robot. The model was a relation between depth of cut and normal grinding force. The effects of wheel speed, feed rate and stiffness of the setup were not investigated. An experimental study was performed by Tahvilian et al. [90] for coefficient determination of a semi-analytical grinding force model, where a flexible robot was used as a tool holder. These researchers investigated the number of impact cutting actions per wheel turn at various grinding power levels. Using the measured power, MRR and wheel speed, the coefficients of the force model were identified. The stiffness of the setup, workpiece properties and deflection effects were not considered in this research. The stiffness of the robot structure can affect grinding model accuracy where it depends on the current position of the robot axes, as well as direction of movement. This effect is especially pronounced when dealing with the difference between the set depth of cut (SDOC) and actual depth of cut (ADOC); the stiffness of the machine, the tool-workpiece contact stiffness and grinding stiffness (cutting stiffness) must be investigated. An analysis of the SDOC and ADOC was performed by Zhang et al. [103], where a fixture was used for fixing the workpiece, which enabled the machine stiffness to vary in a desired range. In that study, for a given stiffness value that was a result of the fixture set, the SDOC and ADOC were observed and investigated using

a multi-pass method. The results demonstrated that for higher stiffness values, the ADOC is closer to the SDOC.

Robotic grinding machines have lower stiffness in comparison with universal grinding machines. This issue leads to dimensional errors and decreases the machining accuracy. The stiffness factor can be categorized as manipulator, workpiece and tool stiffness. In the literature, several techniques were used in robotic machining operations to decrease effect of errors and increase dimensional accuracy and surface quality by considering the stiffness. The elemental errors were categorized, weighted and introduced to the homogenous transformation matrix of a multitasking machine using the Denavit – Hartenberg approach in Ref. [24]. The origin of these errors can be traced to such parameters as the stiffness of the tool and robot cutting tool deformation and geometric or kinematic errors. These researchers defined errors as additional geometric factors in the kinematics of the robot. Position error during robotic deburring with constant normal force was investigated in Ref.[87]. To prevent position error, excessive contact force and workpiece damage, an impedance controller was implemented with respect to the robot stiffness. One of the important focuses in the literature is investigation of tool deflection effects on machining. Due to the nature of robotic machining where tiny drill bit tools are used, machining forces and surface quality are greatly influenced by tool deflection. Correlations between tool position in the space and three cutting force components (coordinates X, Y, and Z) were used for more useful diagnosis of the machining test [59]. The data were collected and processed in order to extract the relationship between cutting forces and their actual point of effect in the space. Such a relationship reflects the deflection amount of the tool. Due to uncertainty in the physical models, empirical models are preferred for prediction of the tool stiffness [4]. An empirical research is described in Ref.[56] in order to study the effect of workpiece inclination, tool slenderness, and cutting strategy on tool deflection during high speed milling. The results showed that proper selection of the tool and milling strategy can decrease tool deflection.

Considering the entire system stiffness (tool, workpiece and hexapod stiffness) to be an important parameter, a novel grinding force model is derived in this study and optimized for robotic grinding. A physical model plus a refining term was used. The refining term indirectly includes the mechanical properties of the setup and workpiece. In addition to the common grinding variables, such as spindle speed, depth of cut, and feed rate, feedbacks from the spindle were used in the refining term of the surface grinding force model. The details of the grinding model are explained in the next section. The performance of the proposed model in predicting the grinding forces is investigated, and a comparison between the proposed model and the physical model is performed.

2.3 Development of Robotic Surface Grinding Model

The aim of the grinding model is to predict the normal and tangential reaction forces coming from the work piece and acting on the tip point of the robotic machine tool. A precise model requires a pre-estimation of the reaction parameters. A path control strategy can be designed with respect to these reaction parameters in order to increase grinding operation performance. To generate a grinding model, an experimental setup was designed. The setup was composed of PI H-824 hexapod, ATI Gamma IP60 force/torque sensor, high-frequency BMR 222-42-MHM spindle, CBN ZY 4.0-5 B126 tool (overhang 25 mm), workpiece (St37 steel), tool changer and collets (Figure 2.1).

The setup enabled the implementation of a grinding operation under controlled-conditions and registered the incoming data from the spindle (current and load percent), force/torque sensor and the hexapod (position feedback). The 6 DOF parallel hexapod that is used in this study has $1.7N/\mu m$ stiffness in the normal direction (Z direction) and $7N/\mu m$ stiffness in tangential direction (Y direction). The normal and tangential axis of the hexapod are along Z and Y directions respectively that are shown in Figure 2.1. The repeatability of the hexapod in normal and tangential directions are $\pm 0.1\mu m$ and $\pm 0.5\mu m$ and the single actuator design resolution of the hexapod is $0.007\mu m$. Stiffness of the force/torque

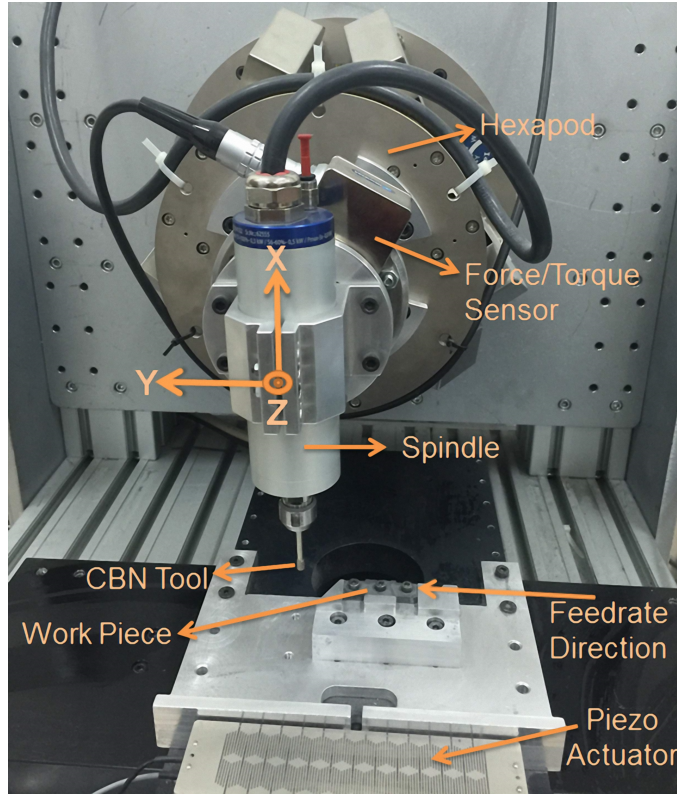


Figure 2.1: Experiment setup

sensor in normal and tangential directions are $18N/\mu m$ and $9.1N/\mu m$. The resolution of the Force/Torque sensor in its normal and tangential directions are $0.0125N$ and $0.00625N$. Head stiffness of the spindle is negligible. The hexapod and force/torque sensors are notably stiff, and they are sufficiently accurate to cover the range of parameters for the grinding experiments conducted in this study. An electro-spindle is used with maximum nominal output power of $300W$ and maximum rotation speed of 60000 rpm.

CBN abrasive mounted bits were used as a grinding tool in this study due to their high resistance against wear, heat dissipation properties and a dry working capability without any coolant [16] and [17]. Based on the data collected, the mechanics of the grinding process can be investigated, and a model of the grinding operation can be generated using analytical methods and data mining and pattern recognition techniques. A large number of parameters affect the

reaction behavior of the workpiece during grinding operations, such as material mechanical properties, stiffness of robot, stiffness of the spindle and toolset, feed rate, depth of cut, spindle speed, workpiece profile, and power of the spindle. As mentioned before, the robotic grinding setup has lower stiffness ($1.7N/\mu m$ in the z direction and $7N/\mu m$ in the y direction) in comparison with universal grinding machines ($60 - 100N/\mu m$ in the z direction and $30 - 60N/\mu m$ in the y direction) [55]. Therefore, the tool can be deflected during the operation. Tool deflection has a significant effect on the grinding operation. An example of robotic grinding with constant set depth of cut (SDOC) and spindle speed is shown in Figure 2.2. In surface A, grinding has been performed at a constant feed rate. On this surface, the tool could not reach to the SDOC due to tool deflection. When the hexapod reaches point B, feeding by the hexapod was stopped and the tool began to compensate its deflection. The tool continuously removes chips at point B, compensates the deflection and reaches the SDOC, as shown in the side and top views of Figure 2.2. Surface C is not machined in this figure.

In this study, we combined both physical and empirical methods for the generation of a comprehensive grinding model with a capability of extension to different grinding setups and workpiece materials. The steps of the grinding model generation are shown in Figure 2.3. Model generation included a refining term that was added to an energy-based surface grinding model (see section 2.3.1) in order to increase accuracy. The model uses a specific grinding energy, where its variables are classic grinding variables (spindle velocity, the depth of cut, feed rate and tool geometry). The coefficient of each term in a new equation was calculated with a linear regression approach with respect to experimental grinding data. The procedure for extracting the refining term equation is as follows: first, design of experiment (DOE) using the Taguchi method was performed and penetration tests were implemented through the DOE table. After implementing the penetration tests, the dimension of dataset increased, adding new extracted features from test results. Next, a feature selection algorithm was implemented to select the most correlated features with the desired out-

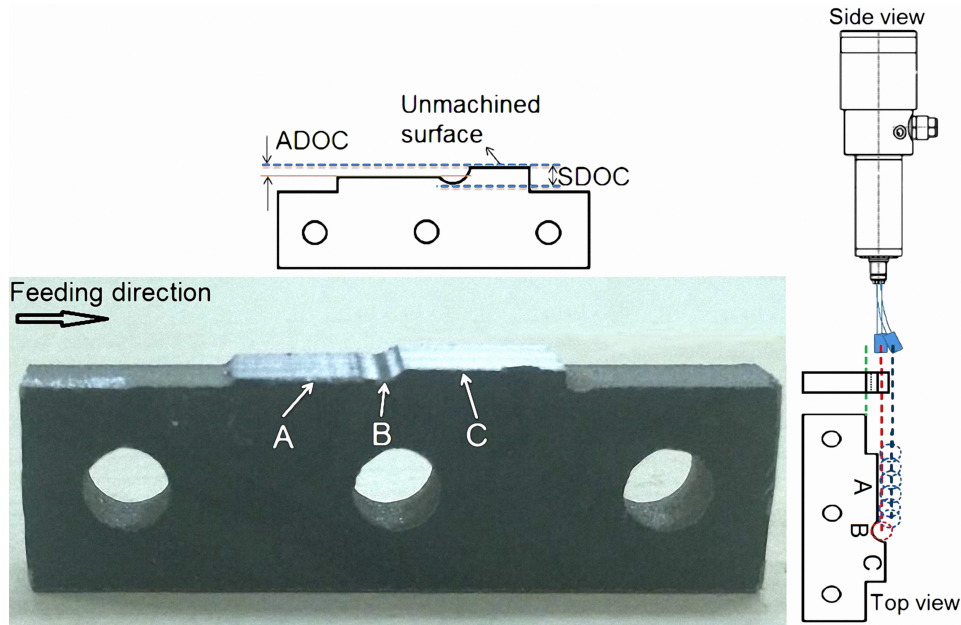


Figure 2.2: Robotic grinding with constant SDOC and spindle speed. A: Ground surface with constant feed rate where tool deflection happens, B: Ground point where hexapod is stopped (zero feed rate) without tool deflection, C: Unmachined surface

put (normal/tangential grinding forces). Finally, the refining term equation was generated as a function of the selected features. The resulting model is sensitive to setup, tool and workpiece stiffness. The accuracy of grinding forces prediction is improved using the new model in comparison with energy-based model prediction results.

2.3.1 Energy-based model of surface grinding forces

It is possible to define the grinding forces as a combination of two different forces. The first one is cutting deformation force, and the second one is sliding force. A cutting deformation force is composed of a chip formation force and a plowing force. The chip formation force is interaction force between the cutting edges of the tool and workpiece material when plastic deformation of workpiece occurs along rake face of the cutting edges. The sliding force is a result of

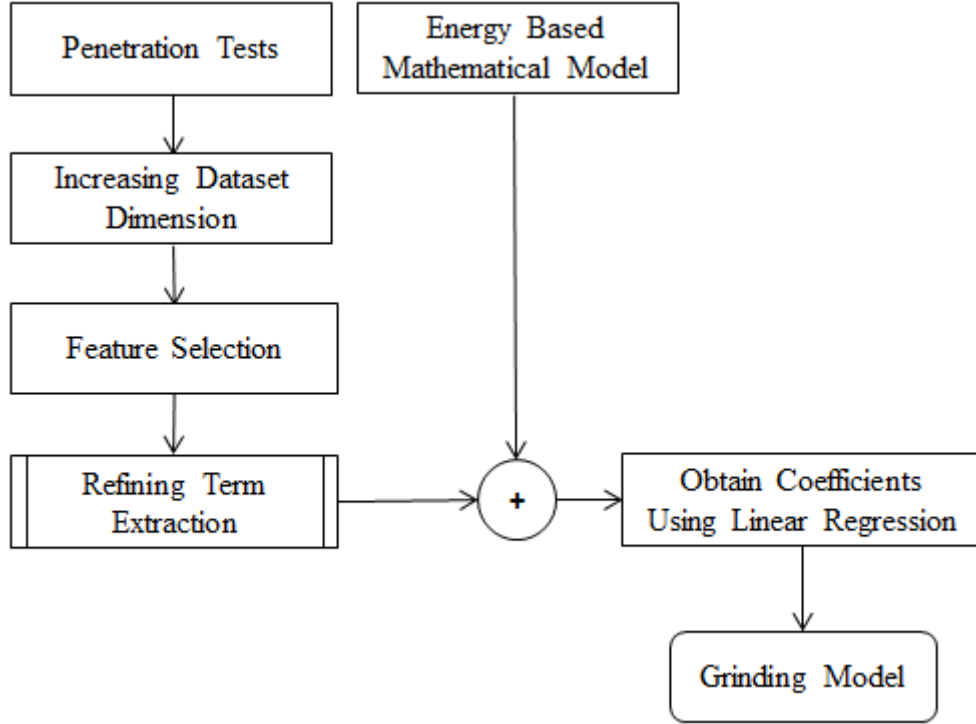


Figure 2.3: Grinding model generation steps

rubbing between the wear flats and the workpiece. The plowing force is a result of elastic reaction between flank surface of the tool and machined material. The plowing force do not contribute to removal of the chip. It is possible to neglect the plowing force because it is a notably small value in comparison with the chip formation force [63]. Therefore, the grinding force can be written as a summation of the chip formation and the sliding forces.

$$F_{Grinding} = F_{Chip} + F_{Sliding} \quad (2.1)$$

Specific grinding energy can be written as a combination of the chip formation specific energy and the sliding specific energy.

$$u_{Grinding} = u_{Chip} + u_{Sliding} \quad (2.2)$$

The chip formation specific energy is composed of two parts, static specific chip formation energy (u_s) and dynamic specific chip formation energy (u_d).

$$u_{Chip} = u_s + u_d \quad (2.3)$$

The static specific chip formation energy is constant and can be identified by experiments. The dynamic specific chip formation energy in the grinding operation is a result of both the strain rate effect and the thermal softening effect. Considering these effects, the u_d can be obtained using Eq. 2.4, where κ and $\dot{\gamma}_0$ are experimental constants. The parameter C is the number of effective abrasive blades of the grinding wheel in unit area, r is the chip width ratio to the chip thickness, d_e is an equivalent tool diameter, V_s is the tool wheel velocity, a_p is the depth of cut, V_f is the feed rate and c_2 is a constant coefficient [91].

$$u_d = c_2 \ln\left(\frac{\kappa (Cr)^{0.5} d_e^{0.25} V_s^{1.5}}{\dot{\gamma}_0 a_p^{0.25} V_f^{0.5}}\right) \quad (2.4)$$

The u_d equation can be written as a summation of two terms Eq.2.5. The first term includes only constant parameters and the second term includes variables. Both constant and variable terms of the u_d equation are multiplied by c_2 .

$$u_d = c_2 \ln\left(\frac{\kappa (Cr)^{0.5} d_e^{0.25}}{\dot{\gamma}_0}\right) + c_2 \ln\left(\frac{V_s^{1.5}}{a_p^{0.25} V_f^{0.5}}\right) \quad (2.5)$$

Using constant terms of u_{Chip} as c_1 :

$$c_1 = u_s + c_2 \ln\left(\frac{\kappa (Cr)^{0.5} d_e^{0.25}}{\dot{\gamma}_0}\right) \quad (2.6)$$

The chip formation specific energy can be expressed as follows [91]:

$$u_{Chip} = c_1 + c_2 \ln\left(\frac{V_s^{1.5}}{a_p^{0.25} V_f^{0.5}}\right) \quad (2.7)$$

The tangential chip formation force can be obtained from the specific chip formation energy using the following formula [64]:

$$F_{t,Chip} = \frac{u_{Chip} V_f a_p b}{V_s} \quad (2.8)$$

Parameter b is the tool width. Substituting Eq. 2.7 in Eq. 2.8, the tangential chip formation force will be as follows [91].

$$F_{t,Chip} = c_1 \left(\frac{b a_p V_f}{V_s} \right) + c_2 \left(\frac{b a_p V_f}{V_s} \right) \ln \left(\frac{V_s^{1.5}}{a_p^{0.25} V_f^{0.5}} \right) \quad (2.9)$$

The normal chip formation force formula is the same as a tangential chip formation force formula. The only differences are coefficients where c_1 and c_2 are multiplied by the static and dynamic ratio of the normal chip formation force to the tangential chip formation force [91].

$$F_{n,Chip} = c_3 \left(\frac{b a_p V_f}{V_s} \right) + c_4 \left(\frac{b a_p V_f}{V_s} \right) \ln \left(\frac{V_s^{1.5}}{a_p^{0.25} V_f^{0.5}} \right) \quad (2.10)$$

As shown in Eq. 2.1 the second part of the grinding force is sliding force. The tangential and normal sliding forces can be written as follows [64]:

$$F_{t,Sliding} = \mu \bar{p} b A \sqrt{a_p d_e} \quad (2.11)$$

$$F_{n,Sliding} = \bar{p} b A \sqrt{a_p d_e} \quad (2.12)$$

In Eq. 2.11 and Eq. 2.12, μ is the frictional coefficient, A is an area ratio of the grinding wheel's wear surface and \bar{p} is the average contact force between the

workpiece and the tool. The formulas of μ and \bar{p} are expressed in Eq. 2.13 and Eq. 2.14 where, α , ζ and p_0 are constant coefficients that can be determined by experiments [91].

$$\mu = \frac{\alpha V_s d_e}{4 p_0 V_f} + \zeta \quad (2.13)$$

$$\bar{p} = \frac{4 p_0 V_f}{V_s d_e} \quad (2.14)$$

Substituting equations 2.13 and 2.14 in equations 2.11 and 2.12 and simplifying the results, the sliding tangential and normal forces are obtained as follows.

$$F_{t,Sliding} = (\alpha A b) \sqrt{a_p d_e} + (4 \zeta p_0 A) \left(\frac{b V_f \sqrt{d_e a_p}}{V_s d_e} \right) \quad (2.15)$$

$$F_{n,Sliding} = (4 p_0 A) \left(\frac{b V_f}{V_s} \sqrt{\frac{a_p}{d_e}} \right) \quad (2.16)$$

In this study, the constant coefficients are determined by a linear regression approach. Therefore, it is possible to combine the experimental constant coefficients for each term in the equations. Considering:

$$c_5 = \alpha A \quad (2.17)$$

$$c_6 = 4 \zeta p_0 A \quad (2.18)$$

$$c_7 = 4 p_0 A \quad (2.19)$$

The tangential and normal sliding forces can be written as Eq. 2.20 and Eq. 2.21.

$$F_{t,Sliding} = c_5(b\sqrt{d_e a_p}) + c_6\left(\frac{bV_f\sqrt{d_e a_p}}{V_s d_e}\right) \quad (2.20)$$

$$F_{n,Sliding} = c_7\left(\frac{bV_f}{V_s}\sqrt{\frac{a_p}{d_e}}\right) \quad (2.21)$$

Finally, adding the chip formation and sliding forces as given in Eq. 2.1, the general form of the grinding tangential force (F_t') and grinding normal force (F_n') are obtained.

$$\begin{aligned} F_t' = & c_1\left(\frac{b a_p V_f}{V_s}\right) + c_2\left(\frac{b a_p V_f}{V_s}\right) \ln\left(\frac{V_s^{1.5}}{a_p^{0.25} V_f^{0.5}}\right) \\ & + c_5(b\sqrt{d_e a_p}) + c_6\left(\frac{bV_f\sqrt{d_e a_p}}{V_s d_e}\right) \end{aligned} \quad (2.22)$$

$$\begin{aligned} F_n' = & c_3\left(\frac{b a_p V_f}{V_s}\right) + c_4\left(\frac{b a_p V_f}{V_s}\right) \ln\left(\frac{V_s^{1.5}}{a_p^{0.25} V_f^{0.5}}\right) \\ & + c_7\left(\frac{bV_f}{V_s}\sqrt{\frac{a_p}{d_e}}\right) \end{aligned} \quad (2.23)$$

The above force model is based on specific grinding energy without considering the mechanical properties such as stiffness of the setup and the possible deflection of the tool and setup during robotic grinding. Therefore, it is necessary to improve the model.

2.3.2 Penetration tests

To improve the energy-based grinding force model, we conducted several penetration tests and extracted the material and setup mechanical properties from the test results. The extracted characteristics are used for the identification of

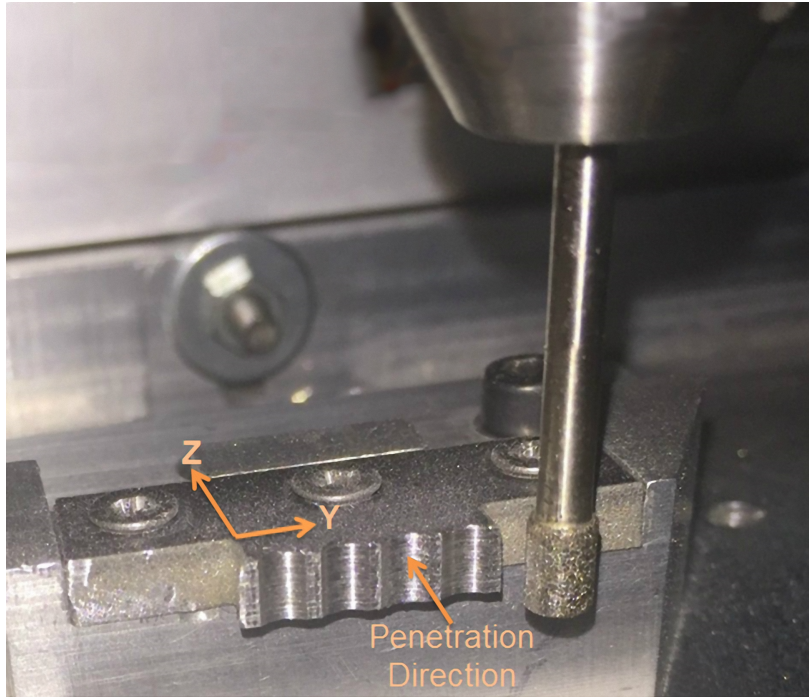


Figure 2.4: Penetration tests example

the model parameters. In the penetration test, the tool enters the workpiece axially, similar to a slot grinding operation, where the feed direction is normal to the workpiece surface. In Figure 2.4, four penetration tests on a workpiece are shown. The DOE methodology is used before implementing the penetration tests. Based on our setup and spindle capabilities, four different levels were defined for each grinding parameter (spindle speed, depth of cut and feed rate). For spindle speeds, 10000, 20000, 30000 and 40000 rpm were used. For the depth of cut, 150, 300, 450 and 600 micro meters were selected. For a feed rate considering the working conditions of the hexapod, the values of 0.2, 0.4, 0.6 and 0.8 mm/s were selected. Using Taguchi's method, a set of experiments was designed, which is shown in Table 2.1.

In the study, forces, spindle position feedbacks from hexapod, spindle current and spindle percent load were registered during the experiments. The data set dimension was increased by adding extra features that were extracted from the

Table 2.1: Design of experiment Taguchi method

Expeiment No	$a_p(\mu m)$	$\omega_s(\text{RPM})$	$V_f(\text{mm/s})$
1	150	10000	0.2
2	150	20000	0.4
3	150	30000	0.6
4	150	40000	0.8
5	300	10000	0.4
6	300	20000	0.2
7	300	30000	0.8
8	300	40000	0.6
9	450	10000	0.6
10	450	20000	0.8
11	450	30000	0.2
12	450	40000	0.4
13	600	10000	0.8
14	600	20000	0.6
15	600	30000	0.4
16	600	40000	0.2

collected data. These new features enabled us to obtain valuable knowledge about workpiece mechanical properties, stiffness of the setup and tool deformation in different experiment conditions. For each experiment with a certain a_p , V_f and V_s , if the tangential or normal force is plotted in the time domain, a graph similar to Figure 2.5 is obtained. Several valuable features can be extracted using such a graph. There is a peak time and a corresponding peak force value in the graph. This peak occurs when the hexapod reaches the desired cutting depth, while the tool is still reaching the SDOC. In an ideal condition when the grinding robot and tool are sufficiently stiff, and negligible deformation happens, the force value should fall to zero immediately at the point where SDOC is reached, which corresponds to the peak point in the penetration test.

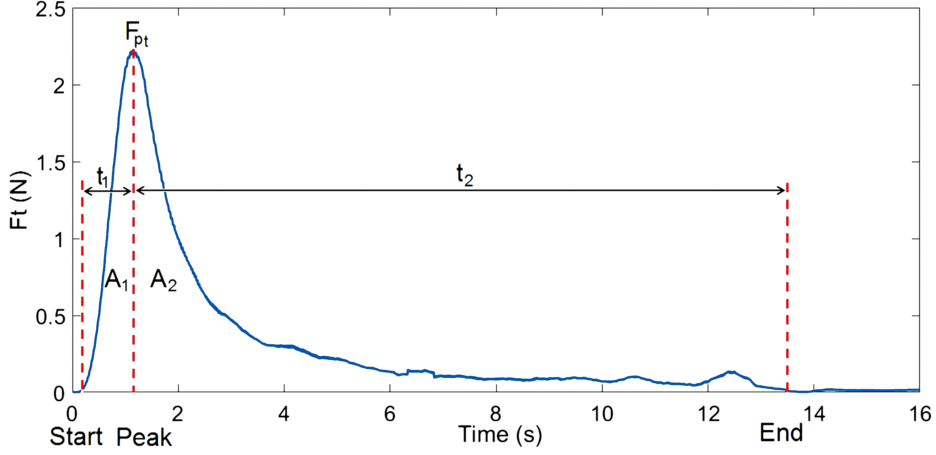


Figure 2.5: Tangential force profile of a penetration test in the time domain

In real conditions, when the tool enters the workpiece, it starts to be deformed and follows the hexapod motion with a delay. A continuous increase in the force value is observed at this stage. When the hexapod reaches the SDOC, feeding is stopped, which is the state at which that peak force value occurs. After this state, in spite of the zero feed rate, the deformed tool still removes chips until it compensates its deformation and reaches the vertical position. Therefore, the force value follows a parabola in the descending section of the graph (Figure 2.5). By investigating the force graph of the penetration test, it is possible to extract new features that are correlated with workpiece properties and setup stiffness. Therefore, the start time, peak time, end time, ascending period (t_1) and descending period (t_2) of the graph, peak force value (F_p), an area between the start and peak time (A_1) and an area between the peak time and the end time (A_2) were extracted as new features. The features were extracted for the tangential and normal force graphs. The symbols of all extracted features and their descriptions are shown in Table 2.2.

After increasing the data dimension, a feature selection algorithm was implemented to select the most correlated features with the desired output. For this purpose, a merit was calculated for each feature subset. Next, the subset that had higher merits were selected as inputs to the grinding model. A correlation-

Table 2.2: Descriptions of the extracted features

Symbol	Description
a_p	Depth of cut
d_e	Tool diameter
A_{1ft}	Area under F_t graph from start time to peak time
A_{1fn}	Area under F_n graph from start time to peak time
A_{2ft}	Area under F_t graph from peak time to end time
A_{2fn}	Area under F_n graph from peak time to end time
ΔA_{ft}	$A_{1ft} - A_{2ft}$
ΔA_{fn}	$A_{1fn} - A_{2fn}$
F_t	Tangential grinding force
F_n	Normal grinding force
F_{pt}	Peak F_t value
F_{pn}	Peak F_n value
I_s	Spindle current
L_p	Percent load of the spindle. If the spindle is not loaded and no defect exists, the L_p will equal to 0%
L_{pmax}	Peak L_p value of penetration test
t	Elapsed time while grinding
t_{1ft}	Start to peak period of t- F_t graph (ascending period)
t_{2ft}	Peak to end period of t- F_t graph (descending period)
t_{1fn}	Start to peak period of t- F_n graph (ascending period)
t_{2fn}	Peak to end period of t- F_n graph (descending period)
t_{pft}	Peak time of F_t graph
t_{pfn}	Peak time of F_n graph
V_f	Feed rate
V_s	Velocity of tool wheel periphery (m/s)
ω_s	Spindle speed (RPM)

based feature selection (CFS) is used for feature selection.

2.3.3 Feature selection

To obtain an accurate predictive model for a class feature, it is important to select the best predictors from a dataset. The best predictors stand for the features that are highly correlated with the class feature. In this study, the class features are normal and tangential grinding forces. So we need to select the most correlated features from our dataset in order to design a grinding force prediction model. A common method for calculating the feature-class correlation value is using Pearson's correlation coefficient. This method investigates each feature-class correlation individually. The weak point of this method is that it does not account for feature-feature correlations that can be classed as redundancy between features. Therefore both feature-class and feature-feature correlations should be considered during evaluation of a feature subset. It is necessary to use an algorithm that searches among the possible feature subsets and calculate a merit for them. The highest merit gives the best feature subset in order to use them for predictive model generation. CFS has a heuristic in order to determine the merit of the features subset with respect to capability of each feature for prediction of the class label, and the degree of redundancy between them [7]. "The heuristic is based on the following hypothesis. Good feature subsets contain features highly correlated with the class but uncorrelated with each other [25]. Eq. 2.24 formalizes the heuristic of CFS [36].

$$Merit_S = \frac{k \bar{r}_{cf}}{\sqrt{k + k(k-1) \bar{r}_{ff}}} \quad (2.24)$$

Eq. 2.24 presents the merit of a feature subset S that includes K features. \bar{r}_{cf} expresses the average of feature-class correlation, and \bar{r}_{ff} is the average feature-feature correlation [37]. The nominator indicates how predictive a subset of features is, and the denominator indicates the redundancy amount between the features. This process handles irrelevant and weak features and discards

Table 2.3: Selected subset with respect to the grinding forces using CFS

No	Selected subset Class feature: F_t	Selected subset Class feature: F_n
1	a_p	a_p
2	ω_S	ω_S
3	I_s	I_s
4	L_P	L_P
5	V_f	V_f
6	t_{1ft}	t_{1fn}
7	t_{2ft}	t_{2fn}
8	F_{pt}	F_{pn}
9	A_{1ft}	A_{1fn}
10	A_{2ft}	A_{2fn}

the redundant attributes which are highly correlated with one or more of the other attributes [34]. For continuous class data, the method that was used for computing the correlation between attributes was a standard linear (Pearson's) correlation. The n possible features generate 2^n possible subsets that testing all of this space is clearly time consuming, and impossible. Using CFS we could generate a matrix of feature-class and feature-feature correlations from training data and search in subset space with different search algorithms [35]. In the present study, a Genetic Algorithm (GA) search method was used. The cost function of GA was the calculated Merit of feature subset. The aim of the GA search was to find a feature subset with the maximum Merit [31]. The main advantage of CFS is that it can detect a correlation between features and eliminate the redundant features. This advantage improves the accuracy of the generated model. The CFS is implemented twice, considering tangential and normal grinding forces to be class features. The selected features for each class feature are given in Table 2.3.

Note that ΔA_{ft} and ΔA_{fn} are eliminated by CFS, because they are a function of the A_{1ft} , A_{2ft} , A_{1fn} and A_{2fn} parameters.

2.3.4 Grinding force model improvement with a refining term

At this step, the equations of refining terms (Δ_t and Δ_n) are introduced for tangential and normal forces. The outputs of the energy-based model are expressed in Eq. 2.22 and Eq. 2.23 as F_t' and F_n' . Therefore, adding a new refining term changes the general form of the proposed grinding force model as follows:

$$F_t = F_t' + \Delta_t \quad (2.25)$$

$$F_n = F_n' + \Delta_n \quad (2.26)$$

The parameters Δ_t and Δ_n are a function of selected features that are shown in Table 2.3. Among the selected features, there are classic grinding variables (a_p , ω_s and V_f) that are used in the energy-based model. Additionally, there are features from the penetration tests analysis (A_{1ft} , t_{1ft} , A_{2ft} , t_{2ft} , F_{pt} , A_{1fn} , t_{1fn} , A_{2fn} , t_{2fn} and F_{pn}). There are two important factors that are derived from the spindle data that are the spindle current and the spindle percent load (I_s and L_p). Both have a significant correlation with grinding forces. Their Pearson's correlation coefficients are approximately 0.9. Spindle percent load is a factor that reflects the spindle current during operation, and it varies between 0 and 100.

$$L_p = \frac{I_s - I_{s0}}{I_{s100} - I_{s0}} \times 100 \quad (2.27)$$

In this equation, I_{s0} is the spindle current without any load, and I_{s100} is the spindle current for a full load. These parameters are spindle characteristics, and they can be derived from the spindle datasheet or by experiment.

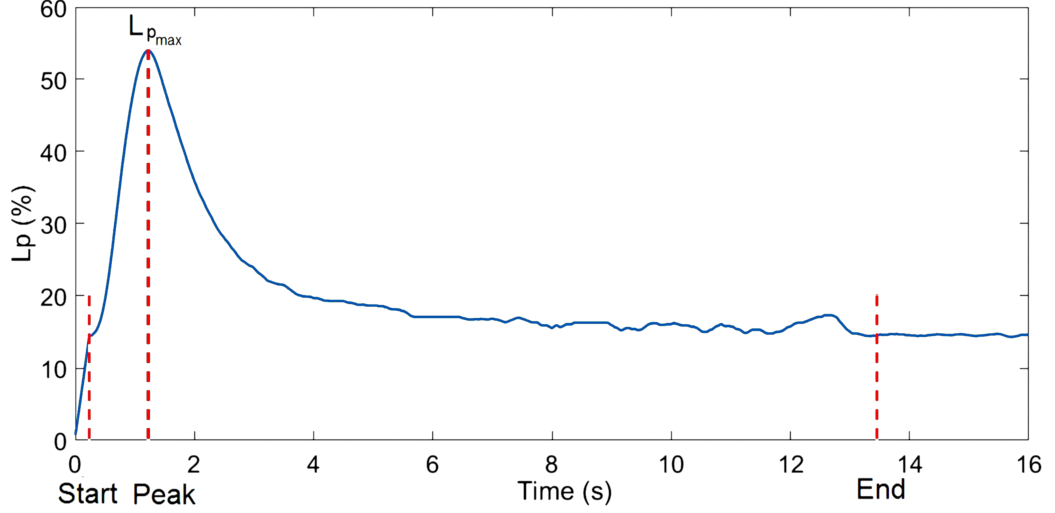


Figure 2.6: Spindle percent load in time domain during penetration test

An example of a percent load graph is shown in Figure 2.6 that is related to the penetration test shown in Figure 2.5. The same start, peak and end time of the force and percent load graphs and their similar patterns are obtained because of high correlation between grinding force and spindle percent load. The maximum value of the percent load graph ($L_{p_{max}}$) and the peak value of the force graph occur simultaneously. Note that there is approximately 16% load because of the tool and tool holder selected in this experiment. The spindle percent load includes both current information and spindle characteristics. Therefore, application of the spindle percent load instead of the spindle current enables the force model to be modified for different spindle types. The mechanical properties of the setup and workpiece are included in the proposed grinding force model using Δ_t and Δ_n . For this purpose, three items were defined as follows for derivation of Δ_t and Δ_n . These three items are correlated to the important parameters, such as stiffness of the setup.

$$\Delta_t = c_8 \left(\frac{A_{1ft}}{t_{1ft}} \right) + c_9 \left(\frac{A_{2ft}}{t_{2ft}} \right) + c_{10} \left(L_p \frac{F_{pt}}{L_{p_{max}}} \right) \quad (2.28)$$

$$\Delta_n = c_{11} \left(\frac{A_{1fn}}{t_{1fn}} \right) + c_{12} \left(\frac{A_{2fn}}{t_{2fn}} \right) + c_{13} \left(L_p \frac{F_{pn}}{L_{pmax}} \right) \quad (2.29)$$

- The first item of Eq. 2.28 and Eq. 2.29 is an average ascending force from the beginning of the penetration until the hexapod reaches SDOC and the end of feeding. This item reflects the average grinding force during penetration of the workpiece, and it changes with workpiece mechanical properties and stiffness of the setup.
- The second item is an average descending force from the end of feeding until compensation of the tool deflection and a zero reaction force. This item is highly correlated with the amount of tool deflection, and it reflects the average grinding force during compensation of the tool deflection to the vertical position.
- The third item is an estimation of the grinding forces using the spindle percent load. A linear relationship between the force and the percent load is assumed because of a high correlation coefficient of L_p . Therefore, in the third item, instantaneous L_p multiplied by the rate of the peak penetration force values to the peak percent load value of the penetration test L_{pmax} provides an estimation of the grinding forces in real time.

Substituting equations 2.22 and 2.28 in equation 2.25, the general form of the tangential grinding force model is derived. Substituting equations 2.23 and 2.29 in equation 2.26, the general form of the normal grinding force model is derived. The coefficients $c_1 - c_{13}$ are identified using a linear regression method. In the research, based on the parameters of Table 2.1, 16 surface grinding tests were conducted. The parameters of the proposed model were identified using the linear regression approach and the performance of the proposed model is shown.

2.4 Results and discussion

The general form of the proposed model is shown in the previous section. In this section, all necessary constant coefficients are calculated using the linear regression approach. Sufficient data samples are collected to implement the regression method. All grinding data samples of each experiment were cropped and merged together. The new database has more than 51000 data samples from different regimes. Implementing a linear regression technique on a database identified all constant coefficients of the model. The following equations were obtained for the grinding forces.

$$\begin{aligned}
 F_t = & -4.67 - 37.1 \left(\frac{b a_p V_f}{V_s} \right) + 0.505 \left(\frac{b a_p V_f}{V_s} \right) \ln \left(\frac{V_s^{1.5}}{a_p^{0.25} V_f^{0.5}} \right) \\
 & + 0.0228 (b \sqrt{d_e a_p}) + 1631 \left(\frac{b V_f \sqrt{d_e a_p}}{V_s d_e} \right) + 0.465 \left(\frac{A_{1ft}}{t_{1ft}} \right) - 1.15 \left(\frac{A_{2ft}}{t_{2ft}} \right) \\
 & + 0.311 \left(L_p \frac{F_{pt}}{L_{pmax}} \right) \tag{2.30}
 \end{aligned}$$

$$\begin{aligned}
 F_n = & -4.42 - 155 \left(\frac{b a_p V_f}{V_s} \right) + 10.5 \left(\frac{b a_p V_f}{V_s} \right) \ln \left(\frac{V_s^{1.5}}{a_p^{0.25} V_f^{0.5}} \right) + 2317 \left(\frac{b V_f \sqrt{a_p}}{V_s \sqrt{d_e}} \right) \\
 & + 1.49 \left(\frac{A_{1fn}}{t_{1fn}} \right) - 4.24 \left(\frac{A_{2fn}}{t_{2fn}} \right) + 1.79 \left(L_p \frac{F_{pn}}{L_{pmax}} \right) \tag{2.31}
 \end{aligned}$$

Units of parameters of the above model are given in Table 2.4.

Investigating the normal and tangential forces of the grinding experiments, three different surface grinding regimes were observed. These regimes are defined based on force change patterns during the surface grinding operation. By changing the stiffness of the grinding setup or by changing the grinding parameters (spindle speed, depth of cut and feed rate), one of the regimes can occur. In the first regime, forces remained almost constant during the operation (Figure 2.7). Grinding with very stiff machines, high spindle speed, low cutting depth and

Table 2.4: Units of parameters

Parameters	Unit
a_p	μm
V_f	mm/s
V_s	m/s
b	mm
d_e	mm

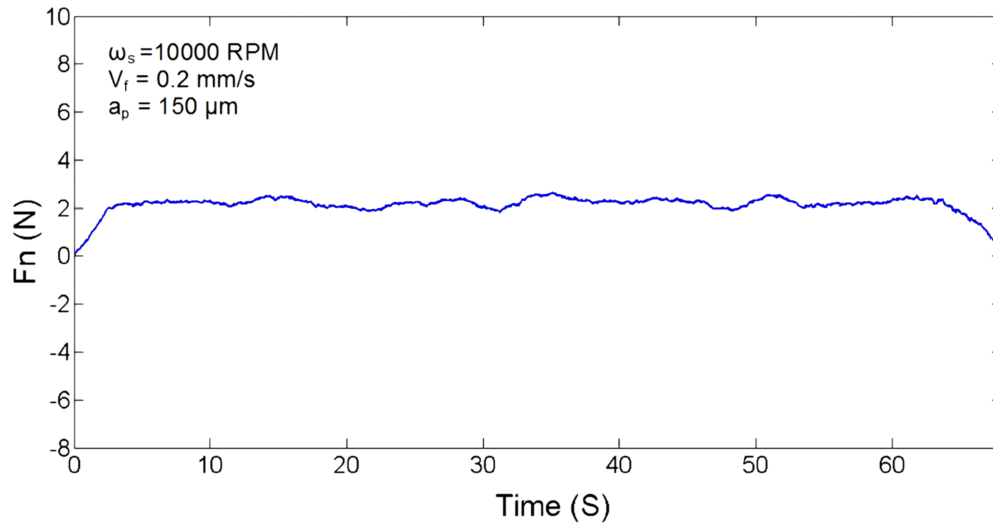


Figure 2.7: Example of the first regime robotic grinding

low feed rate are the factors that lead to constant grinding forces (first surface grinding regime).

In the second regime, the forces increased almost linearly during the operation (Figure 2.8). This regime is observed when significant tool deflection occurs. Grinding by machines with lower stiffness, such as robot manipulators, low spindle speed, high cutting depth and high feed rate, are the factors that lead to the ascending grinding forces (second surface grinding regime).

In the third regime, force fluctuations were observed during the grinding exper-

iment (Figure 2.9). This regime is a transition between the first and second regimes, where small tool deflections occur frequently during the operation.

In this research, the grinding parameters were kept constant during experiments. Note that when the grinding forces change in the experiment, the spindle percent load will also be changed. The examples of measured tangential and normal forces of grinding operations from the three regimes are plotted in Figures 2.10 - 2.15 with the proposed model and energy-based model outputs. The accuracy of a predicting model can be evaluated with its capability to predict the values close to the experimental data. Root mean square error (RMSE) is a factor to evaluate how well the model outputs fit the experimental data. Smaller value of RMSE means the model has predicted the values that are closer to the reality. Two different predicting models can be compared by calculation of their RMSE on an experimental dataset. To investigate the performance of the proposed model in comparison with the energy-based model, RMSE were calculated for both tangential and normal forces considering all 16 experiments and 51113 data samples. The RMSE of tangential and normal forces prediction are shown in Table 2.5. RMSE values of tangential and normal forces prediction using the proposed model are less than RMSE of same forces prediction with the energy-based model. It shows superiority of the developed model.

$$RMSE = \sqrt{\frac{\sum_{i=1}^n (F_{model} - F_{exp})^2}{n}} \quad (2.32)$$

In the RMSE formula, F_{model} is the model output, and F_{exp} is the experimental data.

The results shown in Figures 2.10 - 2.15 indicate the effectiveness of the proposed model in the prediction of the normal and tangential grinding forces, especially for the first and second regimes. For the data of regime 3, outputs of the developed model are close to the measured average force values. The proposed model shows significant improvement in grinding force prediction compared to the energy-based model, especially in prediction of the normal forces.

Table 2.5: RMSE of tangential and normal forces prediction over the total dataset using proposed model and energy-based model

Grinding forces prediction	RMSE value
F_t prediction with proposed model	1.1311 N
F_t prediction with energy-based model	1.1936 N
F_n prediction with proposed model	3.2377 N
F_n prediction with energy-based model	3.6590 N

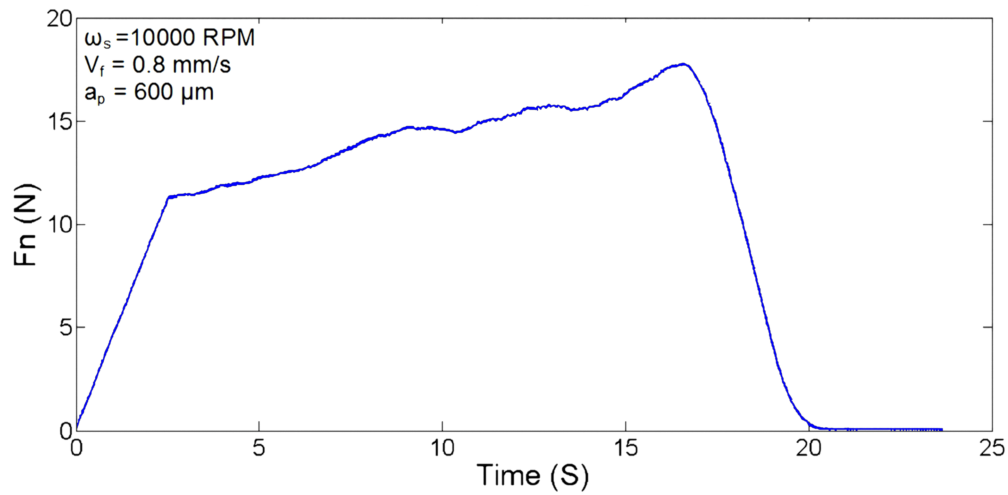


Figure 2.8: Example of the second regime robotic grinding

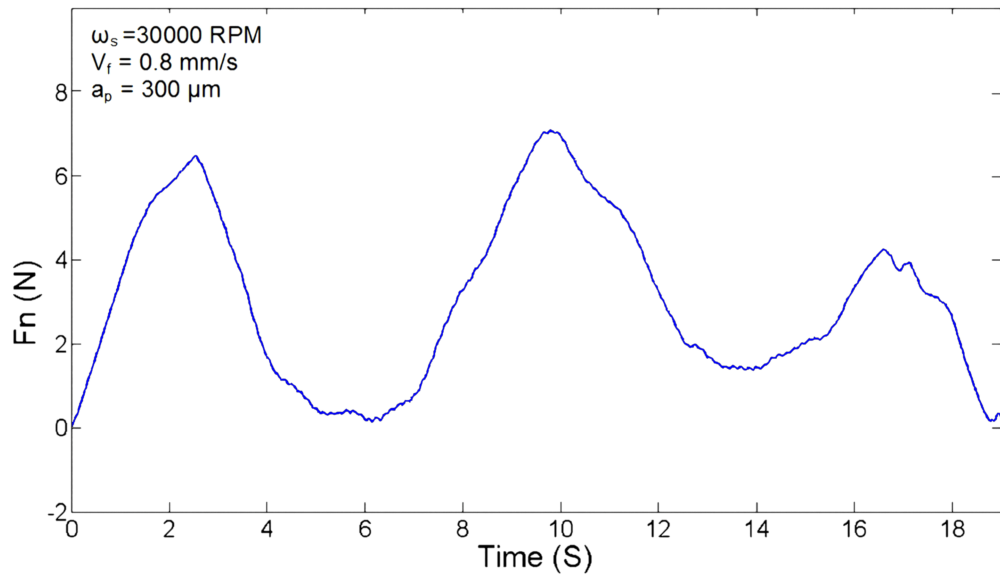


Figure 2.9: Example of the third regime robotic grinding

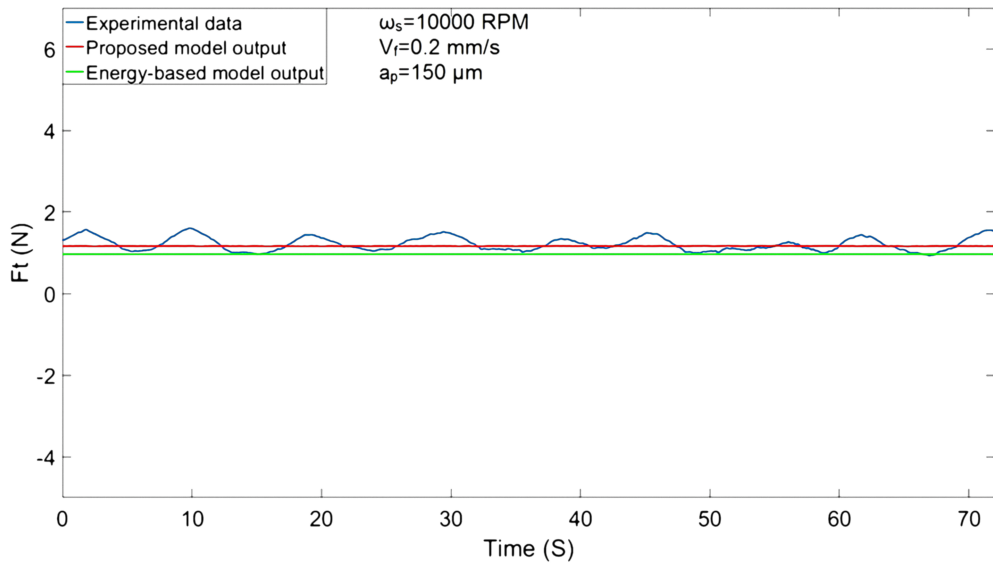


Figure 2.10: Regime 1 example. Tangential grinding force of experimental data (blue graph), proposed model outputs (red graph) and energy-based model outputs (green graph)

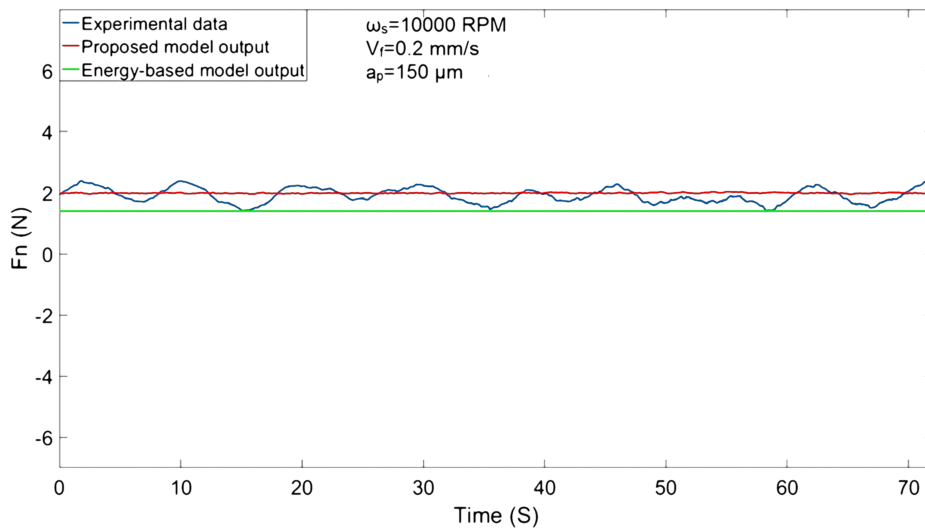


Figure 2.11: Regime 1 example. Normal grinding force of experimental data (blue graph), proposed model outputs (red graph) and energy-based model outputs (green graph)

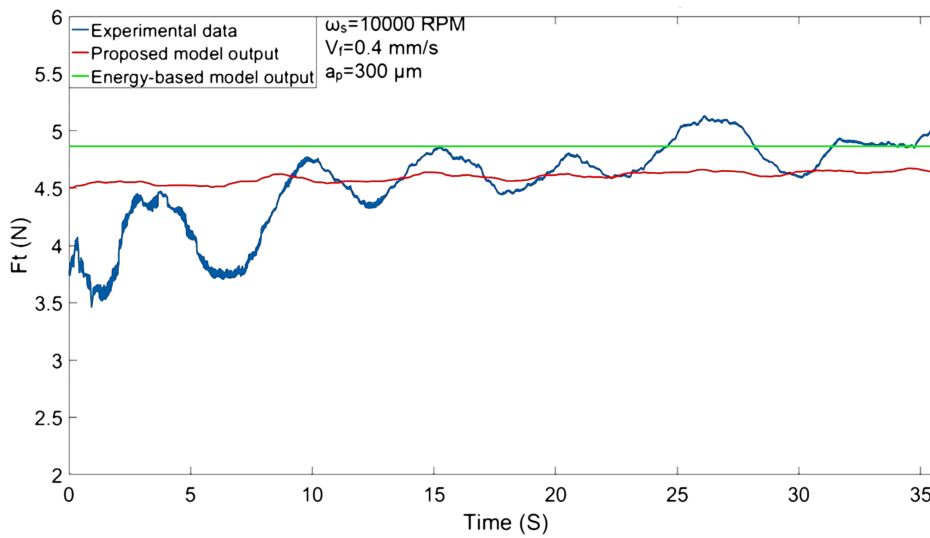


Figure 2.12: Regime 2 example. Tangential grinding force of experimental data (blue graph), proposed model outputs (red graph) and energy-based model outputs (green graph)

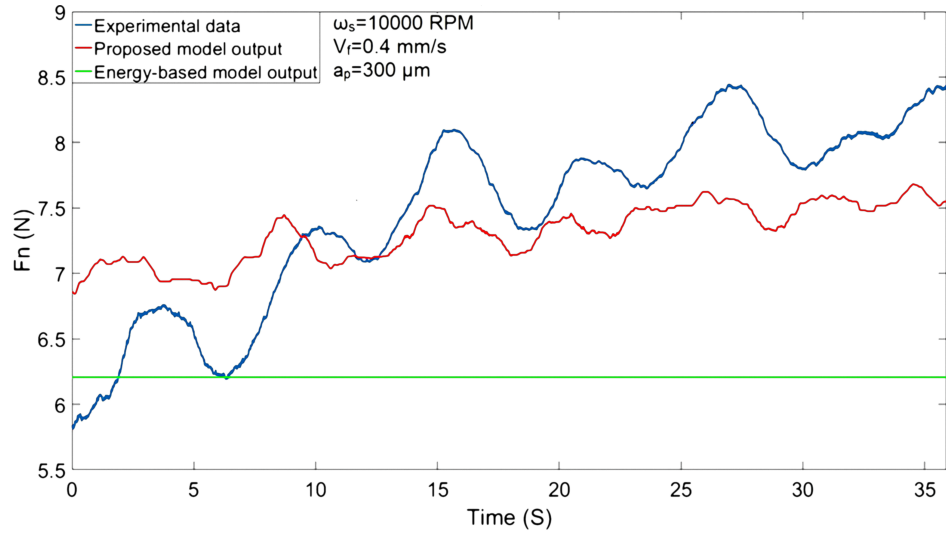


Figure 2.13: Regime 2 example. Normal grinding force of experimental data (blue graph), proposed model outputs (red graph) and energy-based model outputs (green graph)

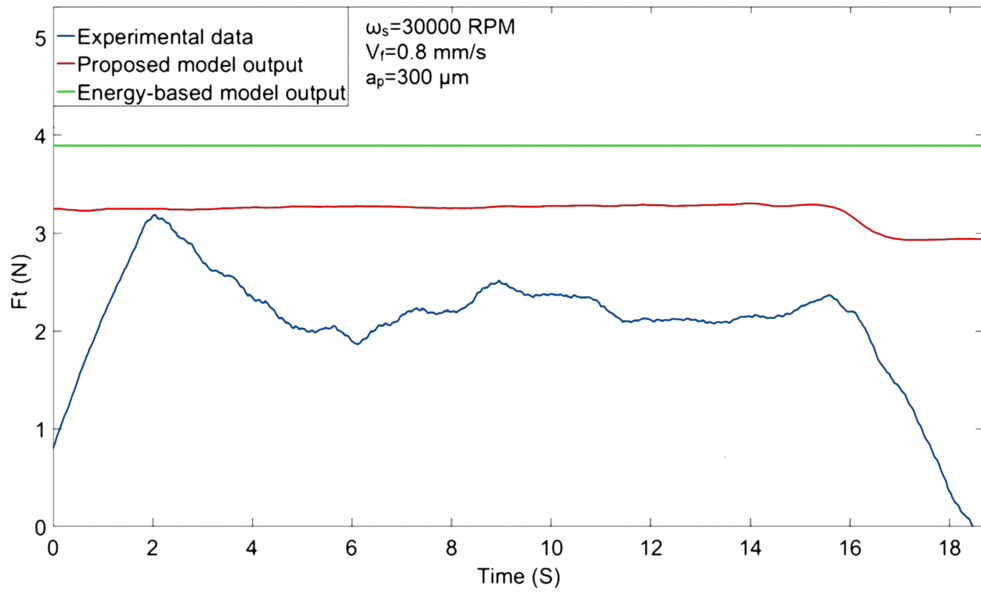


Figure 2.14: Regime 3 example. Tangential grinding force of experimental data (blue graph), proposed model outputs (red graph) and energy-based model outputs (green graph)

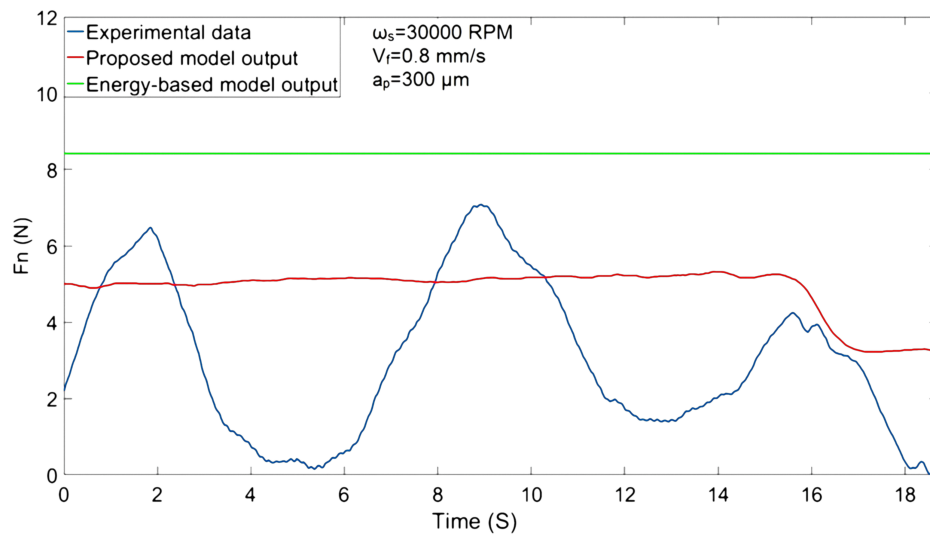


Figure 2.15: Regime 3 example. Normal grinding force of experimental data (blue graph), proposed model outputs (red graph) and energy-based model outputs (green graph)

CHAPTER 3

HIGH PERFORMANCE PARALLEL HEXAPOD-ROBOTIC LIGHT ABRASIVE GRINDING USING REAL-TIME TOOL DEFLECTION COMPENSATION AND CONSTANT RESULTANT FORCE CONTROL

In robotic grinding, significant tool deflection occurs due to the lower stiffness of the manipulator and tool, compared with operation by universal grinding machines. Tool deflection during robotic grinding operation causes geometrical errors in the workpiece cross-section. Also, it makes difficult to control the depth cut during the operation. In this chapter, an approach is developed for real-time calculation and compensation of the tool deflection in normal and tangential directions. Also a supervised fuzzy control method is developed for controlling the resultant grinding force in order to obtain constant depth cut during surface grinding process.

3.1 Introduction

Robotic machining systems have been researched for years to compromise between performance and flexibility for automated machining tasks such as grinding of jet engine turbine propellers. Despite providing great working capabilities on the complex paths of machining tasks, robotic machining setups have less stiffness compared with computer numerical controlled (CNC) machines. Tool deflection in robotic machining significantly affects the machining forces, machining accuracy and surface quality. The machining setup stiffness and effects

of setup, workpiece and tool deflections in the operation performance as well as techniques of handling these effects have been researched [61], [14], [58], [60] and [13]. In order to decrease dimensional errors due to the tool deflection in surface milling operations, a tool path selection method is developed in [57] based on minimization of tool deflection forces along the path. In this method, for three and five axis milling operations the paths that result minimum tool deflection cutting force, which is defined in the plane of the tool axis and the normal vector to the workpiece surface, are extracted. Implementing milling on these paths decreases dimensional errors. For three axis milling two options are proposed. The first is selecting a general path that minimizes the mean value of the tool deflection force and the second is selecting the various milling directions at each control node that results less tool deflection force and connecting these nodes together. For the five axis milling, both tool axis orientation and milling direction are considered in order to minimize the tool deflection force. In spite of higher accuracy choosing proper tool path, the authors did not propose any algorithm for compensation of the tool deflection. In [99], a method is proposed for minimization of vibrations and cutting forces during ball end milling of hardened steel. This method is focused on optimal selection of tool overhang and surface inclination in order to minimize the cutting forces and vibrations and improve the surface quality of machined workpiece. The results of this research show that increasing the tool overhang causes an increase of acceleration of vibration amplitudes. Also the results of this research indicate that increasing the surface inclination causes to decrease of cutting forces where the maximum value for cutting forces is obtained during slot milling with zero inclination. The surface inclination effect together with cutting speed effect are investigated in [98] during ball end milling of hardened steel. An optimum values are proposed for cutting speed and surface inclination for minimization of cutting forces. Such a minimization in cutting forces decreases the tool deflection and improves the machining accuracy. The focus of both of mentioned researches are on optimization of machining parameters with respect to the workpiece surface profile but compensation of the tool deflection is not considered. In ultra-precision

machining the effect of workpiece material properties are more important in comparison with conventional machining because the depth of cut changes in sub-micrometer range [27]. The effect of elastic recovery of workpiece material on surface roughness during ultra-precision milling is investigated in [96]. The results of this research revealed that the elastic recovery capability of workpiece material improves the surface finish in ultra-precision raster milling. The static stiffness of different points of workpiece are calculated and the surface topography of these points after precise turning are investigated in [70]. The results reveal the considerable effect of stiffness on surface roughness. In the most of the experiments, the surface quality are better at the points with higher stiffness and less deflection.

3.2 Literature Survey

There are several studies in the literature related to the compensation of tool deflection effects on workpiece. In this section, a review of the different strategies of these studies is presented. Most of the mentioned studies are related to end-milling operation. Kline et al. [44] proposed a method for predicting the amount of tool and workpiece deflection in end-milling operation based on cantilever beam theory. A force model and cantilever beam theory were used to obtain the amount of deflection. Similarly, Ryu et al. [83] investigated side mill machining operation and attempted to predict the errors caused by tool deflection. However, a solution for compensation of these errors was not presented. The effect of workpiece curvature on tool deflection and the resulting surface errors were investigated in [80]. A method based on path correction was proposed by Law et al. [47]. Their aim was to decrease tool deflection and its effect on the workpiece using optimum tool path. Approaches for path correction in end-milling operations were presented in [89], [23], [88] and [33] by adding an offset to the tool path. Cantilever beam theory was used to calculate the amount of tool deflection. Rao et al. [81] proposed an iterative approach instead of a single offset to compensate for offset error caused by tool deflection. However,

tool angle compensation was not investigated. A method for compensation of tool angle and tool displacement during end-milling operation was proposed by Yang et al. [100] where a proximity sensor was used for detecting tool deflection. A strong aspect of their research is that they considered both tool angle and tool tip displacement by compensating errors.

3.2.1 Constant Force Control

In recent years, force control during robotic machining has been significant for the proper execution of the operation tasks [102], [12]. In these tasks, the robot is controlled to maintain a given set force while the deflection of the robotic arm and cutting tool are major factors that should be considered. In [52], a force control system was designed to reduce the surface roughness by decreasing grinding force variation. A PID controller was used without considering tool and setup deflections during the process where the force sensor is mounted under the workpiece. A constant normal force control technique was developed by the authors. A normal force control on robotic grinding and deburring was investigated by Domroes et al. in [26]. They tried to maintain a constant normal force by adjusting the feed rate. However, they did not offer a systematic procedure for defining the reference force. Also, the stiffness of the setup and workpiece were not investigated. In [76], an adaptive control strategy for surface finishing was studied in which the goal was to track the desired motion in the tangential direction and regulate the desired force normal to the surface simultaneously. For this purpose, a dynamic model of the robot was generated. Using the dynamic model, a control scheme was developed that adapts the grinding coefficient, which is the relationship between the normal and tangential forces. The designed controller was tested on straight and curved surfaces. Thomessen et al. proposed a strategy to control the normal grinding force by simultaneously adjusting the position and feed rate of the tool [93]. Active control force feedback was used in grinding of large Francis turbines where the force sensor was located behind the end effector of the manipulator. However, a user-defined

reference force was used during experiments. Despite the large normal grinding force values, the effects of tool deflection and resulting errors on the sensor reference frame were not considered. An automatic grinding system using a hand grinder and a CNC machine was investigated by Liu et al. in [51]. Compliance of the grinding system was considered by modelling the stiffness of each component using a mass spring model. The real-time normal force feedback was supplied by a force sensor located under the workpiece. For normal grinding force control, a PID controller was used. A linear relationship between the cut depth and the normal force was assumed, and the slope of the cut depth–normal force graph was used as a stiffness of material removal process.

There are two options for the placement of force sensors for grinding operation. The first option is mounting the sensor under the workpiece. The advantage of this option is that there is no orientation between the sensor reference frame and workpiece reference frame. This means that the measured normal and tangential grinding forces by the sensor are real normal and tangential interaction forces between the tool and workpiece. However, in grinding of larger workpieces, it is not functional to use a sensor under the workpiece. The second option is placing the force sensor behind the spindle. This option is useful for industrial grinding applications using robot manipulators. But, in robotic grinding, due to deflection of the tool, there is an orientation between the sensor reference frame and tool reference frame. This means that the measured values for normal and tangential forces are not the real normal and tangential interaction forces between the tool and workpiece. In this study, the second option is selected for mounting the force sensor. In order to solve the problem caused by the tool reference frame orientation, the resultant grinding force was selected as a control parameter.

There is limited research on the effects of resultant force control in machining. An adaptive controller was developed by Budak to control the resultant force of milling operations [12]. A significant improvement was observed in the surface quality of the workpiece using the resultant force control algorithm. An adaptive

control strategy was used in [41] to maintain a constant resultant force while implementing robotic deburring. The proposed approach showed promising results in force/position tracking of an unknown environment. Although normal force control in robotic grinding is a research field that is often investigated, model supervised resultant force control is not studied in detail. In this study, model supervised resultant force control is studied in order to improve surface quality.

3.2.2 Control approaches

Designed linear controllers, such as PID, can be tuned and used in certain grinding conditions. However, due to the non-linearity of the grinding process, the mentioned linear controllers do not turn out a comprehensive solution. Fuzzy controller or a combination of fuzzy and PID controllers are preferable solutions for force control during grinding operations. A hybrid force motion control architecture is proposed in [65] for increasing robot autonomy. The performances of PI and fuzzy PI controllers were compared, and fuzzy PI controller showed better efficiency. A fuzzy controller is used for force control of a ceramic grinding (Al_2O_3) process in [62]. The results showed a more stable machining process when fuzzy controllers were used. Li et al. proposed an adaptive fuzzy control algorithm for hard sphere grinding [49]. Instead of a force sensor, a model was used to estimate the grinding force based on the spindle current indirectly. Based on the grinding force, the cut depth and spindle speed were controlled with a dynamic threshold-based fuzzy adaptive control approach. Although spindle current is used as a key factor for estimation of the grinding force, the obtained model cannot be used for different setups and spindles. This is because of the different characteristics of different spindles. The same current value can correspond to different grinding force bands when the spindle types are different. In our study, a factor called percent load is used in the grinding force model instead of spindle current. A fuzzy PID controller for grinding and deburring applications was generated in [92], [101]. The parameters of the PID controller were updated online at each sampling time by fuzzy rules.

In this study, a combination of a robotic grinding force model and a fuzzy control strategy is developed to maintain a constant resultant grinding force during robotic grinding operation. The grinding model used is optimized for robotic grinding applications considering the setup, tool and workpiece stiffness. As a result, a realistic reference force is generated for the fuzzy controller. Also, an approach is utilized for calculating tool deflection values as a function of grinding forces in the normal and tangential directions. A kinematic solution is proposed for real-time tool deflection compensation (TDC).

3.3 Effect of tool deflection on robotic surface grinding forces

Grinding with constant normal force and constant tangential velocity is a well-known approach for increasing operation accuracy and obtaining constant cutting depth and surface quality along the workpiece. However, the mentioned approach is effective when using universal grinding machines that are very stiff and the deflection of the tool and setup is negligible. In the case of robotic grinding, the stiffness of the robot and setup is lower than CNC type grinding machines. Consequently, there are considerable tool and setup deflections that have significant effects on the grinding forces. During grinding with CNC type machines, when there is a flat workpiece profile and the grinding parameters (depth of cut, spindle speed and feed rate) are constant, the grinding normal and tangential forces are expected to be constant. However, in robotic grinding, due to lower stiffness and tool-setup deflection, the grinding forces can show three different characteristics through the workpiece profile even when the grinding parameters are constant and the workpiece has a flat surface profile [46]. The three characteristics are classified in three regimes in Ref. [46]. In the first regime, the grinding forces remain almost constant because the tool is able to cut the workpiece at a constant feed rate (Figure 2.7). In the second regime, there is an almost linear increase in grinding forces because the tool cannot cut the workpiece at a constant feed rate and, consequently, tool deflection occurs (Figure 2.8). In the third regime, a transition between regime 1 and regime 2

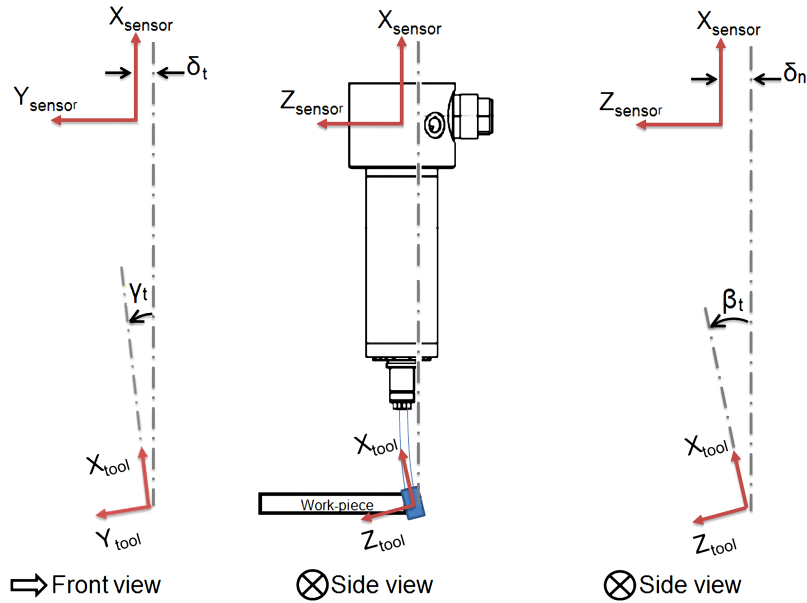


Figure 3.1: Orientations between the tool tip reference frame and force sensor reference frame

occurs with small tool deflection followed by immediate compensation (Figure 2.9).

The differences between the characteristics of robotic grinding and CNC grinding show the effects of tool deflection and setup stiffness on normal and tangential force behaviors. In grinding operations with force feedback, the force sensor is commonly mounted behind the spindle or behind the workpiece. If tool deflection occurs, an orientation occurs between the tool tip reference frame and the force sensor reference frame, as shown in Figure 3.1. This tool deflection can be expressed as two orientations around the Y_{sensor} axis (β_t) and Z_{sensor} axis (γ_t). In this case, the measured normal and tangential grinding forces are not the grinding forces of the tool reference frame because of the orientation. Force changes caused by the deflection cause an undesired variation of cutting depth along the workpiece. The other important effect of tool deflection is geometrical errors in the cross-section of the workpiece. The contact angle between the tool and workpiece changes the cutting depth in the cross-section of the workpiece.

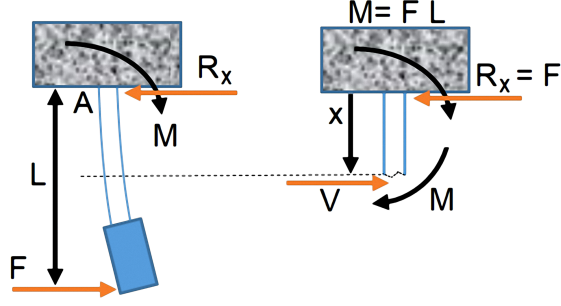


Figure 3.2: Tool modeled as a cantilever rod (left). Internal moment at x distance from the tool holder is shown (right)

3.4 Experimental setup

The experiment setup in this chapter is same as Chapter 2 (Figure 2.1). In addition to the 6-DoF parallel manipulator, the experimental setup has an additional 1 degree of freedom that is actuated by a piezo actuator. The actuator is fixed to the properly constrained table, presenting a single degree of freedom in the z -direction as shown in Figure 2.1. While performing grinding in the y -direction as shown in Figure 2.1, the machining errors can be reduced by admittance control-based negative compensation by the actuation of the piezo actuator.

3.5 Modeling tool deflection

In this section, the model developed for tool orientation and displacement in the normal and tangential directions is explained. The tool-workpiece interaction and their reaction parameters are shown in Figure 3.2. Assuming that the spindle and the robot are rigid and that the tool has a finite rigidity, the tool can be modeled as a cantilever rod where the internal moment at a distance of x from the tool holder (point A) can be represented as M .

To calculate the deflection and stiffness, the double integration method is utilized:

$$EI \frac{d^2\delta}{dx^2} = -M \quad (3.1)$$

where

E : Modulus of Elasticity

I : Moment of Inertia

δ : Displacement

x : Distance from point A

The following equilibrium equation can be written:

$$-Fx + FL + M = 0 \quad (3.2)$$

so,

$$M = Fx - FL \quad (3.3)$$

Substituting Eq. 3.3 into Eq. 3.1 and implementing the double integration method, equations 3.4-3.6 can be written.

$$EI \frac{d^2\delta}{dx^2} = FL - Fx \quad (3.4)$$

$$EI \frac{d\delta}{dx} = FLx - \frac{Fx^2}{2} + C_1 \quad (3.5)$$

$$EI\delta = \frac{FLx^2}{2} - \frac{Fx^3}{6} + C_1x + C_2 \quad (3.6)$$

where C_1 and C_2 are constants. Implementing boundary conditions:

$$\text{For } x = 0 \quad \left\{ \begin{array}{l} \delta = 0 \rightarrow C_2 = 0 \\ \frac{d\delta}{dx} = 0 \rightarrow C_1 = 0 \end{array} \right. \quad (3.7)$$

As a result:

$$\frac{d\delta}{dx} = \frac{F}{EI} \left(Lx - \frac{x^2}{2} \right) \quad (3.8)$$

$$\delta = \frac{F}{2EI} \left(Lx^2 - \frac{x^3}{3} \right) \quad (3.9)$$

Maximum deflection and slope occur at the end of the tool where $x = L$.

In normal direction, considering $F = F_n$, tool tip displacement (δ_n) and tool deflection (β_t) are obtained as Eq. 3.10 and Eq. 3.11.

$$\delta_n = \frac{F_n L^3}{3EI} \quad (3.10)$$

$$\beta_t = \frac{F_n L^2}{2EI} \quad (3.11)$$

In tangential direction, considering $F = F_t$, tool tip displacement (δ_t) and tool deflection (γ_t) are obtained as Eq. 3.12 and Eq. 3.13.

$$\delta_t = \frac{F_t L^3}{3EI} \quad (3.12)$$

$$\gamma_t = \frac{F_t L^2}{2EI} \quad (3.13)$$

3.6 Kinematic solution for tool deflection compensation (TDC)

In order to develop a kinematic solution for TDC, the exact position and orientation of the tool tip should be identified with respect to the hexapod reference frame. Then, it is possible to determine the new position and orientation for the hexapod aiming to compensate for geometrical errors caused by tool deflection. For this purpose, five reference frames are defined in the setup. The first reference frame (R_{base}) is the base reference frame, which is defined at the center

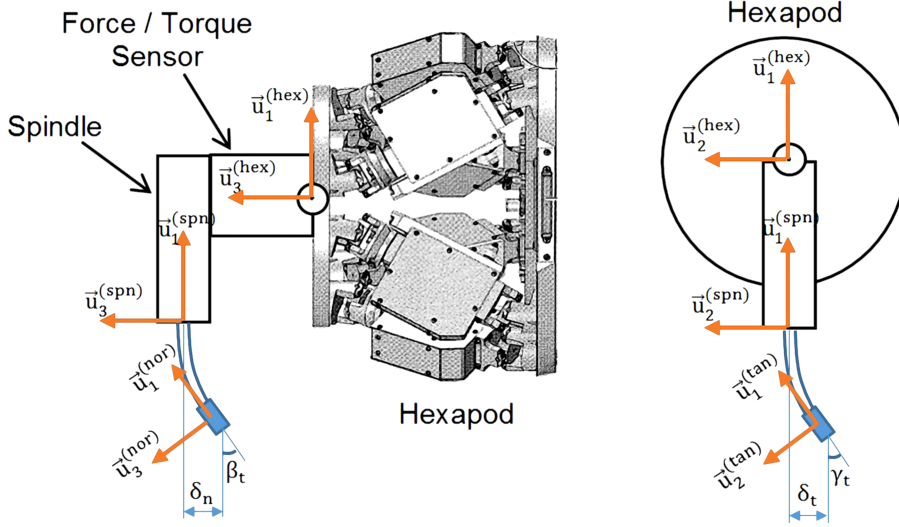


Figure 3.3: Illustration of the setup and assigned reference frames

of the hexapod top plate when it is in home position without any rotation or translation. R_{base} is fixed at this point and acts as the global coordinate system. The second frame (R_{hex}) is defined at the center of the top plate of the hexapod and moves with it. The third frame (R_{spn}) is defined as the tool holder of the spindle. The fourth and fifth reference frames (R_{tan} and R_{nor}) are assigned to the tool tip. The last two reference frames are related to the tool deflection in normal and tangential directions with respect to the R_{spn} . The side and front views of the setup and assigned reference frames are shown in Figure 3.3.

The reference frames from the base frame to the tool tip are shown in Eq. 3.14.

$$R_{base} \rightarrow R_{hex} \rightarrow R_{spn} \rightarrow R_{tan} \rightarrow R_{nor} \quad (3.14)$$

Let $C^{(i,j)}$ be the rotation matrix of the j^{th} reference frame with respect to the i^{th} reference frame.

In this paper, the rotation matrices are written as exponential rotation matrix in the general form of $e^{\tilde{u}\theta}$ as in Ref. [73], [74]. It expresses a rotation of an angle θ about axis n , which is a unit column matrix. Here, \tilde{u} represents a skew symmetric matrix corresponding to the unit vector n .

$$u = \begin{bmatrix} u_1 \\ u_2 \\ u_3 \end{bmatrix} \rightarrow \tilde{u} = \begin{bmatrix} 0 & -u_3 & u_2 \\ u_3 & 0 & -u_1 \\ -u_2 & u_1 & 0 \end{bmatrix} \quad (3.15)$$

The expansion of the exponential rotation matrix about axis n with angle θ is known as the Rodrigues formula, as in Eq. 3.16.

$$e^{\tilde{u}\theta} = I \cos \theta + \tilde{u} \sin \theta + uu^T (1 - \cos \theta) \quad (3.16)$$

Also, u_i is defined as the i^{th} basic column matrix, which is the column matrix representation of the i^{th} unit basis vector $\vec{u}_i^{(k)}$ in reference frame R_k that is its own reference frame [75].

$$u_i = u_i^{(k/k)} = \left\{ \vec{u}_i^{(k)} \right\} |_{R_k} \quad (3.17)$$

Considering the end axis of the assigned reference frames indicated in Figure 3.3 and the expression of the rotation matrices. The rotation matrix from R_{hex} to R_{nor} can be expressed as follows:

$$\hat{C}^{(hex,nor)} = \hat{C}^{(hex,spn)} \hat{C}^{(spn,tan)} \hat{C}^{(tan,nor)} \quad (3.18)$$

Considering assembly errors, the position and orientation of the spindle tool holder with respect to the hexapod reference frame are identified using a coordinate measurement machine (CMM). Consequently, the rotation matrix from R_{hex} to R_{spn} can be written as Eq. 3.19.

$$\hat{C}^{(hex,spn)} = \hat{C}_{CMM} \quad (3.19)$$

where \hat{C}_{CMM} is a constant rotation matrix that expresses the orientation of the spindle with respect to the hexapod moving plate.

Tool deflection can be decoupled to two successive rotations in the tangential and normal directions. Note that both of the mentioned rotations occur about

unit vectors of the spindle reference frame. γ_t is the rotation of the tool around the z-axis (u_3) of R_{spn} due to deflection in the tangential direction. So the rotation matrix from R_{spn} to R_{tan} can be written as Eq. 3.20.

$$\hat{C}^{(spn,tan)} = e^{\left(\tilde{u}_3^{(spn/spn)} \gamma_t\right)} \quad (3.20)$$

β_t is rotation about the y-axis (u_2) of R_{spn} due to deflection in the normal direction. So the rotation matrix from R_{tan} to R_{nor} can be written as Eq. 3.21.

$$\hat{C}^{(tan,nor)} = e^{\left(\tilde{u}_2^{(spn/tan)} \beta_t\right)} \quad (3.21)$$

Eq. 3.21 should be expressed in the spindle reference frame as follows:

$$e^{\left(\tilde{u}_2^{(spn/tan)} \beta_t\right)} = \hat{C}^{(tan,spn)} e^{\left(\tilde{u}_2^{(spn/tan)} \beta_t\right)} \hat{C}^{(spn,tan)} \quad (3.22)$$

Considering Eq. 3.23 as:

$$\hat{C}^{(tan,spn)} = e^{-\left(\tilde{u}_3^{(spn/spn)} \gamma_t\right)} \quad (3.23)$$

So Eq. 3.22 will change to Eq. 3.24.

$$e^{\left(\tilde{u}_2^{(spn/tan)} \beta_t\right)} = e^{-\left(\tilde{u}_3^{(spn/spn)} \gamma_t\right)} e^{\left(\tilde{u}_2^{(spn/spn)} \beta_t\right)} e^{\left(\tilde{u}_3^{(spn/spn)} \gamma_t\right)} \quad (3.24)$$

Tool deflections in both the tangential and normal directions are expressed in the spindle reference frame. Consequently, substituting Eqs. 3.19, 3.20 and 3.24 into the Eq. 3.18 rotation matrix from hexapod to tool tip ($\hat{C}^{(hex,nor)}$) can be obtained as follows: Simplifying $\tilde{u}_i^{(spn/spn)}$ as \tilde{u}_i , consequently:

$$\hat{C}^{(hex,nor)} = \hat{C}_{CMM} e^{(\tilde{u}_3 \gamma_t)} e^{-(\tilde{u}_3 \gamma_t)} e^{(\tilde{u}_2 \beta_t)} e^{(\tilde{u}_3 \gamma_t)} \quad (3.25)$$

given

$$e^{(\tilde{u}_3 \ \gamma_t)} e^{-(\tilde{u}_3 \ \gamma_t)} = \hat{I} \quad (3.26)$$

$$\hat{C}^{(hex,nor)} = \hat{C}_{CMM} e^{(\tilde{u}_2 \ \beta_t)} e^{(\tilde{u}_3 \ \gamma_t)} \quad (3.27)$$

Let t_{spn}^{hex} be the translation from the hexapod reference frame to the spindle reference frame obtained by CMM.

$$t_{spn}^{hex} = \begin{bmatrix} r_x \\ r_y \\ r_z \end{bmatrix} \quad (3.28)$$

Considering the assigned reference frames and tool deflection, the translation from the hexapod reference frame to the tool tip can be written as Eq. 3.29. Based on the feeding direction, δ_t can be a positive or negative value. Here, δ_n is always a negative value because the normal grinding force and Z-axis are in opposite directions.

$$t_{nor}^{spn} = \begin{bmatrix} -L \cos \gamma_t \cos \beta_t \\ \delta_t \\ \delta_n \end{bmatrix} \quad (3.29)$$

Consequently, the translation matrix and transformation homogenous matrix from R_{hex} to R_{nor} are as follows:

$$t_{nor}^{hex} = \begin{bmatrix} r_x - L \cos \gamma_t \cos \beta_t \\ r_y + \delta_t \\ r_z + \delta_n \end{bmatrix} \quad (3.30)$$

$$T_{nor}^{hex} = \begin{bmatrix} \hat{C}^{(hex,nor)} & t_{nor}^{hex} \\ 0 & 0 & 0 & 1 \end{bmatrix} \quad (3.31)$$

In order to obtain the forward kinematics of the robotic grinding setup, the transformation homogenous matrix should be written in the base reference frame. This means the rotation and translation of the hexapod moving plate with respect to the base frame should be considered. Considering the transformation homogenous matrix from R_{base} to R_{hex} as T_{hex}^{base} :

$$T_{hex}^{base} = \begin{bmatrix} \hat{C}_{hex} & t_{hex}^{base} \\ 0 & 0 & 0 & 1 \end{bmatrix} \quad (3.32)$$

where \hat{C}_{hex} and t_{hex}^{base} are the orientation and translation matrices of the hexapod moving plate and can be controlled in real-time. The forward kinematics of the robotic grinding setup can be defined as T_{FK} and obtained by multiplication of T_{hex}^{base} to T_{nor}^{hex} .

$$T_{FK} = T_{hex}^{base} T_{nor}^{hex} \quad (3.33)$$

The transformation homogenous matrix for hexapod that maintains the desired position and orientation of the tool tip can be defined as ($T_{new-hex}^{base}$). The desired forward kinematics of the setup is $T_{FK-desired}$. Therefore;

$$T_{new-hex}^{base} T_{nor}^{hex} = T_{FK-desired} \quad (3.34)$$

Finally, multiplying the desired forward kinematics with the inverse of T_{nor}^{hex} , a new position and orientation of the hexapod are obtained that compensate for the geometrical errors due to tool deflection.

$$T_{new-hex}^{base} = T_{FK-desired} T_{nor}^{hex^{-1}} \quad (3.35)$$

In this study, the desired orientation for the tool is to maintain the vertical direction. Therefore, all of the calculations during operation are made with this goal. In our setup, the calculated new rotation matrix for the hexapod should be changed to the Euler angles 1-2-3 sequence format to use as the input to the robot. In the next section, the resultant force control strategy is explained, which is implemented in parallel with the TDC approach.

3.7 Constant resultant force control using model supervised fuzzy controller

In the previous section, the effect of tool deflection is investigated and a kinematic solution is proposed. The normal and tangential grinding forces measured by the sensor were shown not to be the grinding forces of the tool reference frame because of the mentioned orientations related to the tool deflection. Therefore, controlling the force in the normal direction of the force sensor reference frame is not a proper approach. This is the reason that the resultant of the grinding force components (normal and tangential forces measured by the sensor) is controlled instead of the normal force.

The robotic grinding operation has a highly nonlinear nature as shown in the previous section. Therefore, designing a control architecture need to be able to maintain a constant resultant grinding force is challenging. The conventional linear fixed-gain PID controllers can be optimized easily for desired control specifications such as overshoot, rise time, settling time, etc. Due to the nonlinearity of the grinding process, application of a PID controller with constant gains is not a proper approach and the gains should be modified continuously while handling different inputs and operating conditions. Even if the PID controller is optimized and used for certain conditions, implementation of the controller on a physical setup is challenging. In the physical setup, there are three input sources that should be considered. The first source is the parallel hexapod by which the grinding path and feed rate are controlled. The second source is the piezo actuator by which the depth of cut is controlled. The third source is the

force sensor that supplies the force feedback. All of them have different response times. The controller should be able to synchronize the model and physical setup and control the setup force response in such a way that it converges to the model output that acts as the reference input.

In this study, a model supervised fuzzy control architecture was designed. For the user-defined set depth of cut (SDOC), spindle speed, feed rate and average spindle percent load, the model gives the proper reference resultant grinding force. The aim of the model supervised controller is to make the physical setup interaction resultant force converge with the reference value provided by the model. The depth of cut and its rate of change are the controlled parameters that are output by the fuzzy controller. During the operation together with the resultant force controller, the TDC algorithm is also used.

3.7.1 Grinding force model

The resultant force in grinding operation is the sum squared root of the normal and tangential forces, which is to be controlled. In order to design and optimize a controller, a grinding force model is defined. In robotic grinding, due to the effect of tool deflection and setup stiffness, the grinding model should be able to predict the forces in the different regimes mentioned in Chapter 2. In Chapter 2, an optimized force model for robotic grinding is proposed. In this model, using penetration tests and extracting the defined features, the mechanical properties of the setup and workpiece are included in the model indirectly. Also in this model, the percent load of the spindle, which is a function of spindle current, is included as an extra predictor in the model. The mentioned model is used in this study as a reference (required force components) input generator.

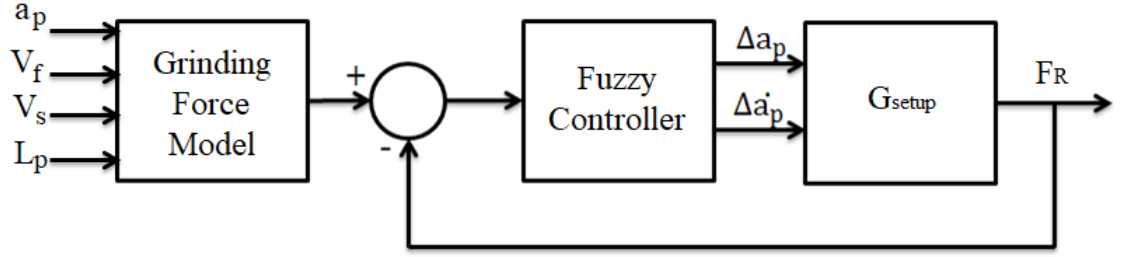


Figure 3.4: Architecture of the proposed model supervised fuzzy admittance controller

3.7.2 Fuzzy controller design

In order to obtain desired cutting depth (SDOC) a resultant grinding force control strategy is used. The reference value for resultant grinding force is generated by the grinding force model where the inputs of the force model are desired depth of cut (SDOC), spindle speed, feed rate and average spindle percent load. The output of the model is proper reference resultant grinding force. The physical setup resultant force is controlled by the fuzzy controller in order to track the reference force generated by the grinding force model. The input of the controller is the error between the reference force profile and resultant grinding force feedback measured by the sensor. During tool and workpiece interaction, to prevent any impulsive behaviors followed by unwanted overshoots and force fluctuations and probable tool and workpiece defects, both cutting depth and its rate of change should be controlled simultaneously. So, the outputs of the fuzzy controller are the necessary change in depth of cut (Δa_p) and its rate of change ($\Delta \dot{a}_p$). The mentioned fuzzy controller outputs are input to the piezo actuator. The architecture of the proposed admittance control structure is shown in Figure 3.4.

In this study, nine Gaussian membership functions were designed for error, (Δa_p) and ($\Delta \dot{a}_p$) as shown in Figure 3.5, Figure 3.6 and Figure 3.7 respectively.

The rule bases of the fuzzy controller are given in Table 3.1. The results and

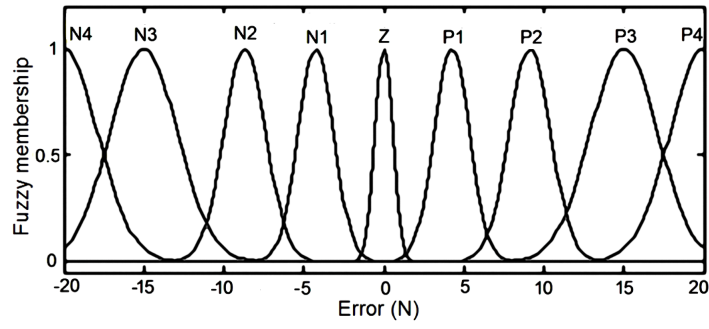


Figure 3.5: Membership functions of Error

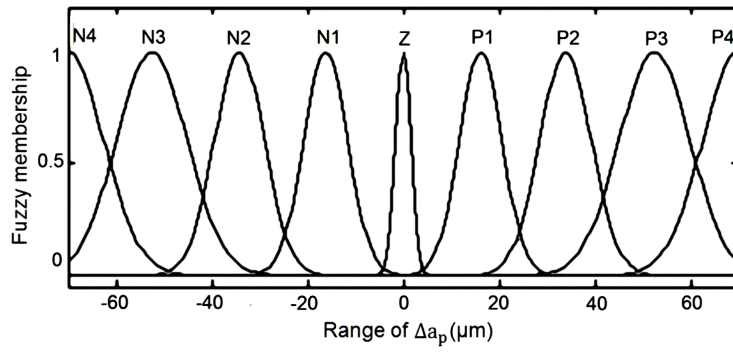


Figure 3.6: Membership functions of (Δa_p)

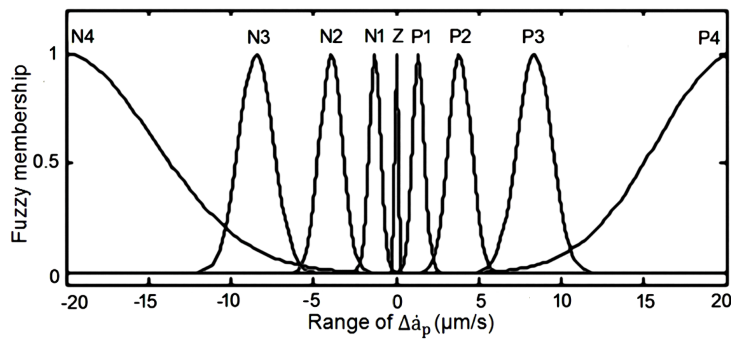


Figure 3.7: Membership functions of $(\Delta \dot{a}_p)$

Table 3.1: Rule bases of the fuzzy controller

No	Rule bases
1	If (<i>Error is N4</i>) then (Δa_p is <i>N4</i>) and ($\Delta \dot{a}_p$ is <i>N4</i>)
2	If (<i>Error is N3</i>) then (Δa_p is <i>N3</i>) and ($\Delta \dot{a}_p$ is <i>N3</i>)
3	If (<i>Error is N2</i>) then (Δa_p is <i>N2</i>) and ($\Delta \dot{a}_p$ is <i>N2</i>)
4	If (<i>Error is N1</i>) then (Δa_p is <i>N1</i>) and ($\Delta \dot{a}_p$ is <i>N1</i>)
5	If (<i>Error is Z</i>) then (Δa_p is <i>Z</i>) and ($\Delta \dot{a}_p$ is <i>Z</i>)
6	If (<i>Error is P1</i>) then (Δa_p is <i>P1</i>) and ($\Delta \dot{a}_p$ is <i>P1</i>)
7	If (<i>Error is P2</i>) then (Δa_p is <i>P2</i>) and ($\Delta \dot{a}_p$ is <i>P2</i>)
8	If (<i>Error is P3</i>) then (Δa_p is <i>P3</i>) and ($\Delta \dot{a}_p$ is <i>P3</i>)
9	If (<i>Error is P4</i>) then (Δa_p is <i>P4</i>) and ($\Delta \dot{a}_p$ is <i>P4</i>)

advantages of the proposed control strategy are presented in the next section.

3.8 Results and discussion

The general form of the proposed resultant grinding force control strategy is shown in the previous section. An example of the grinding resultant force profile without using a force controller and without implementing the TDC algorithm is shown in Figure 3.8. A flat-shaped workpiece was used for this experiment.

As the normal, tangential and resultant grinding forces increase almost linearly, this experiment belongs to the second grinding regime. Such a force increase is due to the tool deflection and low stiffness of the robotic grinding setup. The profile of the workpiece surface is measured by a Keyence-LK-HO27 laser distance sensor, shown in Figure 3.9.

Due to the applied resultant force (Figure 3.8) the profile produced on the surface is shown in Figure 3.10 together with original surface profile of the workpiece..

As shown in Figure 3.10, the grinded surface profile shows the expected depth

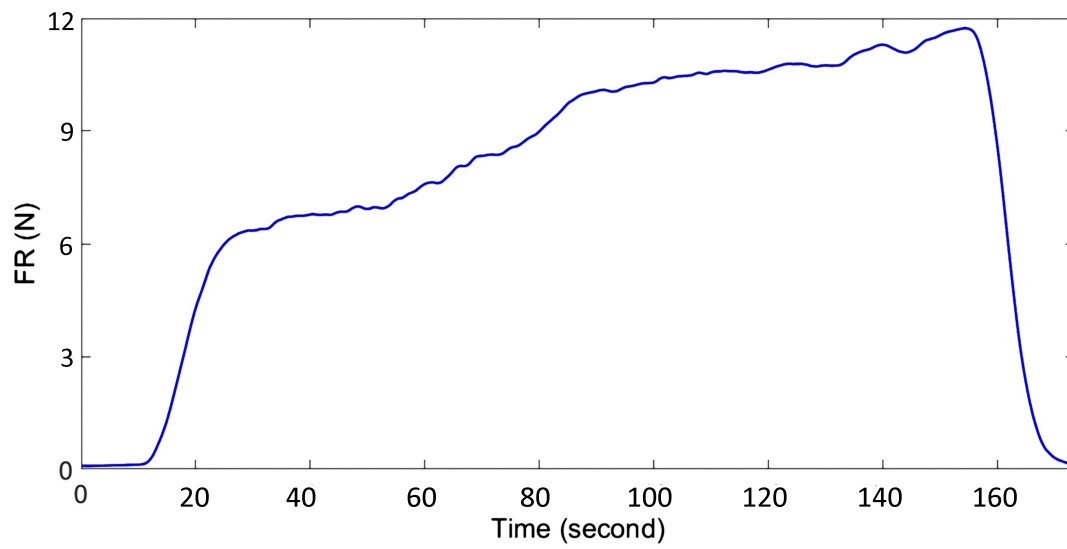


Figure 3.8: Grinding resultant force profile without using a force controller

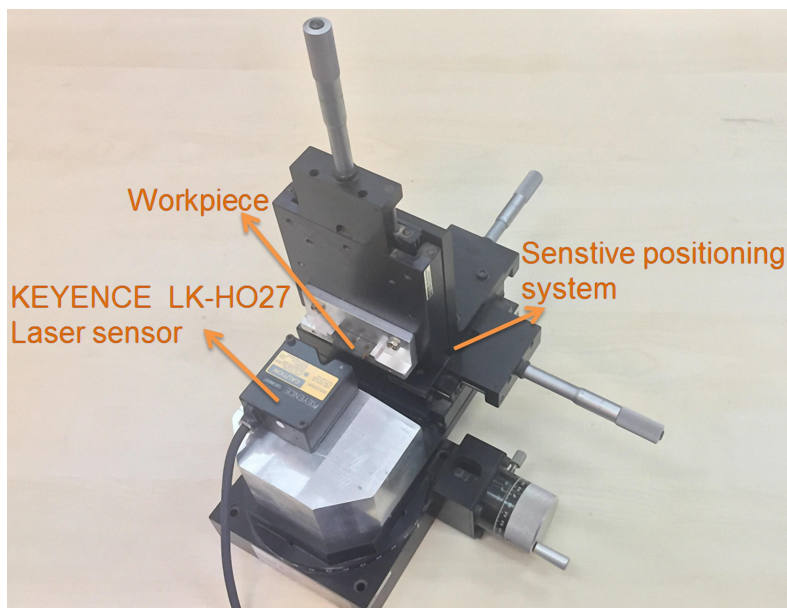


Figure 3.9: Measurement setup

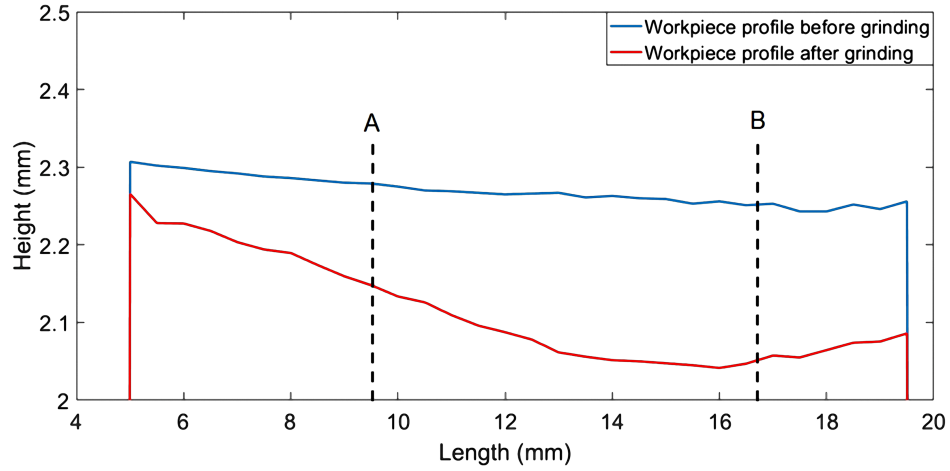


Figure 3.10: Surface profile of the workpiece before grinding and after grinding operation without any force control

of cut increase along with the resultant force rise. It shows that the material removal rate is changing along the workpiece. Therefore, it is not possible to obtain desired cutting depth (SDOC) and desired constant material removal rate during the surface grinding operation which cause geometrical errors. The increase in the resultant force is due to tool deflection. Such a deflection adds an extra component to the grinding force continuously, and this component can be considered as a spring force.

Without implementing the TDC algorithm, a significant error occurs in the cross-section of the workpiece. As shown in Figure 3.11, an inclined cross-section is obtained because of the tool deflection. Such an inclination makes it difficult to control SDOC.

Applying the proposed control approach on the robotic grinding operation and trying to maintain a constant grinding resultant force led to the force graph shown in Figure 3.12. In this graph, the force controller tries to maintain a resultant force of 9 N based on the grinding model output. In this experiment spindle speed is 30000 rpm , SDOC is $230\text{ }\mu\text{m}$, feed rate is 0.1 mm/s and percent load is 36% . The percent load value is selected based on maximum value of percent load in penetration test that is explained in Chapter 2.

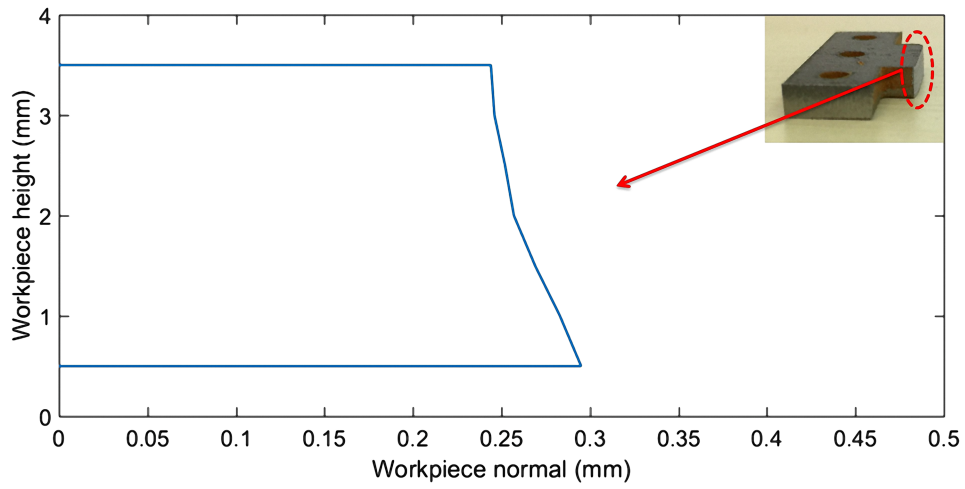


Figure 3.11: Inclined cross-section because of tool deflection

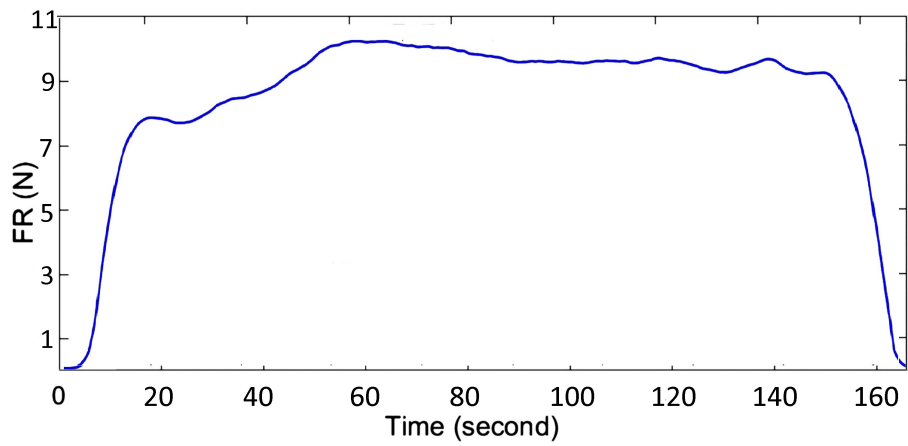


Figure 3.12: Grinding resultant force profile using the proposed force control approach

The measured surface profile of the workpiece after the grinding operation with resultant force control is shown in Figure 3.13 together with Figure 3.11. The graph indicates a noticeable effect of the resultant force control on grinding accuracy. It is shown that the cutting depth remains constant after settling of the resultant grinding force.

In this research, in order to express the effect of the resultant grinding force on the workpiece profile, the force change is shown from tool and workpiece contact instant until tool exit, in parallel with the resulting workpiece profile. The measured surface profile of the workpiece after the grinding operation with resultant force control is shown in Fig. 3.13 together with the original workpiece surface profile before grinding operation. As shown in Fig. 3.13, by entering the tool to the workpiece, the cutting depth is increased. When the grinding force reaches to the reference resultant grinding force value, the controller keeps the resultant grinding force at the range of reference grinding force value. In this condition (point A to point B on the workpiece), the cutting depth remains almost constant until the tool begins to exit from workpiece. In both Fig. 3.10 and Fig. 3.13, there are increases in the last parts of the workpieces' machined surfaces which means decrease in material removal rate. This increase starts when the tool begins to exit the workpiece. Consequently the cutting force and the cutting depth decrease and this changes cause ascending in the workpiece profile graph. In this experiment, when the tool is completely in contact with the workpiece and without considering effect of tool entrance and tool exit (point A to point B on the workpiece), the average cutting depth is equal to $209 \mu m$ where the SDOC is equal to the $230 \mu m$. Using the controller, the average error between actual and target cutting depth is equal to $21 \mu m$. The maximum variation on the workpiece profile in this condition is equal to $30 \mu m$. It means that using the resultant force control method, the cutting depth and surface quality remain constant with acceptable accuracy. Without using the proposed controller, the cutting force and consequently cutting depth increase until the tool starts to exit from the workpiece. The maximum variation on the workpiece profile in this condition is equal to $106 \mu m$ and the average cutting depth is equal to 185.5

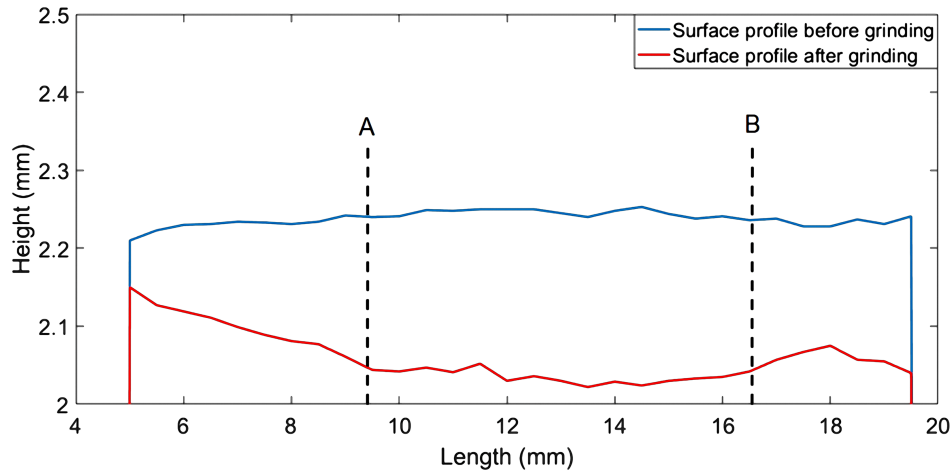


Figure 3.13: Surface profile of the workpiece before and after grinding operation using the proposed force control approach

μm . It means that without using any controller, the cutting depth and surface quality vary along the workpiece where the average error between actual and target cutting depth is equal to $44.5 \mu m$. The target grinding accuracy in this study is $30 \mu m$ for the range of $200-250 \mu m$ cutting depth in one cut machining. The achieved average accuracy was $21 \mu m$. Note that the tool entrance and exit parts are not considered. It is important to note that without implementing TDC, due to the inclination of workpiece cross section, the above values are not meaningful for cutting depth values and operation accuracy.

The effect of TDC is shown in Figure 3.14 implementing the tool deflection compensation algorithm, a vertical cross-section is obtained.

The motions of the hexapod in the X, Y and Z directions while implementing the deflection compensation algorithm are shown in Figure 3.15. Also, the hexapod rotations around the X, Y and Z axes during operation are shown in Figure 3.16. The motion in the Y-direction decreases linearly because the feeding during operation is in the Y-direction. The other motions and orientations are due to the outputs of the compensation algorithm.

One of the challenges of using fuzzy controllers is their stability check difficulty

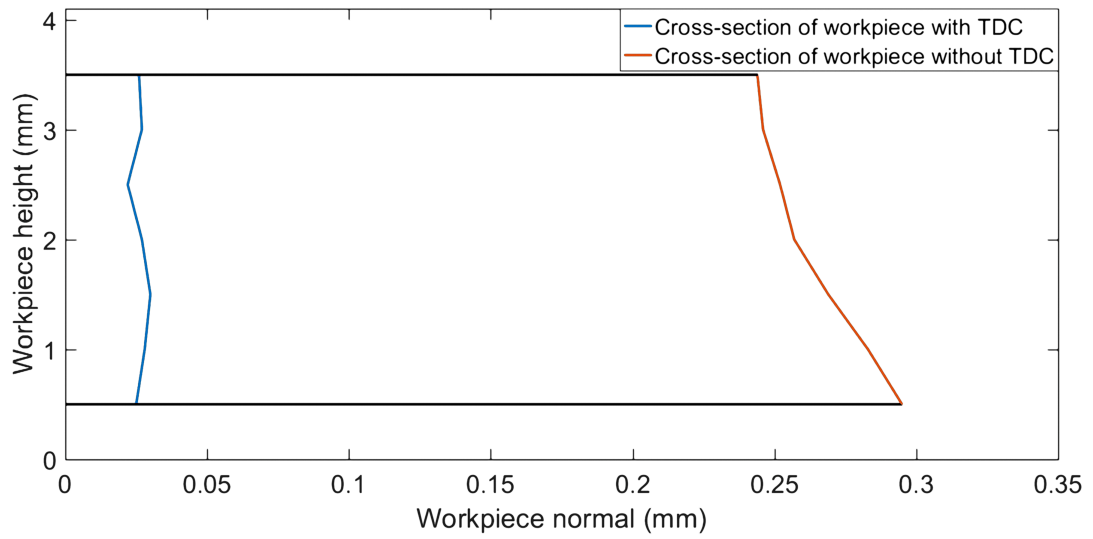


Figure 3.14: Effect of the TDC algorithm on the workpiece cross-section

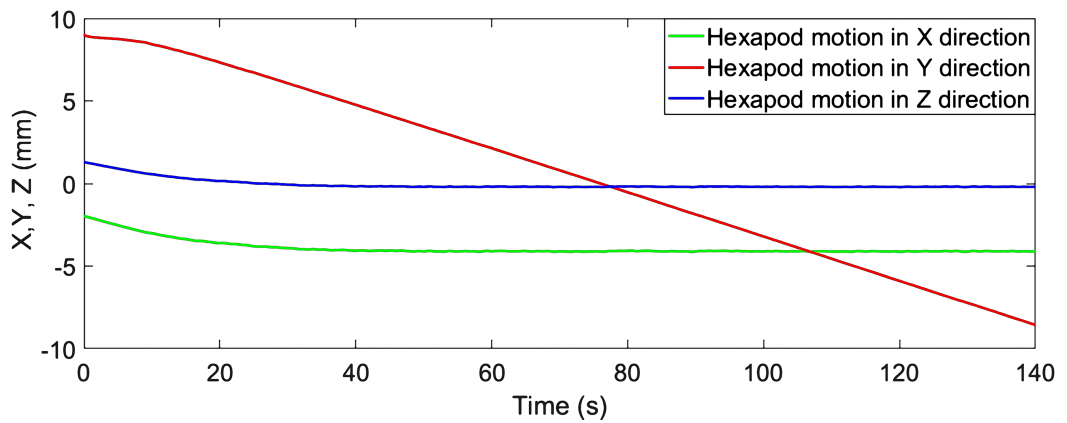


Figure 3.15: Hexapod motion in the X, Y and Z directions during the robotic grinding experiment

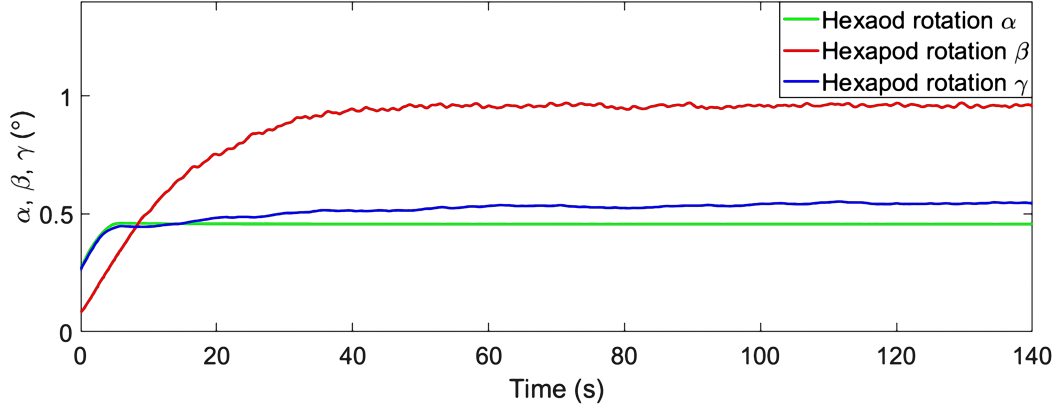


Figure 3.16: Hexapod rotation around the X,Y and Z axes during the robotic grinding experiment

in different conditions. If a constant improper reference input is used, it is possible to encounter instabilities. However, the fuzzy approach is useful for controlling cutting depth and its rate of change simultaneously, but tuning this type of controller without using a model is problematic. The first advantage of the proposed control architecture is that due to its model supervised nature, the reference force profile that should be tracked by the physical setup is realistic. This means that an improper reference force is guaranteed not to be given to the physical setup. Consequently, the unwanted grinding force overshoots and fluctuations followed by probable instabilities and tool or workpiece defects are prevented. Furthermore, application of the grinding model and the model-supervised controller facilitates the pre-simulation of the operation and tuning of the controller based on the desired controller characteristics.

CHAPTER 4

KINEMATIC/DYNAMIC ANALYSIS AND POSTURE OPTIMIZATION OF A 12 DOF HYBRID REDUNDANT MANIPULATOR

4.1 Introduction

Serial and parallel manipulators have their own advantages and disadvantages. The large workspace and flexibility of serial manipulators are very useful but extended structures of them have a tendency to vibrate working at high speeds and to deflect dealing with high loads. Also because of the serial configuration, errors of each link are added up and the overall error reflects to the end effector. Parallel manipulators they are more robust dealing with high loads and they are appropriate for precise positioning. But small work space is the important limitation of the parallel manipulators. Hybrid manipulators are suitable choices in order to use advantages of serial and parallel manipulator simultaneously. Combination of large workspace of serial manipulators and high work load and accuracy of parallel manipulators makes the hybrid manipulators as suitable choice in many operations like grinding and deburring. In this chapter a 12 DOF hybrid manipulator is investigated that is composed of a 6 DOF serial ABB IRB2000 robot and a 6 DOF PI H-824 Hexapod. The Parallel hexapod is connected to the end of the serial ABB manipulator (Figure 4.1). Complete kinematic and dynamic analysis of the hybrid manipulator is done and all reaction/actuating forces and torques are calculated. A novel strategy for posture optimization of the redundant hybrid manipulator based on minimization of

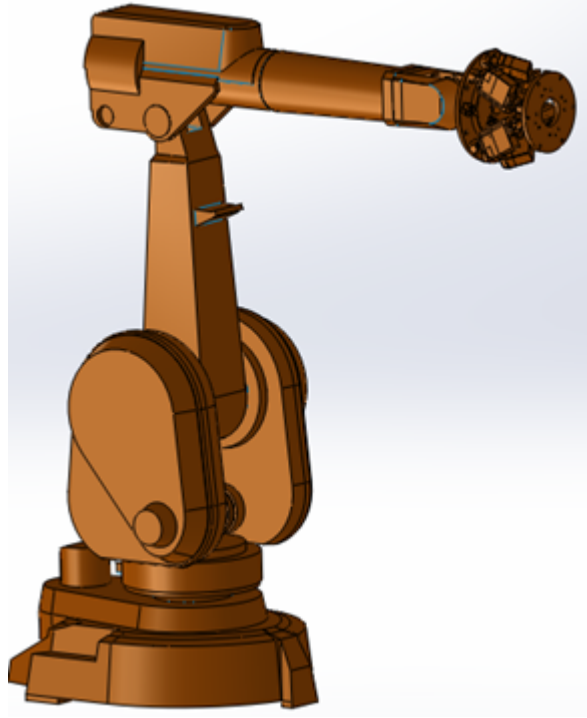


Figure 4.1: 12 DOF redundant hybrid manipulator

the computed torque of wrist joint of serial part of the hybrid manipulator is proposed in this chapter.

4.2 Literature survey

The idea of using hybrid serial-parallel manipulator for grinding and deburring operation was proposed in [54] first. Hybrid manipulators are known by combination of the serial and parallel manipulators or combination of two serial manipulators such that moving platform of the ones is fixed base of the others like a parallel manipulator chain. An example of hybrid architecture using two serial manipulators with 3 DOF in chain form is presented in [104] and [82]. Such a combination gives over all 6 DOF with respect to the fixed base frame. Another example of hybrid structure based on serial-parallel combination is shown in [15] where a 2 DOF serial manipulator is mounted to the moving

platform of a 3 DOF parallel manipulator. A discussion on kinematics and dynamics analysis of hybrid manipulators produced by attaching multiple 3 DOF serial manipulators was done in [67] and [39]. It is necessary to do kinematics and dynamics analysis for each hybrid structure separately because each new configuration has its own kinematics and control scheme. Redundancy of a manipulator is characterized as more degree of freedom than is necessary to do a specified task. Such a property enables the manipulator to access any point in the workspace with infinite postures. The related infinite inverse kinematic solutions are of interest in many robotic studies [8]. Choosing the proper inverse kinematic solution and optimal posture of the manipulator is a challenging point that has a potential to improve the performance of the redundant device. The optimization criteria should be selected in proper way based on objectives such as singularity or obstacle avoidance, power consumption minimization, stability and stiffness maximization, etc. [8]. There are large numbers of researches that propose numerical methods in order to use the redundancy in desired way. A comprehensive investigation of different criteria of using redundant manipulators like dynamics, singularity, task augmentation robustness and optimization are explained in [8]. The joint variables minimization factor is used in [9] in parallel with investigation of the joint limitations. The Ref. [45] focused on motion and singularity of 7 DOF humanoid arm while working in different angles. Several approaches are proposed in [53, 19, 18, 71, 20] in order to prevent singularity of the redundant manipulator. Increasing obstacle avoidance capability of the redundant manipulator considering the joint limitations is the area of interest in [84, 77, 68, 2, 72]. Efficient motion planning using redundancy is investigated in [97, 79]. Fault tolerance characteristics of redundant robots were shown in [40]. Actuating forces/torques minimization using redundancy is investigated in dynamic and static conditions in [42, 29, 78, 10]. Also artificial intelligence concepts (ANN, GA) are used while investigating redundant manipulators in [50, 25, 69]. There are few researches that focused on analytical solutions while investigating the redundant manipulators. The joint variables are calculated as a function of arm angle on humanoid manipulator in [85] in order to optimize

the arm angle while using joint variable minimization and joint limitations as path generation criteria. Also an analytical approach based on the arm angle of a humanoid manipulator with link offsets as extra complexity is proposed in [86] in order to analyze kinematic features of the manipulator in different configuration due to arm angle change. Motion characteristics of a 7 DOF exoskeletal arm were studied in [66] using same method. A semi analytic solution is used in [43] for avoiding singular configuration of the manipulator using the generalized inverse of the Jacobian matrix. Some redundancy resolution problems were solved in [1] with analytical approaches in velocity level. Manipulator tip point trajectory improvement was investigated in [30] with an analytical approach. In [75] two different performance criteria in position and velocity level are proposed in order to obtain optimal inverse kinematic solution of the redundant manipulators.

4.3 Kinematic and dynamic analysis and simulation of ABB IRB2000 manipulator

The IRB 2000 is a 6 DOF industrial serial manipulator with six revolute joints. Assigned reference frames and dimensions related to the Denavit-Hartenberg parameters are shown in Figure 4.2. A set of exponential rotation matrices are used [75] in order to express kinematic description of the manipulator. If $\hat{C}^{(i,j)}$ be considered as the j th link orientation with respect to the i th link the Eq. 4.1 can be written as follow based on D-H parameters [75].

$$\hat{C}^{(i-1,i)} = e^{\tilde{u}_3 \theta_i} e^{\tilde{u}_1 \alpha_i} \quad (4.1)$$

The Denavit-Hartenberg table of the robot is shown in the Table 4.1.

4.3.1 Forward kinematics of the ABB IRB2000 manipulator

The orientation matrices from frame 0 to 6 are:

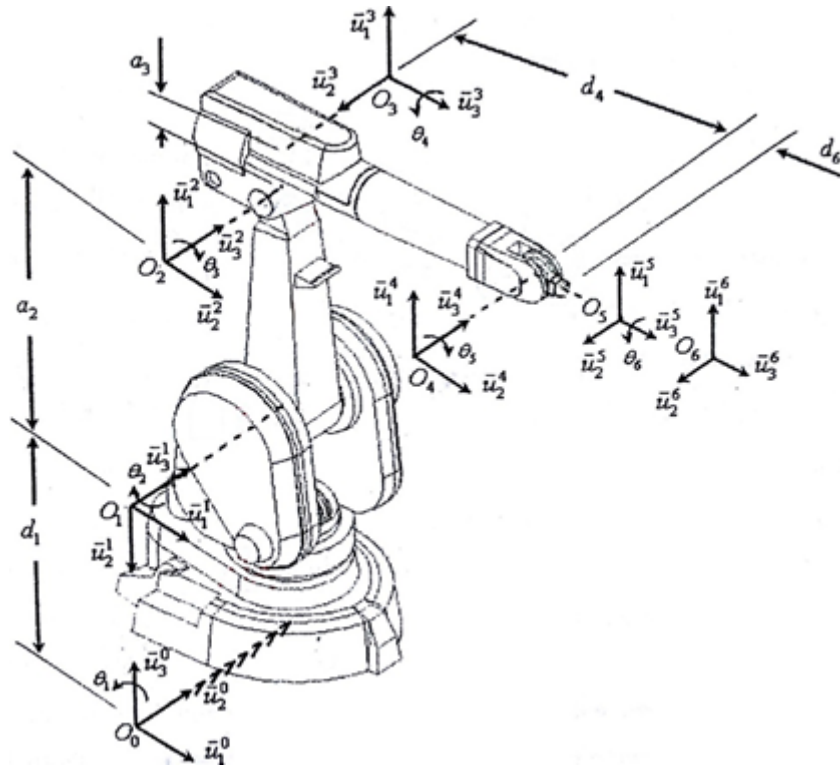


Figure 4.2: Reference frames of ABB IRB2000 Manipulator

Table 4.1: Denavit-Hartenberg parameters of ABB IRB 2000 manipulator

Link No	$a_i[mm]$	$\alpha_i[rad]$	$d_i[mm]$	$\theta_i[rad]$
1	0	$\alpha_1 = -\pi/2$	$d_1 = 750$	θ_1
2	a_2	0	0	$\theta_2 - \pi/2$
3	a_3	$\alpha_3 = -\pi/2$	0	$\theta_3 - \theta_2$
4	0	$\alpha_4 = \pi/2$	$d_4 = 850$	θ_4
5	0	$\alpha_5 = -\pi/2$	0	θ_5
6	0	0	$d_6 = 100$	θ_6

$$\hat{C}^{(0,1)} = e^{\tilde{u}_3 \theta_1} e^{-\tilde{u}_1 \frac{\pi}{2}} \quad (4.2)$$

$$\hat{C}^{(1,2)} = e^{\tilde{u}_3 \theta'_2} \text{ where } \theta'_2 = \theta_2 - \pi/2 \quad (4.3)$$

$$\hat{C}^{(2,3)} = e^{\tilde{u}_3 \theta'_3} e^{-\tilde{u}_1 \frac{\pi}{2}} \text{ where } \theta'_3 = \theta_3 - \theta_2 \quad (4.4)$$

$$\hat{C}^{(3,4)} = e^{\tilde{u}_3 \theta_4} e^{\tilde{u}_1 \frac{\pi}{2}} \quad (4.5)$$

$$\hat{C}^{(4,5)} = e^{\tilde{u}_3 \theta_5} e^{-\tilde{u}_1 \frac{\pi}{2}} \quad (4.6)$$

$$\hat{C}^{(5,6)} = e^{\tilde{u}_3 \theta_6} \quad (4.7)$$

The location of each link origin point with respect to the previous link origin point is calculated as follows:

$$\bar{r}_{01}^{(0)} = d_1 \bar{u}_3 \quad (4.8)$$

$$\bar{r}_{12}^{(1)} = a_2 e^{\tilde{u}_3 \theta'_2} \bar{u}_1 \quad (4.9)$$

$$\bar{r}_{23}^{(2)} = a_3 e^{\tilde{u}_3 \theta'_3} \bar{u}_1 \quad (4.10)$$

$$\bar{r}_{34}^{(3)} = a_3 \bar{u}_3 \quad (4.11)$$

$$\bar{r}_{45}^{(4)} = \bar{0} \quad (4.12)$$

$$\bar{r}_{56}^{(5)} = d_6 \bar{u}_3 \quad (4.13)$$

So the simplified orientation matrix can be written as follow.

$$\hat{C}^{(0,6)} = e^{\tilde{u}_3 \theta_1} e^{-\tilde{u}_1 \pi} e^{-\tilde{u}_2 (\theta'_2 + \theta'_3)} e^{\tilde{u}_3 \theta_4} e^{-\tilde{u}_2 \theta_5} e^{\tilde{u}_3 \theta_6} \quad (4.14)$$

considering

$$\theta'_{23} = \theta'_2 + \theta'_3 \quad (4.15)$$

$$\hat{C}^{(0,6)} = e^{\tilde{u}_3 \theta_1} e^{-\tilde{u}_1 \pi} e^{-\tilde{u}_2 \theta'_{23}} e^{\tilde{u}_3 \theta_4} e^{-\tilde{u}_2 \theta_5} e^{\tilde{u}_3 \theta_6} \quad (4.16)$$

So the wrist point location with respect to the base frame is

$$\begin{aligned} \bar{r} = \bar{r}_{01}^{(0)} + \hat{C}^{(0,1)} \bar{r}_{12}^{(1)} + \hat{C}^{(0,2)} \bar{r}_{23}^{(2)} + \hat{C}^{(0,3)} \bar{r}_{34}^{(3)} \\ + \hat{C}^{(0,4)} \bar{r}_{45}^{(4)} + \hat{C}^{(0,5)} \bar{r}_{56}^{(5)} \end{aligned} \quad (4.17)$$

And the position of tip point with respect to the base frame is

$$\bar{p} = \bar{r} + d_6 \hat{C}^{(0,6)} \bar{u}_3 \quad (4.18)$$

4.3.2 Inverse kinematics of the ABB IRB2000 manipulator

The inverse kinematics of the 6 DOF IRB200 robot is obtained as follows. Starting from tip point:

$$\bar{r} = \bar{p} - d_6 \hat{C}^{(0,6)} \bar{u}_3 \quad (4.19)$$

$$\bar{r}^* = \bar{r} - d_1 \bar{u}_3 \quad (4.20)$$

It is noticed that in previous equation there are three equations and three unknowns namely $\theta_1, \theta'_2, \theta'_{23}$.

since

$$\begin{aligned} \bar{r}^* = e^{\tilde{u}_3 \theta_1} [\bar{u}_1 (a_2 \cos \dot{\theta}_2 + a_3 \cos \dot{\theta}_{23} - d_4 \sin \dot{\theta}_{23}) \\ + \bar{u}_3 (-a_2 \sin \dot{\theta}_2 + a_3 \sin \dot{\theta}_{23} - d_4 \cos \dot{\theta}_{23})] \end{aligned} \quad (4.21)$$

Multiplying both side by $\bar{u}_2^t e^{-\tilde{u}_3 \theta_1}$

$$\bar{u}_2^t e^{-\tilde{u}_3 \theta_1} \bar{r}^* = 0 \text{ because } \bar{u}_2^t \bar{u}_1 = 0 \text{ and } \bar{u}_2^t \bar{u}_3 = 0 \quad (4.22)$$

so

$$r_2^* \cos(\theta_1) - r_1^* \sin(\theta_1) = 0 \quad (4.23)$$

consequently

$$\theta_1 = \text{atan2}(\sigma_1 r_2^*, \sigma_1 r_1^*) \text{ where } \sigma_1 = \pm 1 \quad (4.24)$$

premultiplying \bar{r}^* by $\bar{u}_1^t e^{-\tilde{u}_3 \theta_1}$

$$\bar{u}_1^t e^{-\tilde{u}_3 \theta_1} \bar{r}^* = a_2 \cos \theta'_2 + a_3 \cos \theta'_{23} - d_4 \sin \theta'_{23} \quad (4.25)$$

$$\bar{r}_1^* \cos(\theta_1) + \bar{r}_2^* \sin(\theta_1) = a_2 \cos \theta'_2 + a_3 \cos \theta'_{23} - d_4 \sin \theta'_{23} \quad (4.26)$$

Letting $X = r_1^* \cos(\theta_1) + r_2^* \sin(\theta_1)$

so

$$a_3 \cos \theta'_{23} - d_4 \sin \theta'_{23} = X - a_2 \cos \theta'_2 \quad (4.27)$$

Premultiplying \bar{r}^* by $\bar{u}_3^t e^{-\bar{u}_3 \theta_1}$

$$\bar{u}_3^t e^{-\bar{u}_3 \theta_1} \bar{r}^* = -a_2 \sin \theta'_2 - a_3 \sin \theta'_{23} - d_4 \cos \theta'_{23} \quad (4.28)$$

$$-a_2 \sin \theta'_2 - a_3 \sin \theta'_{23} - d_4 \cos \theta'_{23} = r_3^* = Y \quad (4.29)$$

so

$$-a_3 \sin \theta'_{23} - d_4 \cos \theta'_{23} = Y + a_2 \sin(\theta'_2) \quad (4.30)$$

Squaring and adding Eqs. (4.25) and (4.28)

$$2a_2 X \cos(\theta'_2) - 2a_2 Y \sin(\theta'_2) = X^2 + Y^2 + a_2^2 - a_3^2 - d_4^2 \quad (4.31)$$

Letting $2a_2 X = A$ and $-2a_2 Y = B$ and $X^2 + Y^2 + a_2^2 - a_3^2 - d_4^2 = D^*$

$$B \cos(\theta'_2) + A \sin(\theta'_2) = D^* \quad (4.32)$$

Using some variable change we can write

$$B \left(\frac{1-t^2}{1+t^2} \right) + A \left(\frac{2t}{1+t^2} \right) = D^* \quad (4.33)$$

$$t^2(-B - D^*) + t(2A) + (B - D^*) = 0 \quad (4.34)$$

$$\Delta = 4A^2 - [4(-B - D^*)(B - D^*)] \quad (4.35)$$

$$t_{1,2} = \frac{-2A \pm \sqrt{\Delta}}{2(-B - D^*)} \quad (4.36)$$

$$\theta'_2 = \text{atan2} \left(2t, (1 - t^2) \right) \quad (4.37)$$

$$\theta_2 = \theta'_2 + \pi/2 \quad (4.38)$$

$$\eta_3 = \frac{1}{a_3^2 + d_4^2} \left[a_3 \left(X - a_2 \cos(\theta'_2) \right) - d_4 \left(Y + a_2 \sin(\theta'_2) \right) \right] \quad (4.39)$$

$$\zeta_3 = \frac{1}{a_3^2 + d_4^2} \left[-d_4 \left(X - a_2 \cos(\theta'_2) \right) - a_3 \left(Y + a_2 \sin(\theta'_2) \right) \right] \quad (4.40)$$

$$\theta'_{23} = \text{atan2} (\zeta_3, \eta_3) \quad (4.41)$$

$$\theta_3 = \theta'_{23} + \pi/2 \quad (4.42)$$

let

$$\hat{C}^* = e^{\tilde{u}_2 \theta'_{23}} e^{\tilde{u}_1 \pi} e^{-\tilde{u}_3 \theta_1} \hat{C}^{(0,6)} = e^{\tilde{u}_3 \theta_4} e^{-\tilde{u}_2 \theta_5} e^{\tilde{u}_3 \theta_6} \quad (4.43)$$

if

$$\hat{C}^* = \begin{bmatrix} c_{11}^* & c_{12}^* & c_{13}^* \\ c_{21}^* & c_{22}^* & c_{23}^* \\ c_{31}^* & c_{32}^* & c_{33}^* \end{bmatrix} \quad (4.44)$$

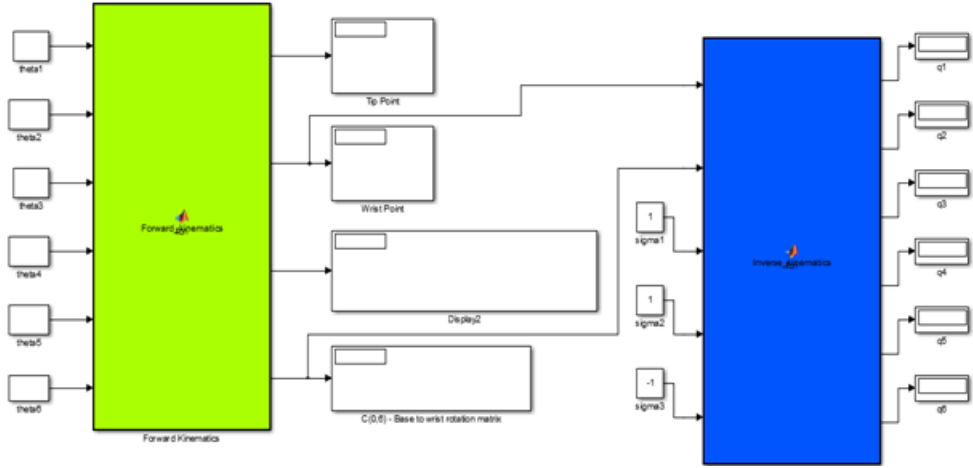


Figure 4.3: Forward and inverse kinematics blocks of the ABB manipulator

$$\theta_4 = \text{atan2}(\sigma_3 c_{23}^*, \sigma_3 c_{13}^*) \quad \text{where } \sigma_3 = \pm 1 \quad (4.45)$$

$$\theta_5 = -\text{atan2}\left(\sigma_3 \sqrt{1 - c_{33}^{*2}}, c_{33}^*\right) \quad (4.46)$$

$$\theta_6 = \text{atan2}(\sigma_3 c_{32}^*, \sigma_3 c_{32}^*) \quad \text{where } \sigma_3 = \pm 1 \quad (4.47)$$

If $\theta_5 = 0$, it is a singularity point. Then

$$\theta_6 = \text{atan2}(\sigma_3 c_{21}^*, \sigma_3 c_{11}^*) \quad \text{where } \sigma_3 = \pm 1 \quad (4.48)$$

The forward and inverse kinematics calculation in SIMULINK is shown in Figure 4.3.

Graphical simulation of the manipulator using virtual reality modeling language toolbox of MATLAB are shown in Figure 4.4 and Figure 4.5.

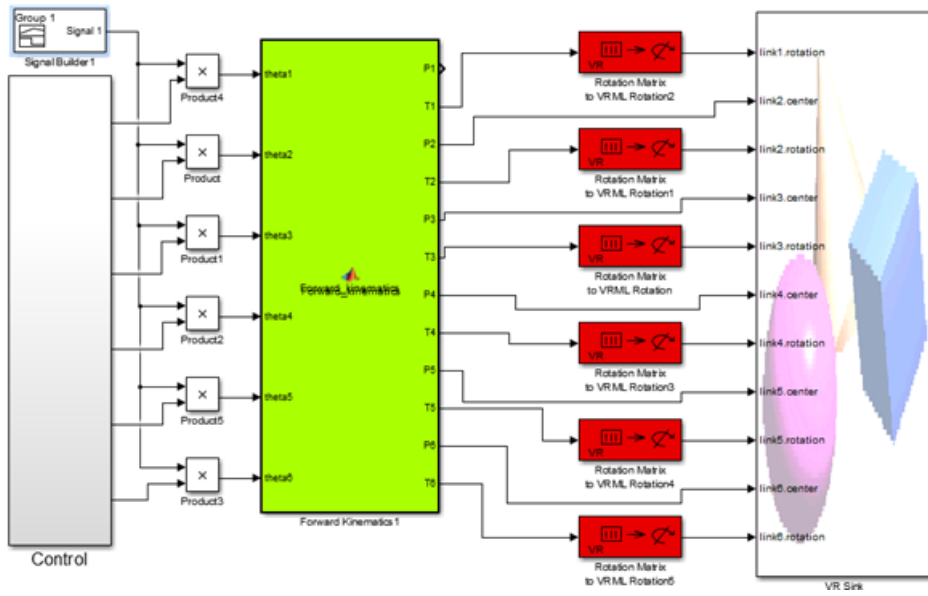


Figure 4.4: Simulation of ABB manipulator using VRML toolbox

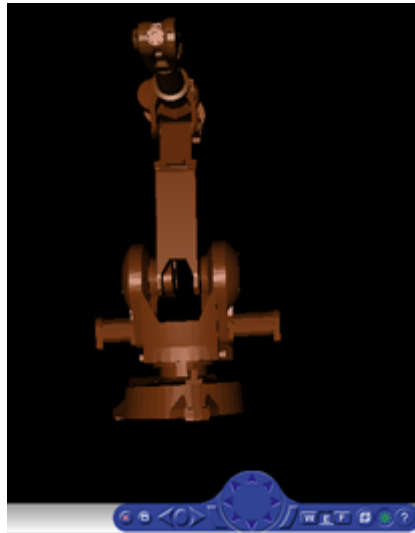


Figure 4.5: Simulation of ABB manipulator

4.3.3 Jacobian calculation of ABB IRB2000 manipulator

In IRB2000 manipulator, Jacobian matrix is generated from kinematics. Generally, Jacobian is a matrix with 6 rows and m columns. In present (ABB IRB2000) manipulator DOF is 6. That's why Jacobian matrix is in the following form.

$$\hat{J}_R = \begin{bmatrix} \bar{J}_{R_1} & \bar{J}_{R_2} & \bar{J}_{R_3} & \bar{J}_{R_4} & \bar{J}_{R_5} & \bar{J}_{R_6} \\ \bar{J}_{A_1} & \bar{J}_{A_2} & \bar{J}_{A_3} & \bar{J}_{A_4} & \bar{J}_{A_5} & \bar{J}_{A_6} \end{bmatrix}_{6 \times m} \quad (4.49)$$

where

$$\bar{J}_{R_1} = \frac{\partial \bar{p}}{\partial \theta_1} \quad (4.50)$$

$$\bar{J}_{R_2} = \frac{\partial \bar{p}}{\partial \theta_2} \quad (4.51)$$

$$\bar{J}_{R_3} = \frac{\partial \bar{p}}{\partial \theta_3} \quad (4.52)$$

$$\bar{J}_{R_4} = \frac{\partial \bar{p}}{\partial \theta_4} \quad (4.53)$$

$$\bar{J}_{R_5} = \frac{\partial \bar{p}}{\partial \theta_5} \quad (4.54)$$

$$\bar{J}_{R_6} = \frac{\partial \bar{p}}{\partial \theta_6} \quad (4.55)$$

Here \bar{p} is displacement of the tip point in inertial frame and was calculated forward kinematics analysis of the manipulator.

Also, second row of Jacobian matrix elements are as follows:

$$\bar{J}_{A_1} = \text{column} \left[\left(\frac{\partial \hat{C}}{\partial \theta_1} \right) \hat{C}^t \right] = \bar{u}_3 \quad (4.56)$$

$$\bar{J}_{A_2} = \text{column} \left[\left(\frac{\partial \hat{C}}{\partial \theta_2} \right) \hat{C}^t \right] = 0 \quad (4.57)$$

$$\bar{J}_{A_3} = \text{column} \left[\left(\frac{\partial \hat{C}}{\partial \theta_3} \right) \hat{C}^t \right] = e^{\tilde{u}_3 \theta_1} e^{-\tilde{u}_1 \pi} (-\bar{u}_2) \quad (4.58)$$

$$\bar{J}_{A_4} = \text{column} \left[\left(\frac{\partial \hat{C}}{\partial \theta_4} \right) \hat{C}^t \right] = e^{\tilde{u}_3 \theta_1} e^{-\tilde{u}_1 \pi} e^{-\tilde{u}_2 \theta_3} e^{\tilde{u}_2 \frac{\pi}{2}} (\bar{u}_3) \quad (4.59)$$

$$\bar{J}_{A_5} = \text{column} \left[\left(\frac{\partial \hat{C}}{\partial \theta_5} \right) \hat{C}^t \right] = e^{\tilde{u}_3 \theta_1} e^{-\tilde{u}_1 \pi} e^{-\tilde{u}_2 \theta_3} e^{\tilde{u}_2 \frac{\pi}{2}} e^{\tilde{u}_3 \theta_4} (-\bar{u}_2) \quad (4.60)$$

$$\bar{J}_{A_6} = \text{column} \left[\left(\frac{\partial \hat{C}}{\partial \theta_6} \right) \hat{C}^t \right] = e^{\tilde{u}_3 \theta_1} e^{-\tilde{u}_1 \pi} e^{-\tilde{u}_2 \theta_3} e^{\tilde{u}_2 \frac{\pi}{2}} e^{\tilde{u}_3 \theta_4} e^{-\tilde{u}_2 \theta_5} (\bar{u}_3) \quad (4.61)$$

Generating the Jacobian matrix, it is possible to analyze the static force/torque of the manipulator. If transpose of the Jacobian matrix is multiplied by force vector on tip point, torques of the joints can be obtained.

$$\bar{\tau} = \hat{J}^t \bar{F} \quad (4.62)$$

where

$$\bar{F}_{end\ effector}^{(0)} = \begin{bmatrix} \bar{F}^{(0)} \\ \bar{M}^{(0)} \end{bmatrix} \quad (4.63)$$

$$\bar{\tau} = \begin{bmatrix} \tau_1 \\ \tau_2 \\ \tau_3 \\ \tau_4 \\ \tau_5 \\ \tau_6 \end{bmatrix} \quad (4.64)$$

For testing the Jacobian matrix, 6 harmonic trajectory are given to the joints of the manipulator which are function of time. The mentioned trajectory are as follows.

$$\theta_1 = 0.03 + 0.3 \sin(t) \quad (4.65)$$

$$\theta_2 = 0.03 + 0.3(\cos(t) - 1) \quad (4.66)$$

$$\theta_3 = 0.03 - 0.3 \sin(t) \quad (4.67)$$

$$\theta_4 = -0.8 \sin(3t) + 10 \quad (4.68)$$

$$\theta_5 = 0.7 \cos(2t) \sin(t + 5) + 20 \quad (4.69)$$

$$\theta_6 = 2t + 12 \sin(t) \quad (4.70)$$

Figures 4.6 and 4.7 Show the trajectories of joints 1 to six together with their angular velocities and angular acceleration profiles.

Now velocity of the tip point in X, Y and Z directions are calculated using two different ways and results are compared together. First we extract the velocity of the tip point with respect to the mentioned trajectories using Jacobian matrix. Afterwards, using forward kinematics of the manipulator the trajectory of tip point in X, Y and Z directions are calculated. The numeric differentiation of these trajectories gives velocities of the tip point in X, Y and Z directions. Comparing these two velocities the Jacobian matrix can be validated.

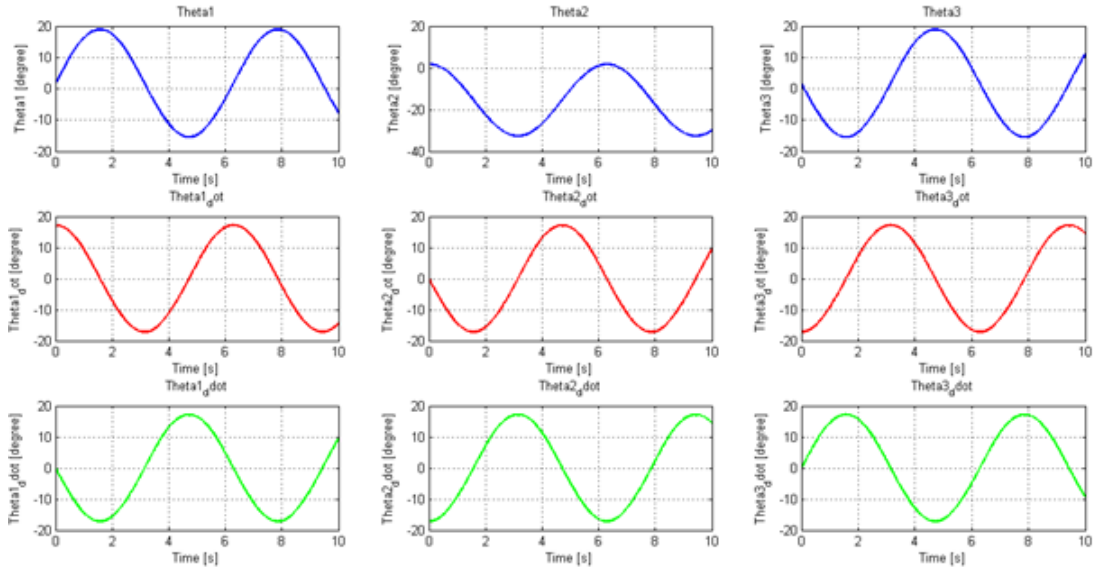


Figure 4.6: Trajectory, angular velocity and angular acceleration profiles of joints 1, 2 and 3. The blue graphs are related to the θ_1 , θ_2 and θ_3 . The red graphs are related to the $\dot{\theta}_1$, $\dot{\theta}_2$ and $\dot{\theta}_3$. The green graphs are related to the $\ddot{\theta}_1$, $\ddot{\theta}_2$ and $\ddot{\theta}_3$.

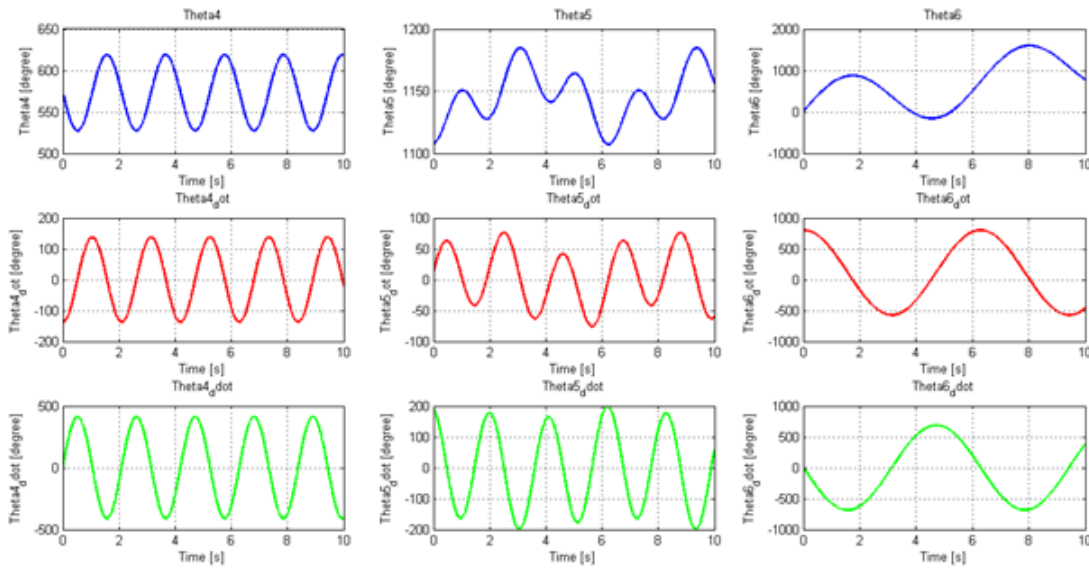


Figure 4.7: Trajectory, angular velocity and angular acceleration profiles of joints 4, 5 and 6. The blue graphs are related to the θ_4 , θ_5 and θ_6 . The red graphs are related to the $\dot{\theta}_4$, $\dot{\theta}_5$ and $\dot{\theta}_6$. The green graphs are related to the $\ddot{\theta}_4$, $\ddot{\theta}_5$ and $\ddot{\theta}_6$.

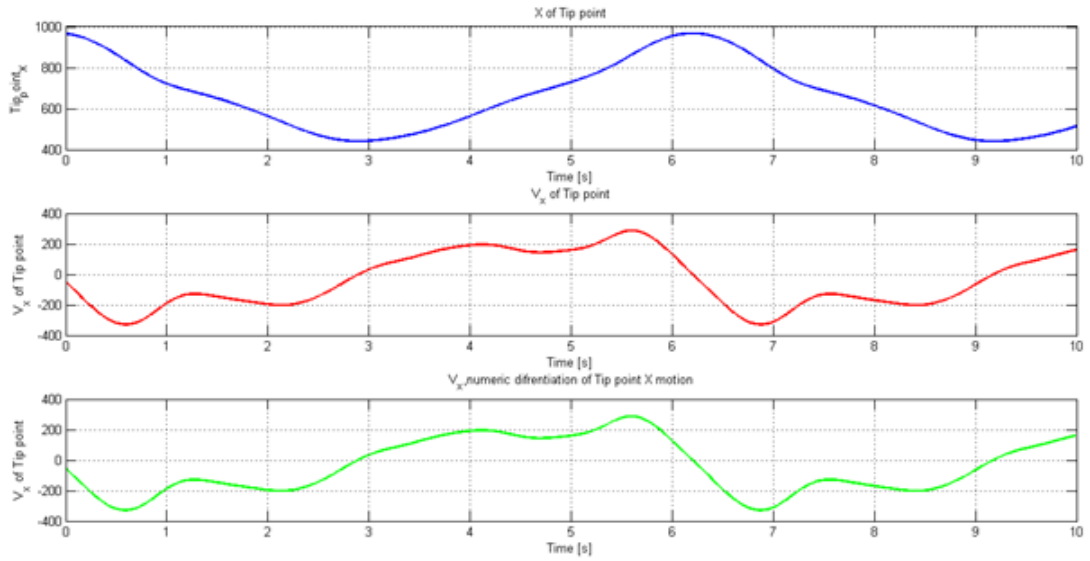


Figure 4.8: X and v_x profiles of the tip point using Jacobian matrix and numerical differentiation

Figures 4.8, 4.9 and 4.10 show the X, Y and Z profiles of the tip point together with v_x, v_y and v_z respectively. The blue graphs are related to the X, Y and Z profiles. The red graphs are related to the v_x, v_y and v_z profiles that are obtained using Jacobian matrix. The green graphs are related to the v_x, v_y and v_z profiles that are obtained using numerical differentiation of X, Y and Z profiles. The results show that the numerical method and Jacobian based method are following each other very well and it verifies the Jacobian calculation.

4.3.4 Dynamic analysis of ABB IRB2000 manipulator

During dynamic analysis of the manipulator using Newton-Euler approach, it is necessary to know the angular velocity/acceleration and linear velocity/acceleration of mass center of each body in its body fixed frame. First it is necessary to take all of the angular velocities to the i 'th body fixed frame with respect to the forward kinematics information. Then taking derivative of the $\vec{\omega}_{i/0}^{(i)}$ using the chain rule with respect to the θ_j and $\dot{\theta}_j$, it is possible to derive angular acceleration of each body $\vec{\alpha}_i^{(i)}$ in its body fixed frame.

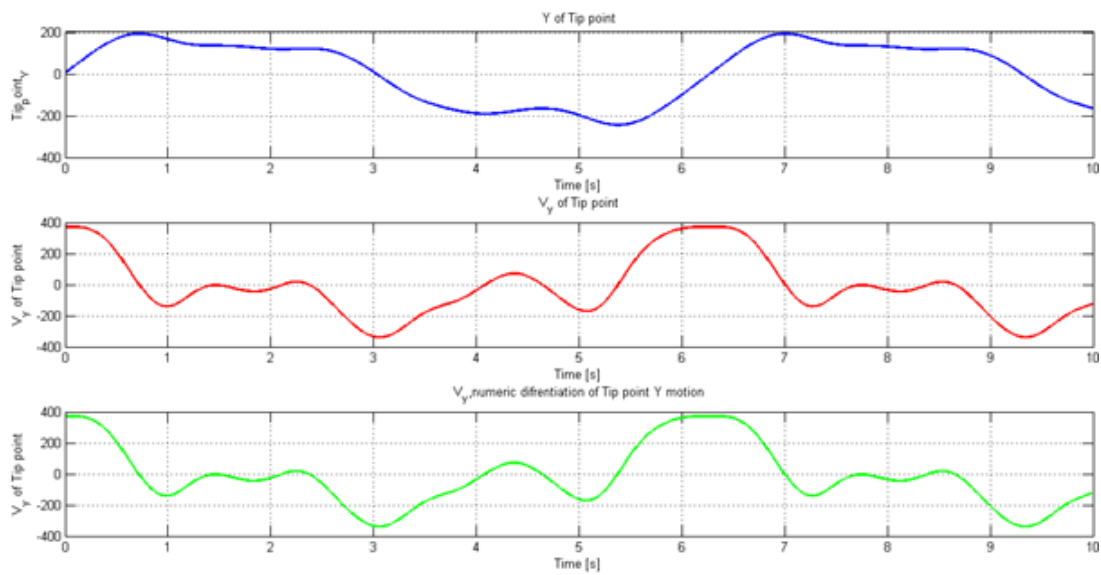


Figure 4.9: Y and v_y profiles of the tip point using Jacobian matrix and numerical differentiation

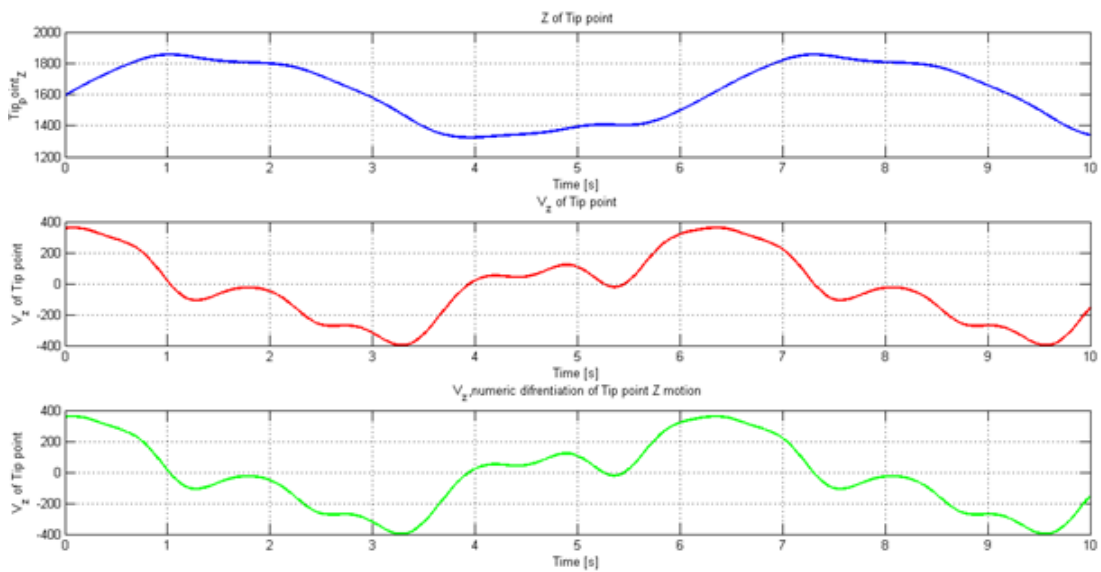


Figure 4.10: Z and v_z profiles of the tip point using Jacobian matrix and numerical differentiation

$$\vec{\omega}_{i/0}^{(i)} = f(\dot{\theta}_i, \theta_i, \dot{\theta}_{i-1}, \theta_{i-1}, \dots, \dot{\theta}_1, \theta_1) \quad (4.71)$$

$$\vec{\alpha}_i^{(i)} = \sum_{j=1}^i \left[\dot{\theta}_j \frac{\partial \vec{\omega}_i^{(i)}}{\partial \theta_j} + \ddot{\theta}_j \frac{\partial \vec{\omega}_i^{(i)}}{\partial \dot{\theta}_j} \right] \quad (4.72)$$

In order to calculate linear velocity and acceleration of center of mass we can write position vector of the mass center as follows.

$$\vec{\alpha}_i^{(i)} = \sum_{j=1}^i \left[\dot{\theta}_j \frac{\partial \vec{\omega}_i^{(i)}}{\partial \theta_j} + \ddot{\theta}_j \frac{\partial \vec{\omega}_i^{(i)}}{\partial \dot{\theta}_j} \right] \quad (4.73)$$

$$\vec{r}_{mi} = \vec{r}_i^{(0)} + x_{mi} \vec{u}_1^i + y_{mi} \vec{u}_2^i + z_{mi} \vec{u}_3^i \quad (4.74)$$

For eliminating coriolis term while taking derivative, it is possible to take all of the terms of \vec{r}_{mi} expression to the zero frame.

$$\bar{r}_{mi} = \vec{r}_i^{(0)} + x_{mi} \hat{C}^{(0,i)} \bar{u}_1^{(i)} + y_{mi} \hat{C}^{(0,i)} \bar{u}_2^{(i)} + z_{mi} \hat{C}^{(0,i)} \bar{u}_3^{(i)} \quad (4.75)$$

Then taking derivative using chain rule gives velocity of center of mass at zero frame.

$$\vec{V}_i^{(0)} = \sum_{j=1}^i \dot{\theta}_j \frac{\partial \vec{r}_i^{(0)}}{\partial \theta_j} \quad (4.76)$$

Now again using chain rule and taking derivative of the velocity vector, the acceleration of the center of mass can be calculated as follow.

$$\vec{a}_i^{(0)} = \sum_{j=1}^i \left[\dot{\theta}_j \frac{\partial \vec{V}_i^{(0)}}{\partial \theta_j} + \ddot{\theta}_j \frac{\partial \vec{V}_i^{(0)}}{\partial \dot{\theta}_j} \right] \quad (4.77)$$

Now the acceleration term is ready to be taken to the i^{th} body fixed frame.

$$\vec{a}_i^{(i)} = \hat{C}^{(i,0)} \vec{a}_i^{(0)} \quad (4.78)$$

For the first part of dynamic analysis of the hybrid manipulator direct and inverse dynamic of serial ABB manipulator will be analyzed. In dynamic investigation based on Lagrangian method, kinetic energy statement is subjected to both generalized coordinates and bodies fixed frame coordinates. In this condition, calculating partial derivations in order to obtain generalized momenta equation leads very long expressions. In order to solve this problem Newton-Euler technique is utilized for dynamic analysis of the manipulator. Furthermore, it is possible to obtain all reaction forces, moments and accelerations of generalized coordinates based on known actuating torques/forces, using Newton-Euler dynamic equations. The mentioned torques/forces are exerted from actuators to the joints of the manipulator. The ABB manipulator is composed of 6 bodies that each body is related to a link. Newton-Euler method generates 6 scalar equations in the space for each body where 3 scalar equations come from force vector and 3 scalar equations are extracted from moment vector. So 36 scalar equations should be generated while dynamic analysis of the manipulator that are mentioned in Table 4-2. In Table 4-2 the interaction force and moments between bodies together with actuating torques coming from joint motors are shown.

For i^{th} body of the serial manipulator, the Newton-Euler dynamic analysis method is described as follows. As mentioned the ABB manipulator is composed of 6 bodies that each body is related to a link. Each body is connected to the next body by a revolute joint. Based Newton-Euler approach for each body six scalar equations are derived; three scalar equations from force vector equation and other three scalar equations from moment vector equations. The general form of these equations for i^{th} body according to the forces in Table 4-2 are mentioned as follows.

$$\vec{F}_{i-1,i} + \vec{F}_{i+1,i} - m_i g \vec{u}_3^0 = m_i \vec{a}_i \quad (4.79)$$

Table 4.2: Number of unknowns in direct dynamic of ABB IRB2000 manipulator

	Joints	Bodies	Unknowns			Parameters
			\vec{F}	\vec{M}	$\ddot{\theta}$	
1	Rev.	0 & 1	3	2	-	$\vec{F}_{01} = F_{011} \vec{u}_1^1 + F_{012} \vec{u}_2^1 + F_{013} \vec{u}_3^1$ $\vec{M}_{01} = M_{011} \vec{u}_1^1 + M_{012} \vec{u}_2^1 + (T_1 - C_{01}\dot{\theta}_1) \vec{u}_3^1$
2	Rev.	1 & 2	3	2	-	$\vec{F}_{12} = F_{121} \vec{u}_1^2 + F_{122} \vec{u}_2^2 + F_{123} \vec{u}_3^2$ $\vec{M}_{12} = M_{121} \vec{u}_1^2 + M_{122} \vec{u}_2^2 + (T_2 - C_{12}\dot{\theta}_2) \vec{u}_3^2$
3	Rev.	2 & 3	3	2	-	$\vec{F}_{23} = F_{231} \vec{u}_1^3 + F_{232} \vec{u}_2^3 + F_{233} \vec{u}_3^3$ $\vec{M}_{23} = M_{231} \vec{u}_1^3 + M_{232} \vec{u}_2^3 + (T_3 - C_{23}\dot{\theta}_3) \vec{u}_3^3$
4	Rev.	3 & 4	3	2	-	$\vec{F}_{34} = F_{341} \vec{u}_1^4 + F_{342} \vec{u}_2^4 + F_{343} \vec{u}_3^4$ $\vec{M}_{34} = M_{341} \vec{u}_1^4 + M_{342} \vec{u}_2^4 + (T_4 - C_{34}\dot{\theta}_4) \vec{u}_3^4$
5	Rev.	4 & 5	3	2	-	$\vec{F}_{45} = F_{451} \vec{u}_1^5 + F_{452} \vec{u}_2^5 + F_{453} \vec{u}_3^5$ $\vec{M}_{45} = M_{451} \vec{u}_1^5 + M_{452} \vec{u}_2^5 + (T_5 - C_{45}\dot{\theta}_5) \vec{u}_3^5$
6	Rev.	5 & 6	3	2	-	$\vec{F}_{56} = F_{561} \vec{u}_1^6 + F_{562} \vec{u}_2^6 + F_{563} \vec{u}_3^6$ $\vec{M}_{56} = M_{561} \vec{u}_1^6 + M_{562} \vec{u}_2^6 + (T_6 - C_{56}\dot{\theta}_6) \vec{u}_3^6$
7	Motion	1-6	-	-	6	$\ddot{\theta}_1, \ddot{\theta}_2, \ddot{\theta}_3, \ddot{\theta}_4, \ddot{\theta}_5, \ddot{\theta}_6$
Total			18	12	6	36 Unnowns

where $\vec{F}_{i-1,i}$ is the force vector acting from $(i-1)^{\text{th}}$ body to i^{th} body and $\vec{F}_{i+1,i}$ is the force vector acting from $(i+1)^{\text{th}}$ body to i^{th} body.

$$\vec{F}_{i-1,i} = F_{(i-1,i),1} \vec{u}_1^i + F_{(i-1,i),2} \vec{u}_2^i + F_{(i-1,i),3} \vec{u}_3^i \quad (4.80)$$

$$\vec{F}_{i+1,i} = F_{(i+1,i),1} \vec{u}_1^i + F_{(i+1,i),2} \vec{u}_2^i + F_{(i+1,i),3} \vec{u}_3^i \quad (4.81)$$

The gravity term is always expressed in zero frame, but before extracting the equations we need to take all elements to the i^{th} frame.

$$\vec{r} = \vec{u}_3^0 \quad (4.82)$$

$$\vec{r}^{(i)} = \overline{\overline{u_3}}^{(0)}(\vec{r}) = \hat{C}^{(i,0)} \overline{\overline{u_3}}^{(0)}(\vec{0}) \quad (4.83)$$

The \vec{a}_i is acceleration vector of the center of gravity of the i^{th} body on body fixed frame i that is calculated in kinematic analysis of the manipulator.

$$\vec{a}_i = a_{i1} \vec{u}_1^i + a_{i2} \vec{u}_2^i + a_{i3} \vec{u}_3^i \quad (4.84)$$

Three scalar equations can be extracted from a vector equation.

Three scalar equations related to the Newton-Euler moment equation of the i^{th} body can be extracted as follow:

$$\overline{\overline{C_i A_i}} \times \vec{F}_{i-1,i} + \overline{\overline{C_i B_i}} \times \vec{F}_{i+1,i} + \overline{\overline{M_{i-1,i}}} + \overline{\overline{M_{i-1,i}}} = \check{J}_i \cdot \vec{\alpha}_i + \vec{\omega}_i \times \check{J}_i \cdot \vec{\omega}_i \quad (4.85)$$

where

C_i : gravity center of the i^{th} body

A_i : connection point of body $(i-1)^{\text{th}}$ and body i

B_i : connection point of body i and body $(i+1)^{\text{th}}$

\times : cross product

\cdot : dot product

The schematic configuration of $\overline{\overline{A_i}}$, $\overline{\overline{B_i}}$ and $\overline{\overline{C_i}}$ vectors is shown in Figure 4.11.

Here x_{mi}, y_{mi} and z_{mi} are position parameters of the i^{th} body mass center in body fixed frame. Note that in $(\overline{\overline{C_i B_i}})$ vectors we start from mass centers and go to the frame i , That's why a negative signs are appeared on the vector expressions. Also the $(\overline{\overline{B_i A_i}})$ Vectors are in negative direction of the $\vec{r}_{i-1,i}$ vectors that are mentioned in kinematic analysis section.

$$\overline{\overline{A_i C_i}} + \overline{\overline{C_i B_i}} = \overline{\overline{A_i B_i}} \quad (4.86)$$

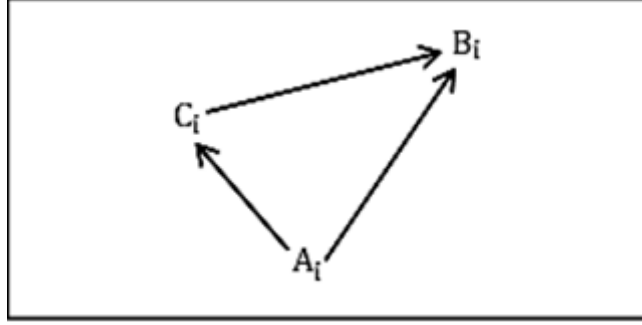


Figure 4.11: Schematic configuration of connections and center of gravity vectors of a body

$$\overrightarrow{C_i B_i} + \overrightarrow{B_i A_i} = \overrightarrow{C_i A_i} \quad (4.87)$$

$$\overrightarrow{C_i B_i} = -x_{mi} \vec{u}_1^i - y_{mi} \vec{u}_2^i - z_{mi} \vec{u}_3^i \quad (4.88)$$

$$\overrightarrow{B_i A_i} = -\vec{r}_{i-1,i} \quad (4.89)$$

$$\overrightarrow{C_i A_i} = -x_{mi} \vec{u}_1^i - y_{mi} \vec{u}_2^i - z_{mi} \vec{u}_3^i - \vec{r}_{i-1,i} \quad (4.90)$$

An important point here is that while writing the $\overrightarrow{B_i A_i}$, the vector $\vec{r}_{i-1,i}$ must be written at i^{th} body fixed frame. For example for the body 1:

$$\vec{r}_{01}^{(0)} = d_1 \vec{u}_3 \rightarrow \vec{r}_{01}^{(1)} = -d_1 \hat{C}^{(1,0)} \vec{u}_3^{(0)} = -d_1 \vec{u}_2 \rightarrow \overrightarrow{B_1 A_1} = -d_1 \vec{u}_2 \quad (4.91)$$

In the moment equations for i^{th} body $\vec{M}_{i-1,i}$ is the moment vector acting from $(i-1)^{\text{th}}$ body to i^{th} body and $\vec{M}_{i+1,i}$ is the moment vector acting from $(i+1)^{\text{th}}$ body to i^{th} body.

$$\vec{M}_{i-1,i} = M_{(i-1,i),1} \vec{u}_1^i + M_{(i-1,i),2} \vec{u}_2^i + (T_i - C_{(i-1,i)} \dot{\theta}_i) \vec{u}_3^i \quad (4.92)$$

Where T_i is torque between $(i-1)^{\text{th}}$ body and i^{th} body around \vec{u}_3 , $C_{(i-1,i)}$ is viscous friction coefficient of the joint that is related to the relative angular velocities of the bodies.

$$\vec{M}_{i+1,i} = M_{(i+1,i),1} \vec{u}_1^i + M_{(i+1,i),2} \vec{u}_2^i + (T_{i+1} - C_{(i,i+1)} \dot{\theta}_{i+1}) \vec{u}_3^i \quad (4.93)$$

Where T_{i+1} is torque between body i and body $i+1$ around \vec{u}_3 , $C_{(i,i+1)}$ is viscous friction coefficient.

$\vec{\alpha}_i$ is angular acceleration of the i^{th} body and have 3 components around \vec{u}_1^i , \vec{u}_2^i and \vec{u}_3^i .

$$\vec{\alpha}_i = \alpha_{i1} \vec{u}_1^i + \alpha_{i2} \vec{u}_2^i + \alpha_{i3} \vec{u}_3^i \quad (4.94)$$

The term $(\vec{\omega}_i \times \check{J}_i \vec{\omega}_i)$ is a vector with three components in terms of \vec{u}_1^i , \vec{u}_2^i and \vec{u}_3^i where \check{J}_i is moment of inertia dyadic of the i^{th} body. The three scalar equations coming from moment equations can be written as follows.

Extracting 6 equations (3 from force vector/3 from moment vector) for 6 body 36 scalar equations are generated with 36 unknowns related to the reaction forces/torques and angular accelerations of the joints. Note that in all of the above equations $\vec{F}_{i+1,i} = -\vec{F}_{i,i+1}$ and $\vec{M}_{i+1,i} = -\vec{M}_{i,i+1}$ due to the reaction force/torque effect.

So the equations can be written in matrix format as follows in order to calculate direct kinematics of the manipulator.

$$[Coefficients]_{36 \times 36} \cdot \begin{bmatrix} \bar{\theta}_i \\ \bar{F}_{(i-1, i), 1} \\ \bar{F}_{(i-1, i), 2} \\ \bar{F}_{(i-1, i), 3} \\ \bar{M}_{(i-1, i), 1} \\ \bar{M}_{(i-1, i), 2} \end{bmatrix}_{36 \times 1} = [Known parameters]_{36 \times 1} \quad (4.95)$$

Substituting the $\bar{\theta}_i$ by \bar{T}_i in the unknown parameters matrix and manipulating the coefficient and known parameters matrices, it is possible to find inverse kinematics of the manipulator easily.

$$[Coefficients]_{36 \times 36} \cdot \begin{bmatrix} \bar{T}_i \\ \bar{F}_{(i-1, i), 1} \\ \bar{F}_{(i-1, i), 2} \\ \bar{F}_{(i-1, i), 3} \\ \bar{M}_{(i-1, i), 1} \\ \bar{M}_{(i-1, i), 2} \end{bmatrix}_{36 \times 1} = [Known parameters]_{36 \times 1} \quad (4.96)$$

A model and simulation of the IRB2000 manipulator is developed using MATLAB[®] Simscape toolbox (Figure 4.12).

4.4 Kinematics and dynamic analysis of the parallel hexapod

Using transformation homogenous matrix and inverse kinematics, it is possible to find the stroke lengths with known angular displacement of the platform in roll, pitch and yaw motions. This method does not give any information about angular displacement of the motor bodies that are necessary for dynamic analysis. Using any dynamic analysis approach like Newton-Euler or Lagrange-Euler, all moving bodies' angular displacements, velocities and accelerations are needed. In order to calculate mentioned parameters loop closure equation

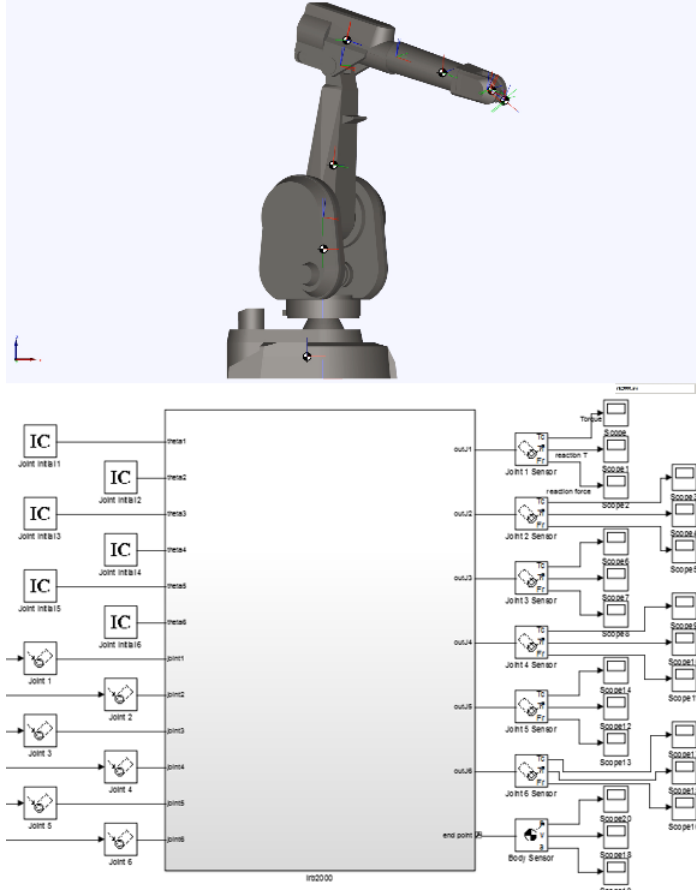


Figure 4.12: MATLAB[®] Simscape model of ABB IRB2000 manipulator

(LCE) in 3D for each motor can be written where each equation gives three scalar equations. In our hexapod each motor is connected to the base frame with a universal joint. So four reference frames are assigned and shown in Figure 4.13.

Zero frame is fixed on point O and frame P is assigned to the upper platform at point A. This frame has a translation X , Y and Z values and rotation with Euler angles sequence 1-2-3 (Roll, Pitch and Yaw) with respect to the zero frame. Due to the hexapod motors configuration there is another fixed rotation between zero frame and motor body fixed frames about $\vec{u}_3^{(0)}$. We call this constant azimuth angle as ψ_i for each motor. So the constant rotation with respect to the zero frame can be written as

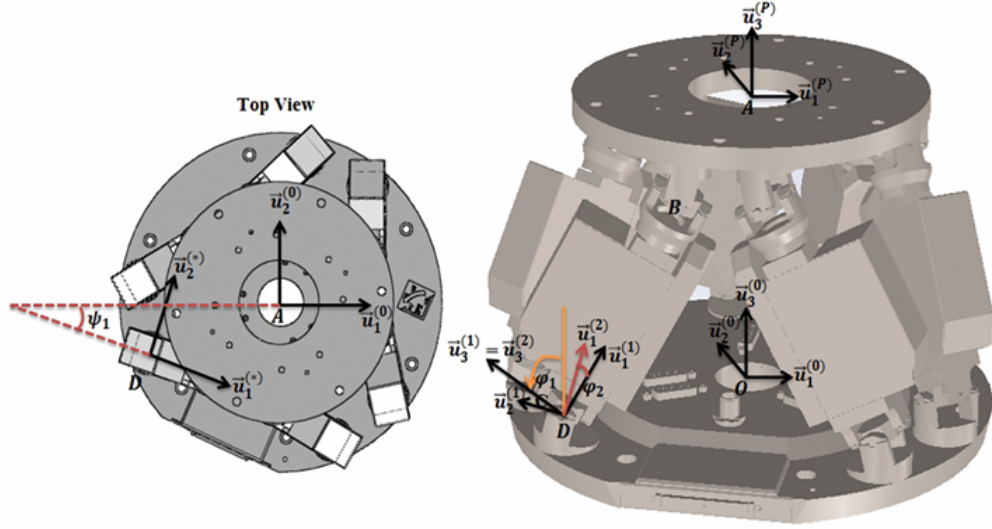


Figure 4.13: Hexapod views and assigned reference frames

$$\hat{C}^{(0,*)} = e^{\tilde{u}_3 \psi_i} \quad (4.97)$$

This rotation is shown on top view of the hexapod in Figure 4.13. It leads to a fixed dummy frame that is fixed for each motor and shown by $\vec{u}_1^{(*)}$ and $\vec{u}_2^{(*)}$ vectors in Figure 4.13. Another frame 1 is assigned on point D and has a rotation about $\vec{u}_2^{(1)} = \vec{u}_2^{(*)}$ with φ_{1i} angle. The last frame 2 is assigned on point D and has a lateral rotation about $\vec{u}_3^{(1)} = \vec{u}_3^{(2)}$ with φ_{2i} angle. As shown in Figure 4.13, the LCE equation for each motor can be written as:

$$\vec{OA} + \vec{AB} = \vec{OC} + \vec{CB} \quad (4.98)$$

Vector \vec{OC} is a known vector that indicates the location of each motor with respect to the zero frame. For i^{th} motor

$$\vec{OC} = p_{ix} \vec{u}_1^{(0)} + p_{iy} \vec{u}_2^{(0)} + p_{iz} \vec{u}_3^{(0)} \quad (4.99)$$

The \vec{CB} vector is

$$\overrightarrow{CB} = S_i \vec{u}_1^{(2)} \quad (4.100)$$

where s_i is variable parameter related to the motor shaft length. It is preferred to write all vector notations in zero frame

$$\overline{CB}^{(0)} = s_i \bar{u}_1^{(\frac{1}{0})} = s_i \hat{C}^{(0,1)} \bar{u}_1^{(\frac{1}{1})} \quad (4.101)$$

Now considering $\hat{C}^{(0,*)}$, it is possible to define $\hat{C}^{(0,2)}$ as rotation matrix that transfer frame zero to frame 2.

$$\hat{C}^{(0,2)} = e^{\tilde{u}_3 \psi_i} e^{\tilde{u}_2 \varphi_{1i}} e^{\tilde{u}_3 \varphi_{2i}} \quad (4.102)$$

Consequently

$$\overline{CB}^{(0)} = s_i e^{\tilde{u}_3 \psi_i} e^{\tilde{u}_2 \varphi_{1i}} e^{\tilde{u}_3 \varphi_{2i}} \bar{u}_1 \quad (4.103)$$

Vector \overrightarrow{CB} can be written in vector notation as

$$\begin{aligned} \overrightarrow{CB} = & \vec{u}_1^{(0)} [s_i (\cos \varphi_{1i} \cos \varphi_{2i} \cos \psi_i - \sin \varphi_{2i} \sin \psi_i)] \\ & + \vec{u}_2^{(0)} [s_i (\cos \varphi_{1i} \cos \varphi_{2i} \sin \psi_i + \sin \varphi_{2i} \cos \psi_i)] \\ & - \vec{u}_3^{(0)} [s_i \cos \varphi_{2i} \sin \varphi_{1i}] \end{aligned} \quad (4.104)$$

Left side of the equation 4-104 is known and calculated using translation X , Y and Z values and rotation with Euler angles sequence 1-2-3 (Roll, Pitch and Yaw) with respect to non-inertial frame.

$$\overrightarrow{OA} = X \vec{u}_1^{(0)} + Y \vec{u}_2^{(0)} + Z \vec{u}_3^{(0)} \quad (4.105)$$

$$\overrightarrow{AB} = r_{ix} \overrightarrow{u}_1^{(p)} + r_{iy} \overrightarrow{u}_2^{(p)} + r_{iz} \overrightarrow{u}_3^{(p)} \quad (4.106)$$

In vector \overrightarrow{AB} expression r_{ix} , r_{iy} and r_{iz} are position information of upper side of the each motor that is connected to the upper plate and these positions parameters are known due to design configuration of hexapod. It is possible to express vector \overrightarrow{AB} in zero frame.

$$\overrightarrow{AB}^{(0)} = r_{ix} \hat{C}^{(0,p)} \bar{u}_1^{\left(\frac{p}{p}\right)} + r_{iy} \hat{C}^{(0,p)} \bar{u}_2^{\left(\frac{p}{p}\right)} + r_{iz} \hat{C}^{(0,p)} \bar{u}_3^{\left(\frac{p}{p}\right)} \quad (4.107)$$

Where $\hat{C}^{(0,p)}$ is rotation matrix of the upper platform of the hexapod rotation with Euler angles sequence 1-2-3 (Roll, Pitch and Yaw). The reason that we use 1-2-3 sequence is that in this sequence the singularity is happen when pitch angle $\beta = \pi/2$ and almost it is impossible due to geometry of the platform.

$$\hat{C}^{(0,p)} = e^{\bar{u}_1 \alpha} e^{\bar{u}_2 \beta} e^{\bar{u}_3 \gamma} \quad (4.108)$$

$$\hat{C}^{(0,p)} = e^{\bar{u}_1 \alpha} e^{\bar{u}_2 \beta} e^{\bar{u}_3 \gamma} \quad (4.109)$$

so

$$\begin{aligned} \begin{bmatrix} 1 & 0 & 0 \\ 0 & \cos \alpha & -\sin \alpha \\ 0 & \sin \alpha & \cos \alpha \end{bmatrix} \begin{bmatrix} \cos \beta & 0 & \sin \beta \\ 0 & 1 & 0 \\ -\sin \beta & 0 & \cos \beta \end{bmatrix} \begin{bmatrix} \cos \gamma & -\sin \gamma & 0 \\ \sin \gamma & \cos \gamma & 0 \\ 0 & 0 & 1 \end{bmatrix} \\ = \begin{bmatrix} c_{11} & c_{12} & c_{13} \\ c_{21} & c_{22} & c_{23} \\ c_{31} & c_{32} & c_{33} \end{bmatrix} \quad (4.110) \end{aligned}$$

Consequently

$$\overline{\text{AB}}^{(0)} = e^{\tilde{u}_1\alpha} e^{\tilde{u}_2\beta} e^{\tilde{u}_3\gamma} = [r_{ix}\bar{u}_1 + r_{iy}\bar{u}_2 + r_{iz}\bar{u}_3] \quad (4.111)$$

Vector $\overline{\text{AB}}^{(0)}$ is composed of known parameters and for simplification it can be written as follow.

$$\overrightarrow{\text{AB}} = b_{ix}\vec{u}_1^{(0)} + b_{iy}\vec{u}_2^{(0)} + b_{iz}\vec{u}_3^{(0)} \quad (4.112)$$

Now the equation 4-98 can be modified by substituting of the above vectors.

$$\begin{aligned} X\vec{u}_1^{(0)} + Y\vec{u}_2^{(0)} + Z\vec{u}_3^{(0)} + b_{ix}\vec{u}_1^{(0)} + b_{iy}\vec{u}_2^{(0)} + b_{iz}\vec{u}_3^{(0)} &= p_{ix}\vec{u}_1^{(0)} \\ + p_{iy}\vec{u}_2^{(0)} + p_{iz}\vec{u}_3^{(0)} + \vec{u}_1^{(0)} [s_i(\cos\varphi_{1i}\cos\varphi_{2i}\cos\psi_i - \sin\varphi_{2i}\sin\psi_i)] & \\ + \vec{u}_2^{(0)} [s_i(\cos\varphi_{1i}\cos\varphi_{2i}\sin\psi_i + \sin\varphi_{2i}\cos\psi_i)] & \\ - \vec{u}_3^{(0)} [s_i\cos\varphi_{2i}\sin\varphi_{1i}] & \end{aligned} \quad (4.113)$$

3D loop closure equation leads to three scalar equations as follows.

$$s_i(\cos\varphi_{1i}\cos\varphi_{2i}\cos\psi_i) - s_i(\sin\varphi_{2i}\sin\psi_i) = X + b_{ix} - p_{ix} \quad (4.114)$$

$$s_i(\cos\varphi_{1i}\cos\varphi_{2i}\sin\psi_i) + s_i(\sin\varphi_{2i}\cos\psi_i) = Y + b_{iy} - p_{iy} \quad (4.115)$$

$$s_i\cos\varphi_{2i}\sin\varphi_{1i} = p_{iz} - Z - b_{iz} \quad (4.116)$$

Adding up square of equation 4-114 and square of equation 4-115:

$$s_i^2\cos^2\varphi_{1i}\cos^2\varphi_{2i} + s_i^2\sin^2\varphi_{2i} = (X + b_{ix} - p_{ix})^2 + (Y + b_{iy} - p_{iy})^2 \quad (4.117)$$

Squaring the equation 4-116:

$$s_i^2\cos^2\varphi_{2i}\sin^2\varphi_{1i} = (-Z - b_{iz} + p_{iz})^2 \quad (4.118)$$

Solving equations 4-114 and 4-115 together s_i and φ_{1i} and φ_{2i} can be obtained as follows.

$$s_i = \pm \sqrt{(X + b_{ix} - p_{ix})^2 + (Y + b_{iy} - p_{iy})^2 + (-Z - b_{iz} + p_{iz})^2} \quad (4.119)$$

Here negative values for strokes are not meaningful due to physical constraint, therefore

$$s_i = \sqrt{(X + b_{ix} - p_{ix})^2 + (Y + b_{iy} - p_{iy})^2 + (-Z - b_{iz} + p_{iz})^2} \quad (4.120)$$

Multiplying equation 4-114 by $\cos \psi_i$ and equation 4-115 by $\sin \psi_i$ and add them up equation 4-121 will obtain.

$$s_i(\cos \varphi_{1i} \cos \varphi_{2i}) = \cos \psi_i (X + b_{ix} - p_{ix}) + \sin \psi_i (Y + b_{iy} - p_{iy}) = \zeta_{i1} \quad (4.121)$$

Reminding equation 4-16

$$s_i \cos \varphi_{2i} \sin \varphi_{1i} = p_{iz} - Z - b_{iz} = \eta_{i1} \quad (4.122)$$

$$\varphi_{1i} = \text{atan2}(\eta_{i1}, \zeta_{i1}) \quad (4.123)$$

Two ways can be followed in order to obtain the angle φ_{2i} .

$$\begin{cases} \cos \varphi_{2i} = \frac{\zeta_{i1}}{s_i \cos \varphi_{1i}} = \zeta_{i2} \\ \sin \varphi_{2i} = \sigma_{2i} \sqrt{1 - \zeta_{i2}^2} = \eta_{i2} \quad , \quad \sigma_{i2} = \pm 1 \end{cases} \quad (4.124)$$

Consequently

$$\varphi_{2i} = \text{atan2}(\eta_{i2}, \zeta_{i2}) \quad (4.125)$$

or

$$\begin{cases} \cos \varphi_{2i} = \frac{\eta_{i1}}{s_i \sin \varphi_{1i}} = \zeta'_{i2} \\ \sin \varphi_{2i} = \sigma_{2i} \sqrt{1 - \zeta'_{i2}{}^2} = \eta'_{i2} , \quad \sigma_{i2} = \pm 1 \end{cases} \quad (4.126)$$

Consequently

$$\varphi_{2i} = \text{atan2}(\eta'_{i2}, \zeta'_{i2}) \quad (4.127)$$

The results of both approaches should be same. σ_{i2} can be positive or negative due to the lateral rotation of each motor. Taking first and second derivative of the kinematic equations using chain rule give the velocity and acceleration of the variables.

4.4.1 Dynamic analysis of a 6 DOF parallel hexapod

In Newton-Euler method 3 equations are written for force vector and 3 equations are written for moment vector, totally 6 equations are written for each body in 3D. In proposed manipulator there are 13 bodies, so in this system 78 equations are obtained. In Table 3 the interaction force and moments between bodies together with actuating torques coming from joint motors are shown.

4.4.1.1 Dynamic equations for upper platform (body 1)

Upper platform is connected to the six bodies (motor shafts) with universal joints. Force equations of the body using Newton-Euler approach can be written as follows.

$$\sum_{j=8}^{13} \vec{F}_{j1} - m_p g \vec{u}_3^0 = m_p \vec{a}_p \quad (4.128)$$

where

Table 4.3: Number of unknowns in direct dynamic of hexapod

	Joints	Bodies	Unknowns			Parameters
			\vec{F}	\vec{M}	acc.	
1	Univ.	Motor 1-Base	3	1	-	$\vec{F}_{02} = F_{021} \vec{u}_1^2 + F_{022} \vec{u}_2^2 + F_{023} \vec{u}_3^2$ $\vec{M}_{02} = M_{023} \vec{u}_3^2$
2	Univ.	Motor 2-Base	3	1	-	$\vec{F}_{03} = F_{031} \vec{u}_1^2 + F_{032} \vec{u}_2^2 + F_{033} \vec{u}_3^2$ $\vec{M}_{03} = M_{033} \vec{u}_3^2$
3	Univ.	Motor 3-Base	3	1	-	$\vec{F}_{04} = F_{041} \vec{u}_1^2 + F_{042} \vec{u}_2^2 + F_{043} \vec{u}_3^2$ $\vec{M}_{04} = M_{043} \vec{u}_3^2$
4	Univ.	Motor 4-Base	3	1	-	$\vec{F}_{05} = F_{051} \vec{u}_1^2 + F_{052} \vec{u}_2^2 + F_{053} \vec{u}_3^2$ $\vec{M}_{05} = M_{053} \vec{u}_3^2$
5	Univ.	Motor 5-Base	3	1	-	$\vec{F}_{06} = F_{061} \vec{u}_1^2 + F_{062} \vec{u}_2^2 + F_{063} \vec{u}_3^2$ $\vec{M}_{06} = M_{063} \vec{u}_3^2$
6	Univ.	Motor 6-Base	3	1	-	$\vec{F}_{07} = F_{071} \vec{u}_1^2 + F_{072} \vec{u}_2^2 + F_{073} \vec{u}_3^2$ $\vec{M}_{07} = M_{073} \vec{u}_3^2$
7	Univ.	Shaft 1-Platform	3	1	-	$\vec{F}_{81} = F_{811} \vec{u}_1^p + F_{812} \vec{u}_2^p + F_{813} \vec{u}_3^p$ $\vec{M}_{81} = M_{813} \vec{u}_3^p$
8	Univ.	Shaft 2-Platform	3	1	-	$\vec{F}_{91} = F_{911} \vec{u}_1^p + F_{912} \vec{u}_2^p + F_{913} \vec{u}_3^p$ $\vec{M}_{91} = M_{913} \vec{u}_3^p$
9	Univ.	Shaft 3-Platform	3	1	-	$\vec{F}_{101} = F_{1011} \vec{u}_1^p + F_{1012} \vec{u}_2^p + F_{1013} \vec{u}_3^p$ $\vec{M}_{101} = M_{1013} \vec{u}_3^p$
10	Univ.	Shaft 4-Platform	3	1	-	$\vec{F}_{111} = F_{1111} \vec{u}_1^p + F_{1112} \vec{u}_2^p + F_{1113} \vec{u}_3^p$ $\vec{M}_{111} = M_{1113} \vec{u}_3^p$
11	Univ.	Shaft 5-Platform	3	1	-	$\vec{F}_{121} = F_{1211} \vec{u}_1^p + F_{1212} \vec{u}_2^p + F_{1213} \vec{u}_3^p$ $\vec{M}_{121} = M_{1213} \vec{u}_3^p$
12	Univ.	Shaft 6-Platform	3	1	-	$\vec{F}_{131} = F_{1311} \vec{u}_1^p + F_{1312} \vec{u}_2^p + F_{1313} \vec{u}_3^p$ $\vec{M}_{131} = M_{1313} \vec{u}_3^p$

Table 4.4: Number of unknowns in direct dynamic of hexapod

	Joints	Bodies	Unknowns			Parameters
			\vec{F}	\vec{M}	acc.	
13	Cylin.	Motor 1-Shaft 1	2	2	-	$\vec{F}_{82} = F_{822} \vec{u}_2^2 + F_{823} \vec{u}_3^2$ $\vec{M}_{82} = M_{822} \vec{u}_2^2 + M_{823} \vec{u}_3^2$
14	Cylin.	Motor 2-Shaft 2	2	2	-	$\vec{F}_{93} = F_{932} \vec{u}_2^2 + F_{933} \vec{u}_3^2$ $\vec{M}_{93} = M_{932} \vec{u}_2^2 + M_{933} \vec{u}_3^2$
15	Cylin.	Motor 3-Shaft 3	2	2	-	$\vec{F}_{104} = F_{1042} \vec{u}_2^2 + F_{1043} \vec{u}_3^2$ $\vec{M}_{104} = M_{1042} \vec{u}_2^2 + M_{1043} \vec{u}_3^2$
16	Cylin.	Motor 4-Shaft 4	2	2	-	$\vec{F}_{115} = F_{1152} \vec{u}_2^2 + F_{1153} \vec{u}_3^2$ $\vec{M}_{115} = M_{1152} \vec{u}_2^2 + M_{1153} \vec{u}_3^2$
17	Cylin.	Motor 5-Shaft 5	2	2	-	$\vec{F}_{126} = F_{1262} \vec{u}_2^2 + F_{1263} \vec{u}_3^2$ $\vec{M}_{126} = M_{1262} \vec{u}_2^2 + M_{1263} \vec{u}_3^2$
18	Cylin.	Motor 6-Shaft 6	2	2	-	$\vec{F}_{137} = F_{1372} \vec{u}_2^2 + F_{1373} \vec{u}_3^2$ $\vec{M}_{137} = M_{1372} \vec{u}_2^2 + M_{1373} \vec{u}_3^2$
19	Motion	Platform acc.	-	-	6	$\ddot{X}, \ddot{Y}, \ddot{Z}, \ddot{\alpha}, \ddot{\beta}, \ddot{\gamma}$
Total			48	24	6	78 Unnowns

$$\vec{F}_{j1} = F_{j11} \vec{u}_1^p + F_{j12} \vec{u}_2^p + F_{j13} \vec{u}_3^p \quad (4.129)$$

In above equation j is number of the bodies (shaft) that are connected to the platform and varies from 8 to 13.

$$\begin{aligned} \vec{u}_3^0 &= [-\cos(\alpha) \sin(\beta) \cos(\gamma) + \sin(\alpha) \sin(\gamma)] \vec{u}_1^p \\ &+ [\cos(\alpha) \sin(\beta) \sin(\gamma) + \sin(\alpha) \cos(\gamma)] \vec{u}_2^p \\ &+ [\cos(\alpha) \cos(\beta)] \vec{u}_3^p \end{aligned} \quad (4.130)$$

\vec{a}_p has been obtained in kinematic analysis of the platform. Three scalar equa-

tions can be extracted from above equation.

$$\sum_{j=8}^{13} \vec{F}_{j11} - m_p g [-\cos(\alpha) \sin(\beta) \cos(\gamma) + \sin(\alpha) \sin(\gamma)] = m_p \vec{a}_{p1} \quad (4.131)$$

$$\sum_{j=8}^{13} \vec{F}_{j12} - m_p g [\cos(\alpha) \sin(\beta) \sin(\gamma) + \sin(\alpha) \cos(\gamma)] = m_p \vec{a}_{p2} \quad (4.132)$$

$$\sum_{j=8}^{13} \vec{F}_{j13} - m_p g [\cos(\alpha) \cos(\beta)] = m_p \vec{a}_{p3} \quad (4.133)$$

Moment equations of the body using Newton-Euler approach can be written as follows where $\overrightarrow{C_1 B_j}$ is a vector that connects center of platform to the connection point with j^{th} shaft.

$$\sum_{j=8}^{13} (\overrightarrow{C_1 B_j} \times \vec{F}_{j1}) + \sum_{j=8}^{13} \vec{M}_{j1} = \check{J}_p \cdot \vec{\alpha}_{p/0} + \vec{\omega}_{p/0} \times \check{J}_p \cdot \vec{\omega}_{p/0} \quad (4.134)$$

where

$$\overrightarrow{C_1 B_j} = c_1 b_{j1} \vec{u}_1^p + c_1 b_{j2} \vec{u}_2^p + c_1 b_{j3} \vec{u}_3^p \quad (4.135)$$

$$\vec{M}_{j1} = -c_{j1} \dot{\alpha} \vec{u}_1^p - c_{j1} \dot{\beta} \vec{u}_2^p + M_{j13} \vec{u}_3^p \quad (j = 8 - 13 \text{ for platform}) \quad (4.136)$$

In above equation j is number of the bodies (shafts) that are connected to the platform and varies from 8 to 13. Also c_{j1} are viscous friction coefficients regarding to the universal joints. \check{J}_p is platform moment of inertia dyadic. Same as force equation, 3 scalar equations will be derived from moment equations.

4.4.1.2 Dynamic equations for motors 1-6 (bodies 2-7)

Motor bodies are connected to 2 bodies that one of them is base plate using a universal joint and the other one is related shaft using a cylindrical joint. So

the dynamic force equations for each motor can be written using Newton-Euler approach as follows. The mass of all motors are same so we call them m_m .

$$\vec{F}_{0j} + \vec{F}_{kj} - m_p g \vec{u}_3^0 = m_m \vec{a}_j \quad (4.137)$$

In the above equation, \vec{F}_{0j} is the force vector that coming from base of the hexapod and acts on the motor body j . Also \vec{F}_{kj} is the force vector coming from related shaft and acts on the motor. The index j is body number and varies from 2-7 and index k is related to the shaft body number and varies from 8-13 respectively. The dynamic moment equations for bodies 2 -7 can be written using Newton-Euler approach as follows.

$$\overrightarrow{C_j D} \times \vec{F}_{0j} + \overrightarrow{C_j C_k} \times \vec{F}_{kj} + \vec{M}_{0j} + \vec{M}_{kj} = \check{J}_m \cdot \check{\alpha}_{j/0} + \check{\omega}_{j/0} \times \check{J}_m \cdot \check{\omega}_{j/0} \quad (4.138)$$

where

$$\overrightarrow{C_j D} = c_j d_{11} \vec{u}_1^2 + c_j d_3 \vec{u}_3^2 \quad (4.139)$$

$$\overrightarrow{C_j C_k} = (s_i + c_j c_{k1}) \vec{u}_1^2 + c_j c_{kj} \vec{u}_3^2 \quad (4.140)$$

Using the same procedure as we done for platform (body 1) it is possible to write 6 equations for each motor (3 force equations/3 moment equations).

4.4.1.3 Dynamic equations for shafts 1-6 (bodies 8-13)

Motor shafts are connected to 2 bodies that one of them is upper platform using a universal joint and the other one is related motor using a cylindrical joint. So the dynamic force equations can be written using Newton-Euler approach as follows. The mass of all shafts are same so we call them m_{shaft} .

$$\vec{F}_{jk} + \vec{F}_{1k} - m_{\text{shaft}} g \vec{u}_3^0 = m_{\text{shaft}} \vec{a}_k \quad (4.141)$$

where

$$\vec{F}_{jk} = -\vec{F}_{kj} = F_i \vec{u}_1^2 - F_{kj2} \vec{u}_2^2 - F_{kj3} \vec{u}_3^2 \quad (4.142)$$

$$\vec{F}_{1k} = -\vec{F}_{k1} = -F_{k11} \vec{u}_1^p - F_{k12} \vec{u}_2^p - F_{k13} \vec{u}_3^p \quad (4.143)$$

In the above equations, \vec{F}_{jk} is the force vector that coming from motor body j acts on the related shaft (body k). Also \vec{F}_{1k} is the force vector coming from upper platform and acts on the relate shaft (body k). Also F_i is actuating torque of related motor. Equation should be expressed in shaft body fixed frame 2 in matrix notation.

$$\bar{F}_{1k}^{(2)} = -F_{k11} \bar{u}_1^{(P/2)} - F_{k12} \bar{u}_2^{(P/2)} - F_{k13} \bar{u}_3^{(P/2)} \quad (4.144)$$

$$\bar{F}_{1k}^{(2)} = -F_{k11} \hat{C}^{(2,p)} \bar{u}_1^{(P/p)} - F_{k12} \hat{C}^{(2,p)} \bar{u}_2^{(P/p)} - F_{k13} \hat{C}^{(2,p)} \bar{u}_3^{(P/p)} \quad (4.145)$$

$\hat{C}^{(2,p)}$ is rotation matrix that transfer shaft fixed frame 2 to platform fixed frame p .

$$\hat{C}^{(2,p)} = \hat{C}^{(2,1)} \hat{C}^{(1,0)} \hat{C}^{(0,\alpha)} \hat{C}^{(\alpha,\beta)} \hat{C}^{(\beta,\gamma)} \quad (4.146)$$

The dynamic moment equations for bodies 8 -13 can be written using Newton-Euler approach as follows.

$$\begin{aligned} \overrightarrow{C_k C_j} \times \overrightarrow{F_{jk}} + \overrightarrow{C_k B_i} \times \overrightarrow{F_{1k}} + \overrightarrow{M_{jk}} + \overrightarrow{M_{1k}} &= \check{J}_{\text{shaft}} \cdot \check{\alpha}_{j/0} \\ &+ \check{\omega}_{j/0} \times \check{J}_{\text{shaft}} \cdot \check{\omega}_{j/0} \end{aligned} \quad (4.147)$$

Using the same procedure as we done for platform (body 1) it is possible to write 6 equations for each motor (3 force equations/3 moment equations).

So the equations can be written in matrix format as follows in order to calculate direct kinematics of the manipulator.

$$[Coefficients]_{78 \times 78} \cdot \begin{bmatrix} \ddot{X} \\ \ddot{Y} \\ \ddot{Z} \\ \ddot{\alpha} \\ \ddot{\beta} \\ \ddot{\gamma} \\ \overline{F}_{(base,motor_i),1} \\ \overline{F}_{(base,motor_i),2} \\ \overline{F}_{(base,motor_i),3} \\ \overline{M}_{(base,motor_i),3} \\ \overline{F}_{(shaft_i,platform),1} \\ \overline{F}_{(shaft_i,platform),2} \\ \overline{F}_{(shaft_i,platform),3} \\ \overline{M}_{(shaft_i,platform),3} \\ \overline{F}_{(motor_i,shaft_i),2} \\ \overline{F}_{(motor_i,shaft_i),3} \\ \overline{M}_{(motor_i,shaft_i),2} \\ \overline{M}_{(motor_i,shaft_i),3} \end{bmatrix}_{78 \times 1} = [Known\ parameters]_{78 \times 1} \quad (4.148)$$

A model and simulation of the prallel hexapod robot is developed using MATLAB[®] Simscape toolbox (Figure 4.14).

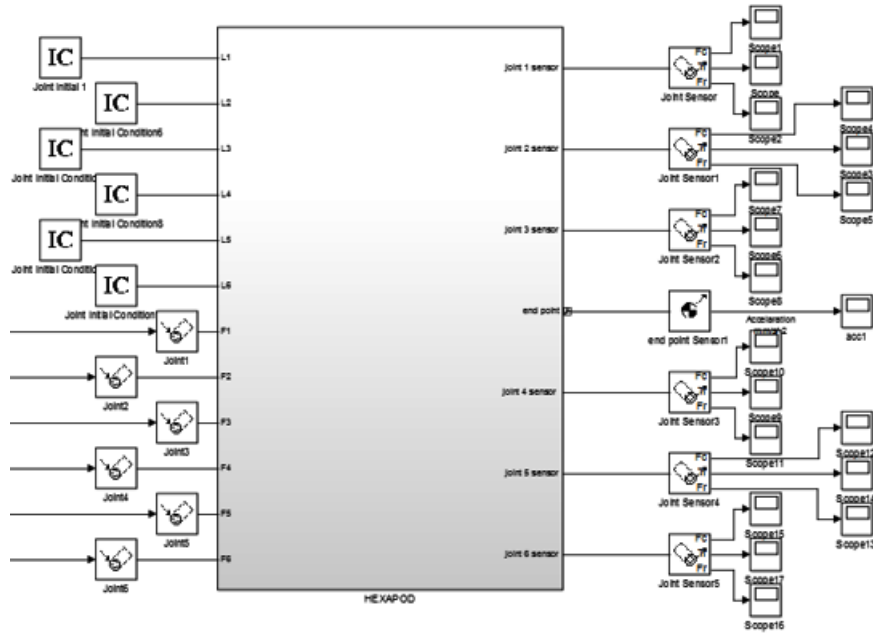
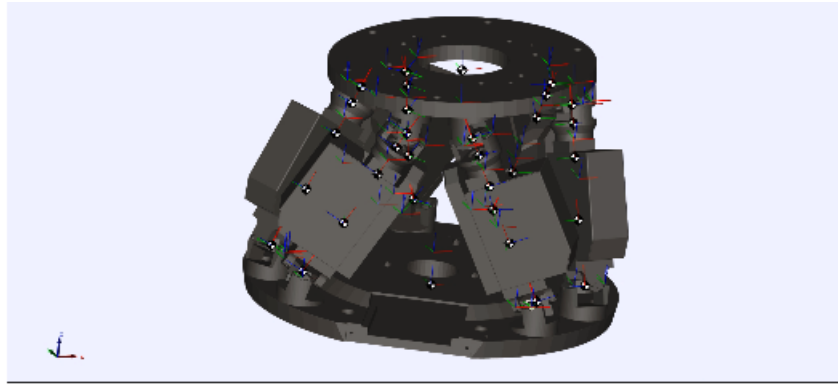


Figure 4.14: MATLAB[®] Simscape model of parallel hexapod robot

4.4.2 Connecting serial and parallel manipulators

In order to match the parallel and serial parts of the hybrid manipulator, two different strategies can be implemented. The first method is to solve the dynamic equations of the serial and parallel manipulators simultaneously. It means that a 114×114 coefficients matrix should be generated in order to solve and obtain all unknown parameters simultaneously. While writing the equations of hexapod, the mass center position vector of each body should be expressed in the inertial reference frame that is assigned on base of the serial manipulator.

Then the first and second derivatives of the position vectors should be done in the inertial reference frame in order to calculate the acceleration vector of the mass center and use it in the dynamic equation. This approach gives exact analytical solutions of the unknowns and it is the most important advantage of the mentioned method. But twice derivation of the mass center position vector in inertial frame gives so long expressions, because it is function of all joint variables and joint velocities and acceleration. That's why it is hard to use this approach especially for real time applications. Therefore second approach is planned to be used for the dynamic analysis of hybrid manipulator in certain conditions. At this proposed method the dynamic analysis of serial and parallel parts will done separately, then the resultant reaction forces/torques coming from hexapod strokes to its base, will be given to the 6th body of the serial manipulator as external forces/torques. The challenging side of this approach is how to add Coriolis effect of hexapod on the serial manipulator. For solving this problem, the hexapod can be considered as a rigid body that is fixed to the 6th body of the serial manipulator. So the 6th body of the ABB manipulator should be modified as combination of 6'th link of it and the hexapod while calculating the center of mass acceleration. In order to apply this assumption with good accuracy the hexapod should not work with high acceleration. Here 6 DOF PI H-824 hexapod is used as parallel part of the hybrid manipulator where its maximum velocity is 1 mm/s and its acceleration is very low. Also here the critical joint is the fifth joint (wrist) of the serial manipulator and the cost function while path optimization of the redundant manipulator is minimization of reaction forces/torques on this critical joint. Consequently it is possible to use the second approach for dynamic analysis. The advantage of this method is simplicity of calculation and quick response of dynamic model that make it suitable for real time applications. The disadvantage is decrease of accuracy if the hexapod has sharp and fast motion.

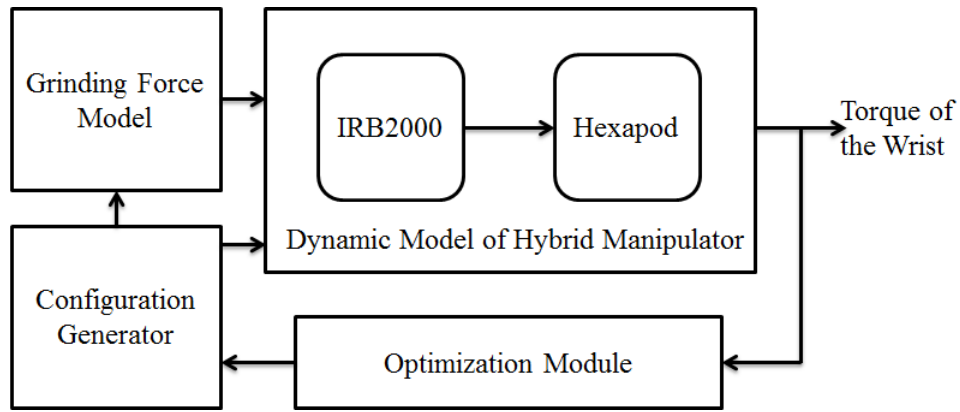


Figure 4.15: Posture optimization process

4.5 Posture optimization of 12 DOF hybrid redundant manipulator

The main aim here is to posture optimization of the 12 DOF hybrid redundant manipulator. Different criteria can be defined as cost function of the optimization problem. Here the fifth joint (wrist) of the ABB serial manipulator is the weakest joint in the robot, so the computed torque of this joint is selected as the cost function. The aim is to minimize this factor by finding the optimum configuration of the hybrid manipulator. For such a purpose we need to calculate the torque of the wrist joint for different possible configurations and select the best one. The dynamic model of the 12 DOF manipulator.

The output of the grinding force model is given to the dynamic model as an external reaction force. The dynamic model calculates all reaction parameters and torques of the joints. The computed torque of the wrist joint is given to the optimization module and new configuration is generated by the module with respect to the kinematics of the 12 DOF redundant manipulator. Then it is given to the dynamic model. This module searches among infinite kinematic solutions of the redundant manipulator, and assigns translation and orientation values for the hexapod. Based on these values and using inverse kinematics of hexapod the location and orientation of connection point between hexapod and ABB robot in the work space are calculated. At the same time, this connec-

tion point is tip point of the ABB manipulator. Consequently with known tip point location and tip point orientation matrix, the joint variables of the serial robot are obtained using inverse kinematics that is explained in Section 4.3.2. This process continues until converge to the minimum torque value. Then the optimal configuration is chosen for the grinding operation (Figure 4.15). The SIMULINK model of the posture optimization process is shown in Figure 4.16.

The optimization process can be implemented in two methods.

The first optimization method is useful when the operator wants to implement the grinding operation with a desired orientation. The desired grinding orientation is identified with respect to the workpiece profile and grinding geometry. In this method the desired orientation and location of the hybrid manipulator tip point should be defined by the operator. The optimization algorithm finds the optimum posture of the robot with respect to the given position and orientation.

If we consider the desired orientation of the tip point as Euler angles α_g , β_g and γ_g with the 1-2-3 sequence, and the desired tip point location as X_g , Y_g and Z_g in inertial coordinate system, there are infinite configurations to reach such a location and orientation in the work space. The transformation homogenous matrix of desired tip point location can be written as follows.

$$\hat{T}_{desired} = \begin{bmatrix} \hat{C}_{desired} & \overline{r_{desired}}^{(G)} \\ 0 & 1 \end{bmatrix} \quad (4.149)$$

where

$$\hat{C}_{desired} = e^{\tilde{u}_1 \alpha_g} e^{\tilde{u}_2 \beta_g} e^{\tilde{u}_3 \gamma_g} \quad (4.150)$$

so

$$\begin{bmatrix} 1 & 0 & 0 \\ 0 & \cos \alpha_g & -\sin \alpha_g \\ 0 & \sin \alpha_g & \cos \alpha_g \end{bmatrix} \begin{bmatrix} \cos \beta_g & 0 & \sin \beta_g \\ 0 & 1 & 0 \\ -\sin \beta_g & 0 & \cos \beta_g \end{bmatrix} \begin{bmatrix} \cos \gamma_g & -\sin \gamma_g & 0 \\ \sin \gamma_g & \cos \gamma_g & 0 \\ 0 & 0 & 1 \end{bmatrix} \hat{C}_{desired} = \quad (4.151)$$

$$\overline{r}_{desired}^{(G)} = \begin{bmatrix} X_g \\ Y_g \\ Z_g \end{bmatrix} \quad (4.152)$$

$$\hat{T}_{IRB2000} \hat{T}_{hexapod} = \hat{T}_{desired} \quad (4.153)$$

$$\hat{C}_{hexapod} = \hat{C}^{(0,6)} e^{\tilde{u}_1 \alpha} e^{\tilde{u}_2 \beta} e^{\tilde{u}_3 \gamma} \quad (4.154)$$

For finding new configuration that takes the robot to the same desired location with same desired orientation the new position and orientation of serial IRB 2000 manipulator can be obtained as follows. The search algorithm identifies new transformation homogenous matrix of the hexapod $\hat{T}_{hexapod}^{new}$ from infinite possible selections. Consequently the new transformation homogenous matrix of the ABB IRB 2000 robot is identified considering new hexapod configuration.

$$\hat{T}_{IRB2000}^{new} = \hat{T}_{desired} \left(\hat{T}_{hexapod}^{new} \right)^{-1} \quad (4.155)$$

Using the new transformation homogenous matrix and the inverse kinematics of the IRB 2000 robot that is explained in Section 4.3.2, the new joint variables are obtained. Also with inverse kinematics of the hexapod (Section 4.4), new values of struts lengths are obtained. An example of posture optimization of 12 DOF hybrid manipulator based on torque minimization in wrist joint is shown in Figure 4.17 and Figure 4.18 respectively. Genetic algorithm (GA) toolbox of MATLAB R2017a is used as signal optimization method in this example.

The second optimization method is useful for grinding with ball-shape tools where the operator wants to implement the grinding operation with an optimum orientation. Here the due to ball-shape tool, the tip point orientation is not important. Just the desired location of the hybrid manipulator tip point should be defined with respect to the workpiece geometry.

The optimization algorithm finds the optimum posture of the robot with respect to the given position. If we consider the desired tip point location as X_o , Y_o and Z_o in inertial coordinate system, same as the first method, there are infinite configurations to reach such a location. The main difference between first and second approach is that in the first method, optimization module is implemented in 6 dimensional space but in the second approach considering grinding orientation angles in parallel with hexapod orientation and translation parameters, the optimization module is implemented in 9 dimensional space. In this method the outputs of the optimization algorithm are optimal grinding orientations (α_g , β_g and γ_g) and the optimal configuration of the robot that leads to the minimum computed torque in wrist joint of the IRB2000 manipulator.

The transformation homogenous matrix of desired tip point location can be written as follows.

$$\hat{T}_{desired} = \begin{bmatrix} \hat{C}_{desired} & \overline{r_{desired}}^{(G)} \\ 0 & 0 & 0 & 1 \end{bmatrix} \quad (4.156)$$

where

$$\hat{C}_{desired} = e^{\tilde{u}_1 \alpha_o} e^{\tilde{u}_2 \beta_o} e^{\tilde{u}_3 \gamma_o} \quad (4.157)$$

so

$$\begin{bmatrix} 1 & 0 & 0 \\ 0 & \cos \alpha_o & -\sin \alpha_o \\ 0 & \sin \alpha_o & \cos \alpha_o \end{bmatrix} \begin{bmatrix} \cos \beta_o & 0 & \sin \beta_o \\ 0 & 1 & 0 \\ -\sin \beta_o & 0 & \cos \beta_o \end{bmatrix} \begin{bmatrix} \cos \gamma_o & -\sin \gamma_o & 0 \\ \sin \gamma_o & \cos \gamma_o & 0 \\ 0 & 0 & 1 \end{bmatrix} \hat{C}_{desired} = \quad (4.158)$$

$$\overline{r}_{desired}^{(G)} = \begin{bmatrix} X_g \\ Y_g \\ Z_g \end{bmatrix} \quad (4.159)$$

$$\hat{T}_{IRB2000} \hat{T}_{hexapod} = \hat{T}_{desired} \quad (4.160)$$

$$\hat{C}_{hexapod} = \hat{C}^{(0,6)} e^{\tilde{u}_1 \alpha} e^{\tilde{u}_2 \beta} e^{\tilde{u}_3 \gamma} \quad (4.161)$$

Same as the previous optimization method, the new position and orientation of serial IRB 2000 manipulator can be obtained as follows.

$$\hat{T}_{IRB2000}^{new} = \hat{T}_{desired} \left(\hat{T}_{hexapod}^{new} \right)^{-1} \quad (4.162)$$

The new joint variables are obtained using the new transformation homogenous matrix and the inverse kinematics of the IRB 2000 robot. Also the new values of struts lengths are obtained with inverse kinematics of the hexapod. An example of posture optimization of hybrid manipulator using second optimization approach is shown in Figure 4.19 and Figure 4.20 respectively. Genetic algorithm (GA) is used as optimization method in this example.

4.5.1 Posture optimization along the grinding path

Two approaches for posture optimization of hybrid redundant manipulator re explained. Such an optimization should be implemented along the grinding path.

Table 4.5: Motion range of the PI H-824 Hexapod

Motion	Range
Travel range X	$\pm 22.5mm$
Travel range Y	$\pm 22.5mm$
Travel range Z	$\pm 12.5mm$
Travel range α	$\pm 7.5^\circ$
Travel range β	$\pm 7.5^\circ$
Travel range γ	$\pm 12.5^\circ$

An offline simulation is done for finding optimal posture of the manipulator in all parts of the grinding path. The grinding path is divided to the small parts and in each part the normal and tangential grinding forces are estimated by the grinding force model as shown in Figure 4.21.

The challenge here is to prevent sharp motion by the manipulator during the posture optimization. Also the joints motion limitations should be considered in posture optimization procedure. Based on the workpiece dimensions and works space of the robot, the motion range that are considered for each joint of the ABB IRB2000 manipulator is $\pm 60^\circ$ degrees. The motion limitations of PI H-824 Hexapod are shown in Table 4.4.

The goal is to find the nearest configuration of the manipulator that leads local minima of the wrist joint computed torque. The flowchart of the posture optimization algorithm is shown in Figure 4.22. At the beginning of the operation a user defined start point is given the optimization algorithm. The mentioned starting point is a user selected configuration for the position that workpiece begins ($x = x_0$). After this step, the starting point of optimization algorithm is considered as the present configuration of the robot. This method helps the optimization algorithm to converge to the closest optimum posture in each iteration without any sharp and unstable motion.

An example of a posture optimization along a 2D path is shown in Figure 4.23. The optimized posture of the robot in three points of the defined path are shown in this Figure.

A simulation of posture optimization during grinding operation on a manifold is shown in Figure 4.24. The optimized posture of the robot in two points of the manifold surface are shown in this Figure.

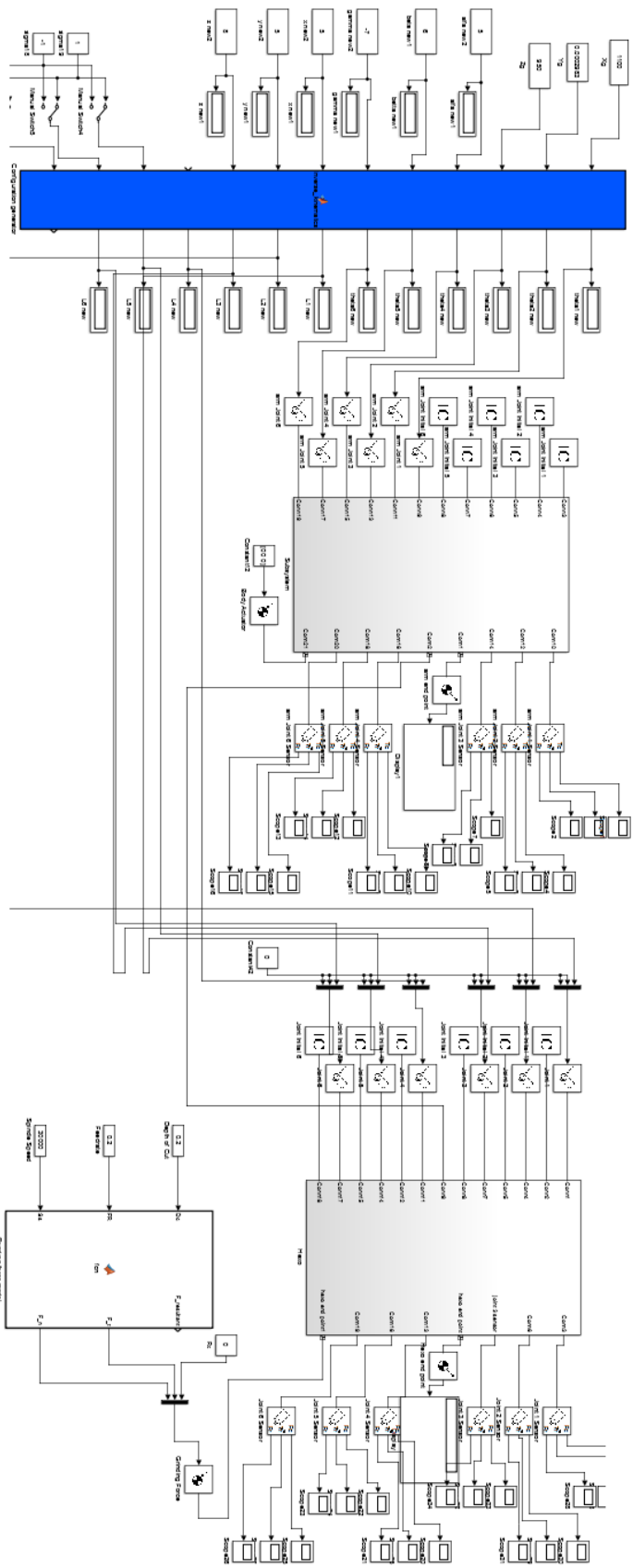


Figure 4.16: SIMULINK model of the posture optimization process

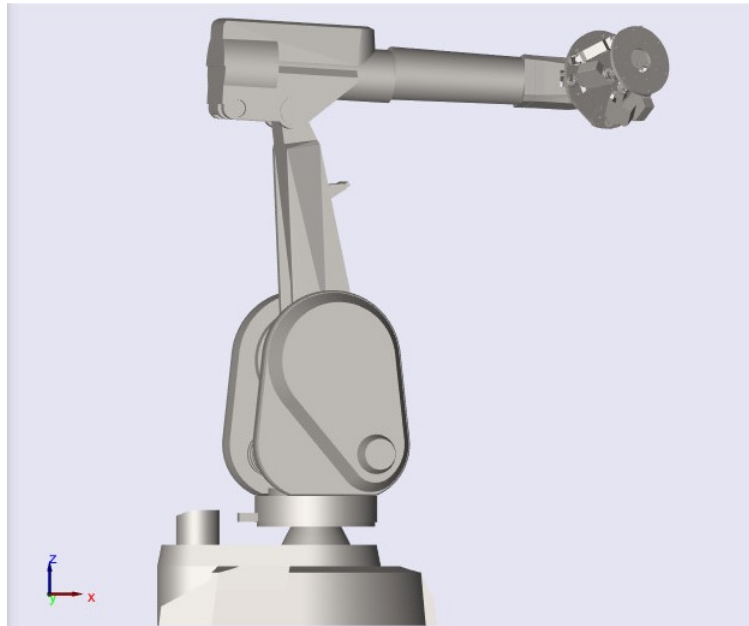


Figure 4.17: Posture optimization of 12 DOF hybrid redundant manipulator with first method

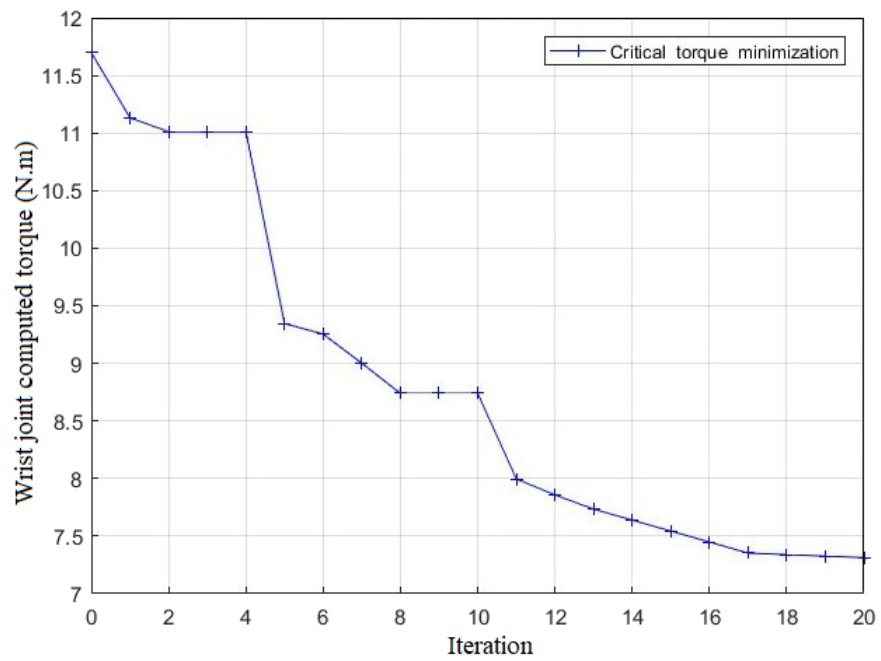


Figure 4.18: Wrist joint computed torque minimization using first optimization approach

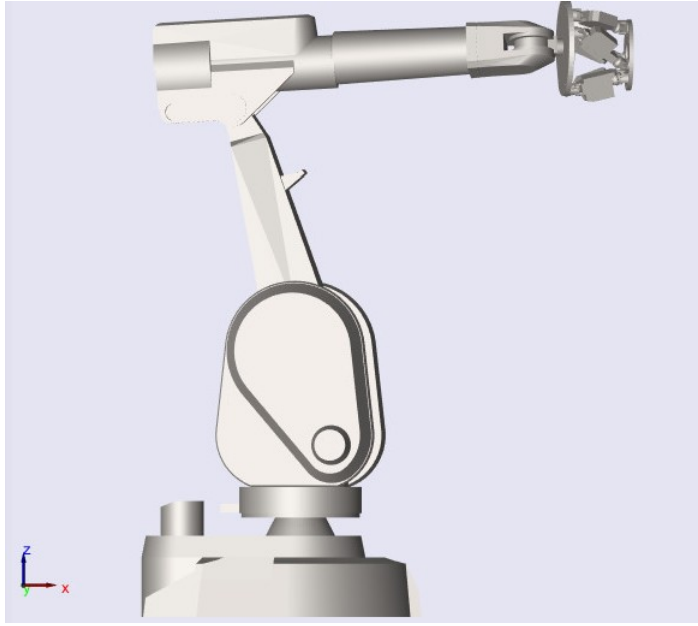


Figure 4.19: Posture optimization of 12 DOF hybrid redundant manipulator with second method

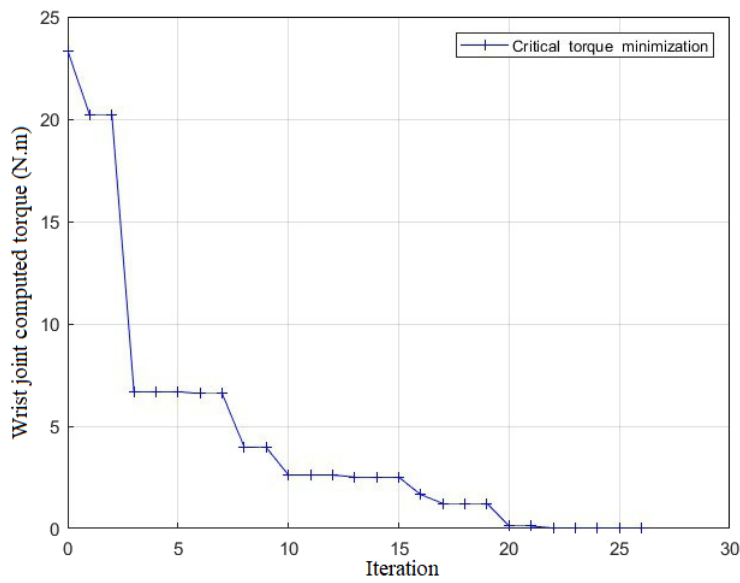


Figure 4.20: Wrist joint computed torque minimization using second optimization approach

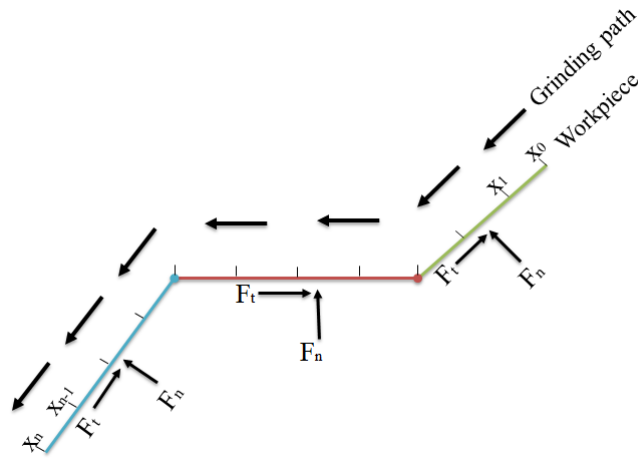


Figure 4.21: Grinding path and calculated normal and tangential grinding forces along path

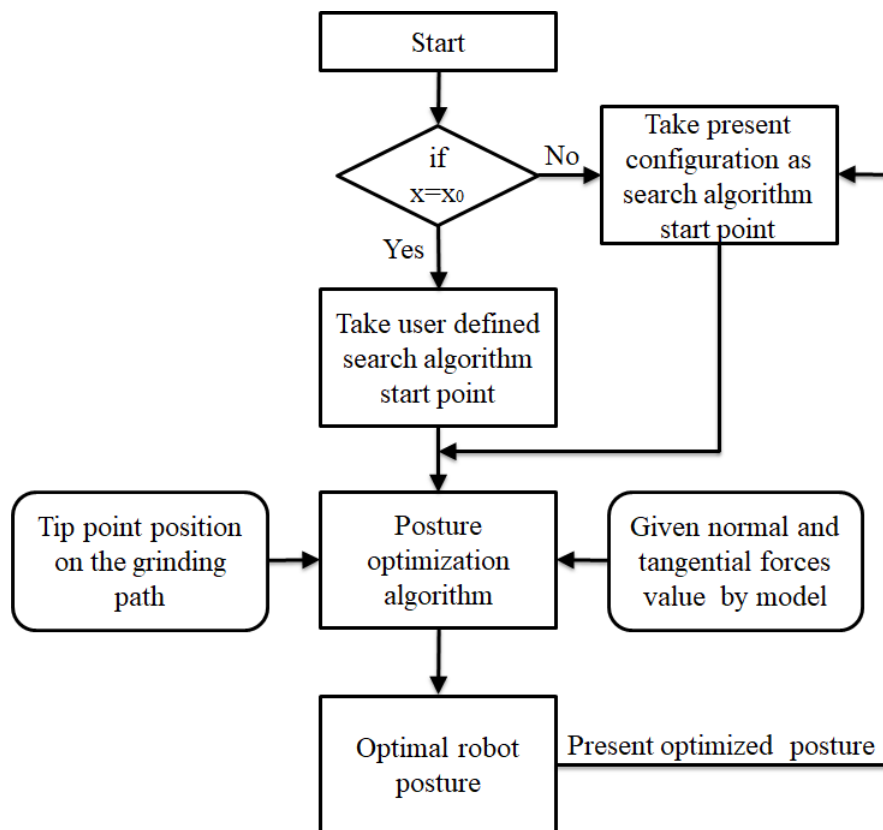


Figure 4.22: Flowchart of the posture optimization algorithm

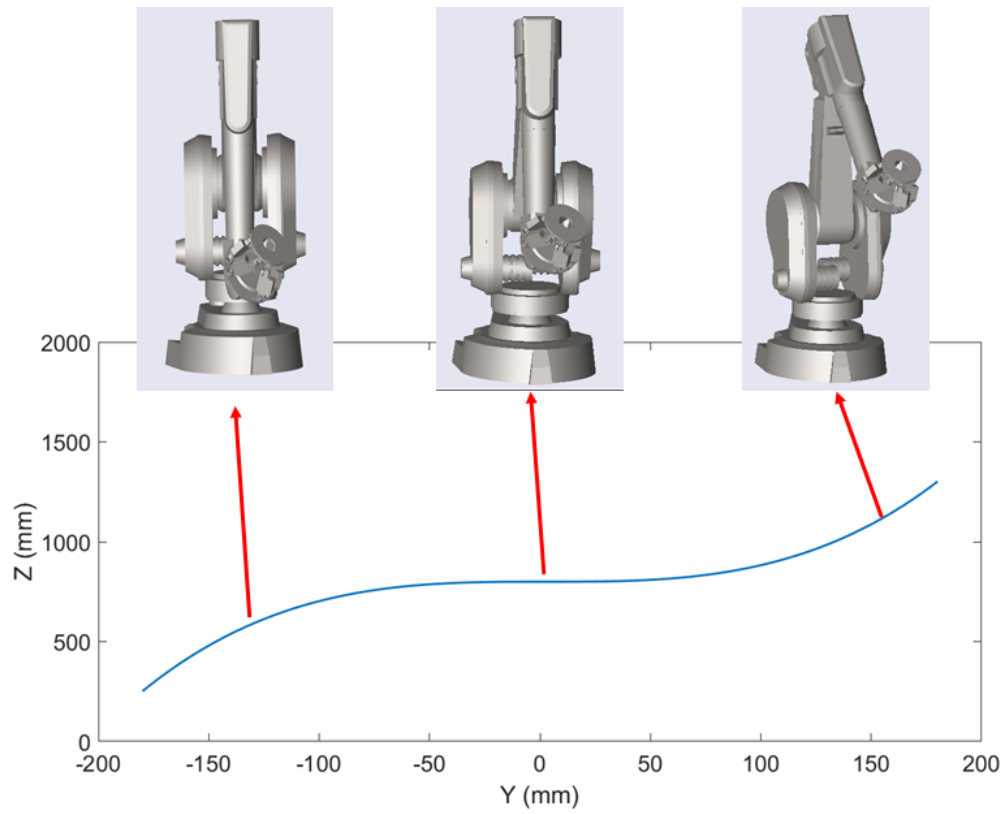


Figure 4.23: Example of posture optimization along a path

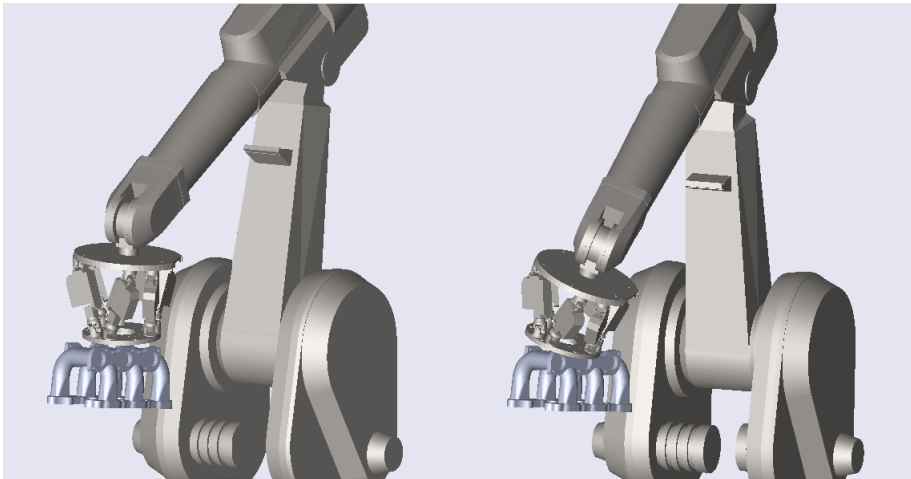


Figure 4.24: Simulation of posture optimization during grinding operation on a manifold

CHAPTER 5

CONCLUSION

In the robotic grinding operation, the effects of tool and setup stiffness are more important than grinding with universal machines that are highly stiff. The results show a significant effect of the tool and setup deflections on the normal grinding force and, consequently, on the equivalent grinding force. Accurate force prediction is important for automatic robotic grinding operation because accurate prediction of grinding forces helps to perform the operation with constant force and prevent geometrical errors. In this thesis, a physical grinding force model that uses chip formation energy and sliding energy is used where classic grinding parameters (spindle velocity, feed rate and the depth of cut) are applied as predictors. In this study, the model is modified as follows in order to increase its accuracy and to adapt it to robotic grinding.

- Hexapod, tool and workpiece mechanical properties are included in the proposed surface grinding force model by adding a refining term to the physical model. The refining term improves the accuracy of the grinding force estimation and makes the model more applicable for robotic grinding.
- To extract workpiece and setup properties, penetration tests are implemented, new features are extracted from test results and these features are used in refining the model.
- The feedback from the spindle during the tests is analyzed. The outcomes

of the analysis show a high correlation between the grinding forces and the spindle percent load, where the percent load is a function of the spindle current. The percent load is used in refining the model.

- The proposed force model is more accurate in comparison with the energy-based force model. Comparison of RMSE of grinding force prediction by energy-based model and proposed model showed improvement in prediction accuracy especially in the prediction of the normal grinding force.
- The model is adaptable for different setups and conditions. There is no need to calculate such parameters as the stiffness of the robot, spindle, tool, workpiece, joints, and connections separately. Because all of the factors and workpiece mechanical properties reflect their effects on the features that are extracted from the penetration test graphs. The refining term of the model includes the above factors in the force model indirectly. For a new setup or new operating conditions, by implementing a penetration test and extracting the necessary features, the model can easily be updated.

As a conclusion, robotic surface grinding operations can be classified in three regimes based on force response.

- In the first regime, the grinding forces remain almost constant during the operation. This regime is similar to the universal grinding machine response, where the tool cuts the workpiece with a set feed rate with negligible tool deflection. It is possible to apply the existed grinding models in certain conditions for this regime.
- In the second regime, the grinding forces increase almost linearly during the operation. This phenomenon is due to tool deflection and is similar to the ascending section of the penetration test graph, where a tool cannot

cut the workpiece with a set feed rate.

- The third regime includes a transition response where a small tool deflection occurs followed by fast compensation. This response causes a fluctuation in the force graphs when both deflection and compensation occurs.
- In the second and third regimes, even when the classic grinding variables (spindle speed, feed rate and the depth of cut) are constant, the grinding forces change. Therefore, the predictors alone are not sufficient to generate an efficient force model. In this condition, the spindle percent load is an extra predictor that varies with the grinding forces, even when the other predictors are constant. Consequently, the proposed model has the ability to track force changes in the second and third regimes.
- The model in this study can be used for efficient classification of the grinding operation regimes and prediction of the grinding forces.

In this thesis, a novel approach is proposed for parallel hexapod-robotic light abrasive grinding with constant resultant grinding force and real-time TDC. For this purpose, a model supervised fuzzy admittance controller is proposed for the robotic grinding operation with constant resultant force. The robotic grinding behavior is different from grinding with common CNC-type stiff machines. For reference force generation the proposed grinding force model is used that is designed for robotic grinding operations. In grinding operation the tool deflection is the main disadvantage which causes geometrical error (inclined profile) in the cross-section of the workpiece. A method for calculation of tool deflection in tangential and normal directions is utilized, combined with a kinematic solution for real-time compensation of the tool deflection. Application of this approach leads to obtain disinclined cross-section.

Investigating the results of experiments, the following inferences are concluded.

- Resultant force control is an effective method for preventing geometrical errors in robotic grinding operation.
- The resultant grinding force can be adjusted in real-time by controlling the depth of cut and its rate of change.
- The tuned realistic reference input produced by the force model, combined with the functionality of the fuzzy controller for nonlinear plants, provides a proper method for increasing the accuracy of robotic grinding operations.
- The proposed model supervised fuzzy control structure decreases the instability probability of the fuzzy controller because of the realistic reference input profile produced by the grinding model.
- Computation of the tool deflection value as a function of grinding forces and compensation of it in real time during the robotic grinding operation is an effective way of preventing geometrical errors in workpiece cross-section.

Hybrid manipulators are suitable choices in order to use advantages of serial and parallel manipulator simultaneously. Combination of large workspace of serial manipulators and high work load and accuracy of parallel manipulators makes the hybrid manipulators as suitable choice in many operations like grinding and deburring. In this thesis a 12 DOF hybrid manipulator is investigated that is composed of a 6 DOF serial ABB IRB2000 robot and a 6 DOF PI H-824 Hexapod. The Parallel hexapod is connected to the end of the serial ABB manipulator. Kinematic and dynamic analysis of the hybrid manipulator is done and all reaction/actuating forces and torques are calculated. A novel strategy for posture optimization of the redundant hybrid manipulator based on minimization of the computed torque of wrist joint of serial part of the hybrid manipulator is proposed in this study. There are infinite inverse kinematic solutions for a

redundant manipulator. A configuration generator module is developed in order to generate inverse kinematic solutions for a desired tip point location and orientation. A GA search approach is used to find optimum solution that leads minimum torque in the wrist joint. Also it is possible to find optimum grinding orientation in the work space if there is not any desired grinding orientation. It is concluded that posture optimization in a redundant manipulator is a useful approach for obtaining optimum force or torque value in joints of a manipulator. For the hybrid redundant manipulator that is focused in this thesis, the different optimization criteria like minimization of all joints actuating torques can be used as future works. The real-time posture optimization of the redundant manipulator can be another research topic where a parallel processing solution can be investigated for this topic.

REFERENCES

- [1] Abdel-Rahman, T. M. (1991). A generalized practical method for analytic solution of the constrained inverse kinematics problem of redundant manipulators. *The International journal of robotics research*, 10(4):382–395.
- [2] Agirrebeitia, J., Aviles, R., de Bustos, I. F., and Ajuria, G. (2003). Inverse position problem in highly redundant multibody systems in environments with obstacles. *Mechanism and machine theory*, 38(11):1215–1235.
- [3] Amamou, R., Fredj, N. B., and Fnaiech, F. (2008). Improved method for grinding force prediction based on neural network. *The International Journal of Advanced Manufacturing Technology*, 39(7-8):656–668.
- [4] Arnaiz-González, Á., Fernández-Valdivielso, A., Bustillo, A., and López de Lacalle, L. N. (2016). Using artificial neural networks for the prediction of dimensional error on inclined surfaces manufactured by ball-end milling. *The International Journal of Advanced Manufacturing Technology*, 83(5-8):847–859.
- [5] Aslan, D. and Budak, E. (2014). Semi-analytical force model for grinding operations. *Procedia CIRP*, 14:7–12.
- [6] Azizi, A. and Mohamadyari, M. (2015). Modeling and analysis of grinding forces based on the single grit scratch. *The International Journal of Advanced Manufacturing Technology*, 78(5-8):1223–1231.
- [7] Azuaje, F. (2006). Witten ih, frank e: Data mining: Practical machine learning tools and techniques 2nd edition. *BioMedical Engineering OnLine*, 5(1):1.
- [8] Bekey, G. (2008). Springer handbook of robotics (b. siciliano and o. khatib; 2008)[book review]. *IEEE Robotics & Automation Magazine*, 15(3):110–110.

- [9] Benhabib, B., Goldenberg, A. A., and Fenton, R. G. (1985). A solution to the inverse kinematics of redundant manipulators. In *American Control Conference, 1985*, pages 368–374. IEEE.
- [10] Boudreau, R. and Nokleby, S. (2012). Force optimization of kinematically-redundant planar parallel manipulators following a desired trajectory. *Mechanism and Machine Theory*, 56:138–155.
- [11] Brinksmeier, E., Aurich, J., Govekar, E., Heinzl, C., Hoffmeister, H.-W., Klocke, F., Peters, J., Rentsch, R., Stephenson, D., Uhlmann, E., et al. (2006). Advances in modeling and simulation of grinding processes. *CIRP Annals-Manufacturing Technology*, 55(2):667–696.
- [12] Budak, E. (2000). Improving Productivity and Part Quality in Milling of Titanium Based Impellers by Chatter Suppression and Force Control. *Annals of the CIRP*, 49(1):31–36.
- [13] Budak, E., Tunc, L. T., Alan, S., and Özgüven, N. (2012). Prediction of workpiece dynamics and its effects on chatter stability in milling. *CIRP Annals - Manufacturing Technology*, 61:339–342.
- [14] Campa, F., López de Lacalle, L., Lamikiz, A., Bilbao, E., Calleja, A., and Peñafiel, J. (2009). Tool deflection on peripheral milling. *The annals of Dunarea de Jos University of Galati, Fascicle V, technologies in machine building*.
- [15] Carbone, G. and Ceccarelli, M. (2004). A stiffness analysis for a hybrid parallel-serial manipulator. *Robotica*, 22(5):567–576.
- [16] Chen, W. (2000). Cutting forces and surface finish when machining medium hardness steel using cbn tools. *International journal of machine tools and manufacture*, 40(3):455–466.
- [17] Chen, X., Rowe, W., and Cai, R. (2002). Precision grinding using cbn wheels. *International Journal of Machine Tools and Manufacture*, 42(5):585–593.

- [18] Chiaverini, S. (1997). Singularity-robust task-priority redundancy resolution for real-time kinematic control of robot manipulators. *IEEE Transactions on Robotics and Automation*, 13(3):398–410.
- [19] Cho, D. K., Choi, B. W., and Chung, M. J. (1995). Optimal conditions for inverse kinematics of a robot manipulator with redundancy. *Robotica*, 13(1):95–101.
- [20] Choi, Y. (2008). Singularity-robust inverse kinematics using lagrange multiplier for redundant manipulators. *Journal of Dynamic Systems, Measurement, and Control*, 130(5):051009.
- [21] Dai, H., Yuen, K., and Elbestawi, M. (1993). Parametric modelling and control of the robotic grinding process. *The International Journal of Advanced Manufacturing Technology*, 8(3):182–192.
- [22] Deng, Z. H., Zhang, X. H., Liu, W., and Cao, H. (2009). A hybrid model using genetic algorithm and neural network for process parameters optimization in NC camshaft grinding. *The International Journal of Advanced Manufacturing Technology*, 45(9-10):859–866.
- [23] Denkena, B., Möhring, H. C., and Will, J. C. (2007). Tool deflection compensation with an adaptronic milling spindle. In *Conference on Smart Machining Systems*.
- [24] Díaz-Tena, E., Ugalde, U., López De Lacalle, L. N., De la Iglesia, A., Calleja, A., and Campa, F. (2013). Propagation of assembly errors in multitasking machines by the homogenous matrix method. *The International Journal of Advanced Manufacturing Technology*, 68(1-4):149–164.
- [25] Ding, H., Li, Y., and Tso, S. (2000). Dynamic optimization of redundant manipulators in worst case using recurrent neural networks. *Mechanism and Machine Theory*, 35(1):55–70.
- [26] Domroes, F., Krewet, C., and Kuhlenkoetter, B. (2013). Application and Analysis of Force Control Strategies to Deburring and Grinding. *Modern Mechanical Engineering*, 3(June):11–18.

- [27] Fang, F., Wu, H., and Liu, Y. (2005). Modelling and experimental investigation on nanometric cutting of monocrystalline silicon. *International Journal of Machine Tools and Manufacture*, 45(15):1681–1686.
- [28] Feng, J., Chen, P., and Ni, J. (2013). Prediction of grinding force in microgrinding of ceramic materials by cohesive zone-based finite element method. *The International Journal of Advanced Manufacturing Technology*, 68(5-8):1039–1053.
- [29] Ghosal, A. and Desa, S. (1993). Dynamical resolution of redundancy for robot manipulators. *Journal of Mechanical Design*, 115(3):592–598.
- [30] Ghosal, A. and Roth, B. (1988). A new approach for kinematic resolution of redundancy. *The International journal of robotics research*, 7(2):22–35.
- [31] Golberg, D. E. (1989). Genetic algorithms in search, optimization, and machine learning. *Addion wesley*, 1989:102.
- [32] Guo, M., Li, B., Ding, Z., and Liang, S. Y. (2016). Empirical modeling of dynamic grinding force based on process analysis. *The International Journal of Advanced Manufacturing Technology*, pages 1–11.
- [33] Habibi, M., Arezoo, B., and Vahebi Nojedeh, M. (2011). Tool deflection and geometrical error compensation by tool path modification. *International Journal of Machine Tools and Manufacture*, 51(6):439–449.
- [34] Hall, M. A. (1999). *Correlation-based feature selection for machine learning*. PhD thesis, The University of Waikato.
- [35] Hall, M. A. (2000). Correlation-based feature selection of discrete and numeric class machine learning. *Proceedings of 17th International Conference on Machine Learning, San Francisco, CA*, pages 359–366.
- [36] Hall, M. A. and Smith, L. A. (1997). Feature subset selection: a correlation based filter approach. progress in connectionist-based information systems. *International Conference on Neural Information Processing and Intelligent Information Systems*, 2:855–858.

- [37] Hall, M. A. and Smith, L. A. (1998). Practical feature subset selection for machine learning. *Proceedings of the 21st Australasian Computer Science Conference ACSC*, pages 181–191.
- [38] Hecker, R. L., Liang, S. Y., Wu, X. J., Xia, P., and Jin, D. G. W. (2007). Grinding force and power modeling based on chip thickness analysis. *The International Journal of Advanced Manufacturing Technology*, 33(5-6):449–459.
- [39] Ibrahim, O. and Khalil, W. (2006). Inverse dynamic modeling of serial-parallel hybrid robots. In *Intelligent Robots and Systems, 2006 IEEE/RSJ International Conference on*, pages 2156–2161. IEEE.
- [40] Jing, Z. and Cheng, F. (2009). On the joint velocity jump during fault tolerant operations for manipulators with multiple degrees of redundancy. *Mechanism and Machine Theory*, 44(6):1201–1210.
- [41] Jung, S., Hsia, T. C., and Bonitz, R. G. (2004). Force Tracking Impedance Control of Robot Manipulators Under Unknown Environment. *IEEE TRANSACTIONS ON CONTROL SYSTEMS TECHNOLOGY*, 12(3):474–483.
- [42] Kazerounian, K. and Nedungadi, A. (1988). Redundancy resolution of serial manipulators based on robot dynamics. *Mechanism and machine theory*, 23(4):295–303.
- [43] Kiréanski, M. V. and Petrovié, T. M. (1993). Combined analytical-pseudoinverse inverse kinematic solution for simple redundant manipulators and singularity avoidance. *The International journal of robotics research*, 12(2):188–196.
- [44] Kline, W. A., Devor, R. E., and Shareef, I. A. (1982). The Prediction of Surface Accuracy in End Milling. In *Trans, of ASME*, volume 104, pages 272–278.
- [45] Kreutz-Delgado, K., Long, M., and Seraji, H. (1992). Kinematic analysis of 7-dof manipulators. *The International journal of robotics research*, 11(5):469–481.

- [46] Latifinavid, M. and ilhan Konukseven, E. (2017). Hybrid model based on energy and experimental methods for parallel hexapod-robotic light abrasive grinding operations. *The International Journal of Advanced Manufacturing Technology*, pages 1–15.
- [47] Law, K. M. Y., Geddam, A., and Ostafiev, V. A. (1999). A process-design approach to error compensation in the end milling of pockets. *Journal of Materials Processing Technology*, 89-90:238–244.
- [48] Leonesio, M., Parenti, P., Cassinari, A., Bianchi, G., and Monno, M. (2012). A time-domain surface grinding model for dynamic simulation. *Procedia CIRP*, 4:166–171.
- [49] Li, D., Xu, M., and Wei, C. (2012). A dynamic threshold-based fuzzy adaptive control algorithm for hard sphere grinding. *Int J Adv Manuf Technol*, 60:923–932.
- [50] Li, Y. and Leong, S. H. (2004). Kinematics control of redundant manipulators using a cmac neural network combined with a genetic algorithm. *Robotica*, 22(6):611–621.
- [51] Liu, C., Chen, a., Wang, Y.-T., and Chen, C.-C. (2004). Modelling and simulation of an automatic grinding system using a hand grinder. *The International Journal of Advanced Manufacturing Technology*, 23:874–881.
- [52] Liu, C. C., Chen, A., Chen, C.-C. C., and Wang, Y. Y.-T. (2005). Grinding force control in an automatic surface finishing system. *Journal of materials processing Technology*, 170(1-2):367–373.
- [53] Long, G. L. and Paul, R. P. (1992). Singularity avoidance and the control of an eight-revolute-joint manipulator. *The International journal of robotics research*, 11(6):503–515.
- [54] Lopes, A. and Almeida, F. (2008). A force–impedance controlled industrial robot using an active robotic auxiliary device. *Robotics and Computer-Integrated Manufacturing*, 24(3):299–309.

- [55] López de Lacalle, L. N., Lamikiz, A., Muñoa, J., Salgado, M., and Sánchez, J. (2006). Improving the high-speed finishing of forming tools for advanced high-strength steels (ahss). *The International Journal of Advanced Manufacturing Technology*, 29(1):49–63.
- [56] López de Lacalle, L. N., Lamikiz, A., Sanchez, J., and Salgado, M. (2004). Effects of tool deflection in the high-speed milling of inclined surfaces. *The International Journal of Advanced Manufacturing Technology*, 24(9-10):621–631.
- [57] López de Lacalle, L. N., Lamikiz, A., Sanchez, J., and Salgado, M. (2007). Toolpath selection based on the minimum deflection cutting forces in the programming of complex surfaces milling. *International Journal of Machine Tools and Manufacture*, 47(2):388–400.
- [58] López de Lacalle, L. N., Lamikiz, A., Sánchez, J. A., and Bustos, I. F. D. (2005). Simultaneous Measurement of Forces and Machine Tool Position for Diagnostic of Machining Tests. *IEEE TRANSACTIONS ON INSTRUMENTATION AND MEASUREMENT*, 54(6):2329–2335.
- [59] López de Lacalle, L. N., Lamikiz, A., Sanchez, J. A., and de Bustos, I. F. (2005). Simultaneous measurement of forces and machine tool position for diagnostic of machining tests. *IEEE transactions on instrumentation and measurement*, 54(6):2329–2335.
- [60] Lopez de Lacalle, L. N., Lamikiz, A., Sanchez, J. A., and Salgado, M. A. (2004). Effects of tool deflection in the high-speed milling of inclined surfaces. *Int J Adv Manuf Technol*, 24:621–631.
- [61] López de Lacalle, L. N., Lamikiz, A., Sánchez, J. A., and Salgado, M. A. (2007). Toolpath selection based on the minimum deflection cutting forces in the programming of complex surfaces milling. *International Journal of Machine Tools and Manufacture*, 47(2):388–400.
- [62] Luo, J., editor (2012). *Advances in Intelligent and Soft Computing - Soft*

Computing in Information Communication Technology. Springer Science & Business Media.

- [63] Malkin, S. (2002). *Grinding technology*. Society of Manufacturing Engineers (SME).
- [64] Malkin, S. and Cook, N. H. (1971). The wear of grinding wheels: part 1—attritious wear. *Journal of Engineering for Industry*, 93(4):1120–1128.
- [65] Mendes, N., Neto, P., Pires, J. N., and Loureiro, A. (2013). An optimal fuzzy-PI force / motion controller to increase industrial robot autonomy. *Int J Adv Manuf Technol*, 68:435–441.
- [66] Miller, L. M., Kim, H., and Rosen, J. (2011). Redundancy and joint limits of a seven degree of freedom upper limb exoskeleton. In *Engineering in Medicine and Biology Society, EMBC, 2011 Annual International Conference of the IEEE*, pages 8154–8157. IEEE.
- [67] Mingyang, Z., Tong, G., Ge, C., Qunming, L., and Dalong, T. (1995). Development of a redundant robot manipulator based on three dof parallel platforms. In *Robotics and Automation, 1995. Proceedings., 1995 IEEE International Conference on*, volume 1, pages 221–226. IEEE.
- [68] Mitsi, S. and Bouzakis, K.-D. (1993). Simulation of redundant manipulators for collision avoidance in manufacturing and assembly environments. *Mechanism and machine theory*, 28(1):13–21.
- [69] Nearchou, A. C. (1998). Solving the inverse kinematics problem of redundant robots operating in complex environments via a modified genetic algorithm. *Mechanism and machine theory*, 33(3):273–292.
- [70] Nieslony, P., Krolczyk, G., Wojciechowski, S., Chudy, R., Zak, K., and Maruda, R. (2018). Surface quality and topographic inspection of variable compliance part after precise turning. *Applied Surface Science*, 434:91–101.
- [71] Nokleby, S. B. and Podhorodeski, R. P. (2001). Reciprocity-based resolution

- of velocity degeneracies (singularities) for redundant manipulators. *Mechanism and machine theory*, 36(3):397–409.
- [72] Oh, S.-Y., Orin, D., and Bach, M. (1984). An inverse kinematic solution for kinematically redundant robot manipulators. *Journal of Field Robotics*, 1(3):235–249.
- [73] Özgören, M. K. (2002). Topological analysis of 6-joint serial manipulators and their inverse kinematic solutions. *Mechanism and Machine Theory*, 37(5):511–547.
- [74] Özgören, M. K. (2007). Kinematic analysis of spatial mechanical systems using exponential rotation matrices. *Journal of Mechanical Design*, 129(11):1144–1152.
- [75] Özgören, M. K. (2013). Optimal Inverse Kinematic Solutions for Redundant Manipulators by Using Analytical Methods to Minimize Position and Velocity Measures. *Journal of Mechanisms and Robotics*, 5(3):031009.
- [76] Pagilla, P. and Yu, B. (2001). Adaptive control of robotic surface finishing processes. In *Proceedings of the 2001 American Control Conference. (Cat. No.01CH37148)*, volume 1, pages 630–635.
- [77] Pourazady, M. and Ho, L. (1991). Collision avoidance control of redundant manipulators. *Mechanism and machine theory*, 26(6):603–611.
- [78] Pueh, L. H. (1993). Motions with minimal joint torques for redundant manipulators. *TRANSACTIONS-AMERICAN SOCIETY OF MECHANICAL ENGINEERS JOURNAL OF MECHANICAL DESIGN*, 115:599–599.
- [79] Puga, J. P. and Chiang, L. E. (2008). Optimal trajectory planning for a redundant mobile manipulator with non-holonomic constraints performing push–pull tasks. *Robotica*, 26(3):385–394.
- [80] Rao, V. S. and Rao, P. V. M. (2006a). Effect of workpiece curvature on cutting forces and surface error in peripheral milling. *Proceedings of the Insti-*

- tution of Mechanical Engineers, Part B: Journal of Engineering Manufacture*, 220(9):1399–1407.
- [81] Rao, V. S. and Rao, P. V. M. (2006b). Tool deflection compensation in peripheral milling of curved geometries. *International Journal of Machine Tools and Manufacture*, 46(15):2036–2043.
- [82] Romdhane, L. (1999). Design and analysis of a hybrid serial-parallel manipulator. *Mechanism and Machine Theory*, 34(7):1037–1055.
- [83] Ryu, S. H., Lee, H. S., and Chu, C. N. (2003). The form error prediction in side wall machining considering tool deflection. *International Journal of Machine Tools & Manufacture*, 43:1405–1411.
- [84] Sciavicco, L. and Siciliano, B. (1988). A solution algorithm to the inverse kinematic problem for redundant manipulators. *IEEE Journal on Robotics and Automation*, 4(4):403–410.
- [85] Shimizu, M., Kakuya, H., Yoon, W.-K., Kitagaki, K., and Kosuge, K. (2008). Analytical inverse kinematic computation for 7-dof redundant manipulators with joint limits and its application to redundancy resolution. *IEEE Transactions on Robotics*, 24(5):1131–1142.
- [86] Singh, G. K. and Claassens, J. (2010). An analytical solution for the inverse kinematics of a redundant 7dof manipulator with link offsets. In *Intelligent Robots and Systems (IROS), 2010 IEEE/RSJ International Conference on*, pages 2976–2982. IEEE.
- [87] Song, H.-C. and Song, J.-B. (2013). Precision robotic deburring based on force control for arbitrarily shaped workpiece using cad model matching. *International Journal of Precision Engineering and Manufacturing*, 14(1):85–91.
- [88] Soori, M., Arezoo, B., and Habibi, M. (2014). Virtual machining considering dimensional, geometrical and tool deflection errors in three-axis CNC milling machines. *Journal of Manufacturing Systems*, 33(4):498–507.

- [89] Suh, S.-H., Cho, J.-H., and Hascoet, J.-Y. (1996). Incorporation of Tool Deflection in Tool Path Computation: Simulation and Analysis. *Journal of Manufacturing Systems*, 15(3):190–199.
- [90] Tahvilian, A. M., Hazel, B., Rafieian, F., Liu, Z., and Champliand, H. (2015). Force model for impact cutting grinding with a flexible robotic tool holder. *The International Journal of Advanced Manufacturing Technology*, pages 1–15.
- [91] Tang, J., Du, J., and Chen, Y. (2009). Modeling and experimental study of grinding forces in surface grinding. *Journal of materials processing technology*, 209(6):2847–2854.
- [92] Tao, Y., Zheng, J., Lin, Y., Wang, T., Xiong, H., He, G., and Xu, D. (2015). Fuzzy PID control method of deburring industrial robots. *Journal of Intelligent & Fuzzy Systems*, 29(6):2447–2455.
- [93] Thomessen, T., Lien, T. K., and Sann ns, P. K. (2001). Robot control system for grinding of large hydro power turbines. *Industrial Robot: An International Journal*, 28(4):328 – 334.
- [94] T nshoff, H., Peters, J., Inasaki, I., and Paul, T. (1992). Modelling and simulation of grinding processes. *CIRP Annals-Manufacturing Technology*, 41(2):677–688.
- [95] Wang, D., Ge, P., Bi, W., and Jiang, J. (2014). Grain trajectory and grain workpiece contact analyses for modeling of grinding force and energy partition. *The International Journal of Advanced Manufacturing Technology*, 70(9-12):2111–2123.
- [96] Wang, S., To, S., and Cheung, C. (2013). An investigation into material-induced surface roughness in ultra-precision milling. *The International Journal of Advanced Manufacturing Technology*, 68(1-4):607–616.
- [97] Weghe, M. V., Ferguson, D., and Srinivasa, S. S. (2007). Randomized path planning for redundant manipulators without inverse kinematics. In

Humanoid Robots, 2007 7th IEEE-RAS International Conference on, pages 477–482. IEEE.

- [98] Wojciechowski, S., Maruda, R., Barrans, S., Nieslony, P., and Krolczyk, G. (2017). Optimisation of machining parameters during ball end milling of hardened steel with various surface inclinations. *Measurement*, 111:18–28.
- [99] Wojciechowski, S., Maruda, R. W., Krolczyk, G. M., and Nieslony, P. (2018). Application of signal to noise ratio and grey relational analysis to minimize forces and vibrations during precise ball end milling. *Precision Engineering*, 51:582–596.
- [100] Yang, M. Y. and Choi, J. G. (1998). A tool deflection compensation system for end milling accuracy improvement. *JOURNAL OF MANUFACTURING SCIENCE AND ENGINEERING*, 120(2):222–229.
- [101] Yang, Z., Gao, Y., Zhang, D., and Huang, T. (2003). A Self-tuning Based Fuzzy-PID Approach for Grinding Process Control. *Key Engineering Materials. Trans Tech Publications*, 238-239:375–382.
- [102] Zeng, G. and A., H. (1997). An overview of robot force control. *Robotica*, 15(5):473–482.
- [103] Zhang, B., Wang, J., Yang, F., and Zhu, Z. (1999). The effect of machine stiffness on grinding of silicon nitride. *International Journal of Machine Tools and Manufacture*, 39(8):1263–1283.
- [104] Zheng, X., Bin, H., and Luo, Y. (2004). Kinematic analysis of a hybrid serial-parallel manipulator. *The International Journal of Advanced Manufacturing Technology*, 23(11-12):925–930.

CURRICULUM VITAE

1. Name/Surname: MASOUD LATIFINAVID

2. Date of Birth: 21/09/1982

3. Contact: latifinaid@gmail.com - Tel: +90-5319675896

4. Education:

Degree	Department	University	Year
Bachelor	Mechanical Engineering	Tabriz Azad University	2001-2007
Master	Mechatronic Engineering	Sharif University of Technology	2007-2009
PhD	Mechanical Engineering	Middle East Technical University	2010-2018

5. Thesis:

Degree	Thesis Title	Supervisor	Year
Master	Computer aided prognosis of epileptic patients using multi-modality data and artificial intelligence techniques	Prof. Dr. Hamid SOLTANIAN ZADEH	2007-2009
PhD	Development of high performance hybrid robotic deburring system	Assoc. Prof. Dr. Erhan İlhan KONUKSEVEN	2010-2018

6. Academic positions and job experiences

Position	Department	Year
Lecturer	Mechatronic Engineering Department, THK University, Ankara	August 2014– 2018

Research assistant	Mechatronic Engineering Department, THK University, Ankara	December 2013 – August 2014
Research assistant	Cognitive Science Department. Iran Institute of Fundamental Sciences (IPM)	December 2008 –October 2009
Research assistant	Sharif University of Technology, Iran	September 2007– January 2008

7. Publications

7.1. International peer review journals

- LATIFINAVID M., KONUKSEVEN E.İ “Hybrid model based on energy and experimental methods for parallel hexapod-robotic light abrasive grinding operations”, International Journal of Advanced Manufacturing Technology, 2017. (SCI)
- LATIFI-NAVID M., BİLEN M., KONUKSEVEN E.İ., DOĞAN M., ALTUNBASER A., “Fast and Accurate Semi-automatic Haptic Segmentation of Brain Tumor in 3D MRI Images”, Turkish Journal of Electrical Engineering & Computer Sciences, DOI: 10.3906/elk-1308-132, pp. - , 2016. (SCI)
- M. Latifi-Navid, K.V. Elisevich, H. Soltanian-Zadeh, “Algorithmic Analysis of Clinical and Neuropsychological Data in Localization-Related Epilepsy”, International Journal of Computational Models and Algorithms in Medicine (IJCMAM), 2013.

7.2. International conference proceedings

- A. Zabihollah, M.Latifi-Navid,Sh. Zareie, , “Comparison of classical and optimal control strategies applied for active vibration suppression of adaptive laminated beams” , Proceeding of the Third International Conference on Modeling, Simulation and Applied Optimization, Sharjah, U.A.E. 2009.
- A. Zabihollah, Sh. Zareie, M.Latifi-Navid, “Random Vibration Response of Axially loaded Laminated Tapered Beam-columns”, 1st International Conference on Composites: Characterization, Fabrication, and Application, Kish Island, Iran, 2008.
- A. Zabihollah*, S. Zareie, M. Latifi-Navid, H. Ghafari, “Effects of Ply-drop off on Forced Vibration Response of Non-uniform Thickness Laminated Composite Beams”, 1st International Conference on Composites: Characterization, Fabrication, and Application, Kish island, Iran, 2008.

- B. Rohani, M. Latifi-Navid, F. Saeidi, M. Ghaziani, “A Hydraulic Strategy Design for Modelling and Simulation of A Mold Oscillation System”, the 15th International Conference on Machine Design and Production June 19– 22, 2012, Pamukkale, Denizli, Turkey.
- M. Latifi-Navid, K.V. Elisevich, H. Soltanian-Zadeh, “ Algorithmic Analysis of Clinical and Neuropsychological Data in Localization-Related Epilepsy”, International conference on applied computational mathematics ICACM 2012, Ankara, Turkey. (Extended Abstract)

8. Research projects

Code: 114E272, Project title: “Development of high performance hybrid robotic deburring system”, TÜBİTAK 1001 R & D project.

9. Conference and organizations

- 2008 CSI International Computer Engineering Conference, Organization Committee (CSICC-08) Iran, March 9-11, 2008.

14. Administrative duties

Internship coordinator, University of Turkish Aeronautical Associations, Mechatronic Engineering Department, (2014-2017)

15. Awards & scholarships

- TÜBİTAK-BİDEB 2215 International PhD students’ fellowship 2011-2013.
- Turkish government scholarship 2009.
- 2016 Finalist of “Yeni Fikirler Yeni İşler (YFYI 2016)”, Third selected project by people open voting
- 2017 Finalist of “Yeni Fikirler Yeni İşler (YFYI 2017)”, The final round will be held at 14 October 2017.